ENHANCED BIOLOGICALLY-INFORMED MODELS OF INFECTIOUS DISEASES: STRUCTURE AND DYNAMICS

MAHMUDA RUMA

A DISSERTATION SUBMITTED TO THE FACULTY OF GRADUATE STUDIES
IN PARTIAL FULFILMENT OF THE REQUIREMENTS
FOR THE DEGREE OF
DOCTOR OF PHILOSOPHY

GRADUATE PROGRAM IN MATHEMATICS AND STATISTICS
YORK UNIVERSITY
TORONTO, ONTARIO

APRIL 2026

Abstract

Abstract

Infectious diseases such as HIV, measles, and influenza continue to pose major challenges to global health, particularly in the presence of waning immunity, evolving pathogens, and heterogeneous contact patterns. Understanding the mechanisms driving infection persistence, disease resurgence, and the effectiveness of interventions requires the integration of mathematical modeling. However, an increased level of understanding that modelling can provide here depends on the robustness of the model in (1) it's representation of the biology and (2) the analyzes and simulation studies that can be conducted to produce quality results.

This thesis explores the effects of incorporating biological mechanisms into models of infectious diseases that are often ignored. In the first project we incorporate the virus loss term into a model of pathogen dynamics in-host in order to determine if such a term affects the model dynamics and bifurcation. In the second project we analyze the effects of waning immunity on the probability and severity of measles infections in populations with varying degrees of vaccine-induced immunity. We then extend this waning immunity framework to a study of seasonal influenza. Finally, we explore the effects of environmental reservoirs on the transmissibility of COVID-19, influenza, measles and norovirus in a defined spatial location – a theme park. In all projects we consider deterministic and/or stochastic modelling outcomes, and sensitivity analyses to study the model population dynamics and bifurcations and determine model parameters that most affect population and infection outcomes.

By integrating theoretical analysis, numerical simulation, and sensitivity-based methods, this research provides a unified understanding of infection dynamics from within-host to population scales. The findings offer valuable information for designing effective medical and public health intervention strategies.

Acknowledgements

Acknowledgements

I would like to begin by expressing my sincere gratitude to the Almighty for granting me the strength, patience, and perseverance to complete this research.

My deepest appreciation goes to my supervisor, Dr. Jane Heffernan, Professor in the Department of Mathematics and Statistics at York University, for her continuous guidance, encouragement, and insightful feedback throughout my doctoral studies. Her expertise and unwavering support have been invaluable for the success of this work and for my academic development.

I extend my thanks to all faculty and staff members of the Department of Mathematics and Statistics, York University, for their academic guidance and assistance during my PhD journey.

Finally, I am profoundly grateful to my parents, my husband, and my children for their constant love, patience, and encouragement. I give special thanks to my daughters for their remarkable understanding and tolerance throughout this journey, as I could often not give them the time they deserved. Their support has been my greatest motivation.

Table of Contents

List of Tables

List of Figures

Chapter 1

Introduction

Pathogenic microorganisms such as bacteria, viruses, parasites, and fungi, are responsible for causing infectious diseases. Individuals that contract these microorganisms can become very sick [1, 2, 3]. These microorganisms can also cause large outbreaks within communities [4, 5, 6]. Mathematical models of Disease can be used to study infections in individuals (immunology) and populations (epidemiology), including the dynamics and persistence of infectious diseases, and possible control strategies that can reduce morbidity and mortality [7, 8, 9, 10, 11]. Sometimes, however, simplifying assumptions can be made in the mathematical model that can omit certain parts of the system that may be important to the overall outcome of infection, affecting effective control strategy determination [12, 13, 14].

In this thesis, our aim is to study the effects of including biological mechanisms into a model that are typically omitted, specifically: the addition of a virus loss term in in-host modelling, including waning immunity in population-level models of infectious diseases, including stochastic effects on pathogen infection and persistence in a population, including an environmental reservoir in a population-level model where environmental transmission can occur. By introducing a virus loss term, we can more accurately capture the decline in viral load over time within a host. Adding a level of waning immunity will allow us to model the gradual loss of immunity post-infection or vaccination, reflecting more accurately

real-world scenarios. Incorporating stochasticity introduces randomness to better simulate the unpredictable nature of disease transmission and progression. Finally, the inclusion of an environmental reservoir accounts for the presence and impact of pathogens in the environment, which can play a crucial role in the spread of disease.

Through these modifications, we seek to investigate how these factors influence disease outcomes at both the individual host level and the population level. Our goal is to provide deeper insight into disease mechanisms and contribute to the development of more effective control and prevention strategies.

1.1 Introduction to Mathematical Modelling of Infectious Disease

Mathematical modelling can provide an understanding of the underlying mechanisms of disease transmission and spread, help to pinpoint key factors in the disease transmission process, suggest effective control and preventive measures, and provide an estimate for the severity and potential scale of the epidemic.

1.1.1 The Basics in Mathematical Epidemiology

Kermack-Mckendrick [15] introduced the mathematical theory of epidemics. Dividing the population into three states (susceptible S, infected I, recovered R), they proposed the following basic model in Mathematical Epidemiology [15]:

$$\begin{aligned} \tfrac{dS}{dt} &= \lambda - \beta SI - \mu S \\ \tfrac{dI}{dt} &= \beta SI - \gamma I - \delta I \\ \tfrac{dR}{dt} &= \gamma I - dR\,. \end{aligned} \tag{1.1}$$

This model is called the SIR model. Here, β is the transmission rate, γ is the recovery rate, μ is the natural death rate, δ is the disease-induced death rate, and λ is the incoming rate of susceptibles, or birth rate. We also note that it is assumed that susceptibles are fully susceptible and recovered individuals are fully immune. Infectious individuals transmit the disease and can recover.

Basic Reproduction Number: The basic reproduction number, $\mathcal{R}_0$, is defined as the expected number of secondary cases produced by a single infection when introduced into a completely susceptible population. For the SIR,

$$\mathcal{R}_0 = \frac{\beta S_0}{\gamma + d}$$

where S_0 is the proportion of susceptibles at the disease free equilibrium. The initial number of susceptibles could be $S_0 = \lambda/d$. We refer the reader to reference [16] for a review on $\mathcal{R}_0$ and different methods of derivation.

Control Reproduction Number: The control reproduction number R_c extends the concept of the basic reproduction number to populations where control mechanisms such as vaccination are employed. Here, Assuming vaccine-induced immunity is life-long,

$$R_c = (1 - p)\mathcal{R}_0$$

where p is the rate of vaccination.

Herd Immunity: Herd immunity refers to the indirect protection against a contagious infectious disease that happens when a significant fraction p_c of the population is immune either through vaccination or immunity developed through previous infection. The basic definition for the significant fraction is

$$p_c = 1 - \tfrac{1}{\mathcal{R}_0} \ .$$

1.1.2 The Basics in Mathematical Immunology / Pathogen Dynamics

The basic model of pathogen dynamics, the TIV model, was introduced by Perelson and colleagues in the 1990's [17, 18]. It includes cells that the pathogen infects (target cells), the pathogen, and different components of the life-cycle of the pathogen including the steps needed by which the pathogen can produce progeny.

The basic model describing the interaction between uninfected target cells T, infected cells I, and the virus V, is governed by the following system of differential equations:

$$\begin{aligned} \frac{dT}{dt} &= s - dT - \beta TV \\ \frac{dI}{dt} &= \beta TV - \delta I \\ \frac{dV}{dt} &= pI - cV \end{aligned} \tag{1.2}$$

where s and d are the birth and death rates of the target cells, β is the infection rate, δ is the death rate of infected cells, p is the pathogen production rate by the infected cells, and c is the clearance rate of the pathogen. This model has the following reproduction number

$$R_0 = \frac{p\beta T_0}{\delta c}$$

where $T_0 = \frac{s}{d}$ is an equilibrium value of target cells.

1.1.3 Extensions to the Basic Models

The SIR and TIV models omit some characteristics of the biology. We will now provide an overview of characteristics that we will incorporate into modelling studies in this thesis.

1.1.3.1 The Virus Loss Term

When a virus particle infects a cell, it is enters the cells and is lost to the population. The basic TIV model (1.2) does not include this component of the biology. The new TIV model with the virus loss term is:

$$\begin{aligned} \frac{dT}{dt} &= s - dT - \beta TV \\ \frac{dI}{dt} &= \beta TV - \delta I \\ \frac{dV}{dt} &= pI - cV - \beta_v TV \end{aligned} \tag{1.3}$$

where the magnitude of $\beta_v = \beta$ and β_v is the virus loss term. The basic reproduction number for Model (1.3) is

$$\mathcal{R}_0 = \frac{p}{\delta} \frac{\beta T_0}{(c + \beta_v T_0)}$$

where p/δ gives the number of new virus particles that an infected cell makes and $\beta T_0/(c+\beta_v T_0)$ gives the probability that a virus will infect a cell.

We note that the vast majority of in-host modelling studies ignore the effects of the virus loss term as it is generally assumed that $\beta_v T << c$. However, inclusion of this term provides a more realistic basic reproduction number in that it includes the probability of infecting a cell ($\beta T_0/(c + \beta_v T_0)$) rather than allowing a virus particle to infect many cells ($\beta T_0/c$) which is biologically implausible. The inclusion of this term can also provide much richer dynamics of a model [19, 20, 21, 22]. We thus will include this term in our study in this thesis. We direct the reader to [22] for more discussion of the virus loss term.

1.1.3.2 The Immune Response

The immune response to pathogens is a coordinated, multi-layered defense system that detects, contains, and eliminates invading organisms while limiting damage to the host. It begins with innate immunity, which provides rapid, non-specific protection through physical barriers, antimicrobial molecules, and immune cells such as macrophages and neutrophils that recognize pathogens. Signals from the innate response activate adaptive immunity, in which

specialized cells mount highly specific responses: B-cells produce antibodies that neutralize or mark pathogens for destruction, while T-cells kill infected cells (cytotoxic T-cells) or coordinate immune activity (helper T-cells). Together, these processes lead to pathogen clearance and the formation of immunological memory, enabling faster and more effective responses upon future exposure to the same pathogen.

The basic TIV Model (1.2) does not explicitly model the effects of the immune response. Instead, it is assumed that the immune response will (1) increase parameters like c and δ that reflect antibody neutralization and infected cell killing, respectively, or (2) decrease parameters like β to reflect blocking of infection from specific cytokines [22]. There are many extensions of the basic model to explicity include modelling of the immune response. We refer the reader to [22, 23] for particular examples.

We are interested in modelling the effects of T-helper cells explicitly, including their proliferation and their effects on infected cell killing. An example of such a model is:

$$\begin{aligned} T' &= s - \beta TV - dT \\ T'_H &= s_H - \beta_H T_H V - d_H T_H + p_H T_H \\ I' &= \beta_H T_H V + \beta TV - \mu_I I - \sigma T_H I \\ V' &= pI - V \end{aligned} \tag{1.4}$$

where s_H is the incoming rate to T-helper cells into the system, d_H is the natural death rate of T-helper cells, and p_H is the proliferation rate of these cells. This model also includes an infected cell killing term $\sigma T_H I$ that assumes that infected cell killing is proportional to the T-helper cells in the system. It also includes possible infection of T-helper cells by the pathogen, which can occur in HIV infection. We note that this model ignores pathogen loss due to infection of target cells T and T-helper cell T_H populations, but this is also a term that we will consider in this thesis (discussed above section (1.1.3.1)).

1.1.3.3 The Exposed Class

The basic SIR Model (1.1) assumes that once someone has come into contact with an infected individual, they can immediately be infected and infect others. This is not true as there exists a time between infection and becoming infectious. This is called the latent period of infection, or the exposed period of infection and is generally represented by E in an SEIR model

$$\begin{aligned} \tfrac{dS}{dt} &= \lambda - \beta SI - dS \\ \tfrac{dE}{dt} &= \beta SI - dE - \sigma E \\ \tfrac{dI}{dt} &= \sigma E - \gamma I - dI \\ \tfrac{dR}{dt} &= \gamma I - dR\,. \end{aligned} \tag{1.5}$$

where σ is the rate at which exposed individuals move to the infectious class I. Here, $\mathcal{R}_0$ becomes

$$\mathcal{R}_0 = \frac{\beta S_0}{\gamma + d}\frac{\sigma}{\sigma + d}\ .$$

Examples of studies that employ the SEIR model, and various extensions, include [24, 25].

1.1.3.4 Waning Immunity

The basic SIR Model (1.1) assumes that once someone is infected they cannot become infected again – that is, they remain in the recovered class forever. However, some infectious diseases do not have this characteristic. For example, people can experience influenza infection many times in their lives [26, 27, 28]. This is also true for the common cold, pertussis, and COVID-19 [29, 30].

A simple extension for including waning immunity in a model of infectious diseases in a population is called the SIRS model, and is given by

$$\begin{aligned} S' = &\quad \lambda - \beta SI - dS + \omega R \\ I' = &\quad \beta SI - \gamma I - dI \end{aligned}$$

$$R' = \quad \gamma I - dR - \omega R$$

where ω is the waning rate of immunity from the recovered class. We may also, however, choose to explicitly model an intermediate (partially immune) stage representing waning immunity W such that

$$\begin{aligned} S' &= \lambda - \beta SI - dS + \phi W \\ I' &= \beta SI - \gamma I - dI \\ R' &= \gamma I - dR - \omega R \\ W' &= \omega R - \phi W - dW \end{aligned}$$

where ω is the waning rate of effective immunity from the R to the waning immunity class W, and ϕ is the waning rate from W to S. This model, called the SIRWS model, has been previously studied by [31, 32, 33].

A different extension is to include vaccination and waning, which can be captured by the following model:

$$\begin{aligned} S' &= \lambda(1-p) - \beta SI - dS + \phi S \\ I' &= \beta SI - \gamma I - dI \\ R' &= \gamma I - dR \\ V' &= \lambda p - \omega V - dV \\ W' &= \omega V - dW - \phi W \end{aligned} \tag{1.6}$$

where p is the fraction of incoming susceptibles that are vaccinated and move to the recovered class.

1.1.3.5 An Environmental Reservoir

Infected individuals can shed pathogen into their surrounding environment. While in the environment (and before it has decayed), susceptibles can be exposed to this pathogen

reservoir and become infected. Infectious diseases where environmental contamination and transmission have been documented include: measles [34, 35], COVID-[36, 37], and norovirus [38, 39, 40].

An extension of the basic SIR Model (1.1) to include the effects of an environmental reservoir is

$$\begin{aligned} S' &= \lambda - \beta SI - \beta_G SG - dS \\ I' &= \beta SI + \beta_G SG - \gamma I - dI \\ R' &= \gamma I - dR \\ G' &= kI - \delta G \end{aligned} \tag{1.7}$$

where G is the pathogen load in the environment, δ is the pathogen decay rate, and β_G is the infection rate of susceptibles from the environment. Mathematical models in the literature that includes the effects of environmental reservoirs include [41, 42, 43, 44, 45].

1.1.3.6 Heterogeneous Populations

Susceptibility, infectivity, and immunity can differ between individuals, and different subgroups of a population. Behaviour can also differ between hosts and subgroups, and affect the possibility of infectious disease transmission. The SIR and SEIR models can be extended to explicitly include the effects of host or subpopulation heterogeneities. For example,

$$\begin{aligned} \tfrac{dS_i}{dt} &= \lambda_i - \Sigma_j \beta_{ij} S_i I_j - d_i S_i \\ \tfrac{dI_i}{dt} &= \Sigma_j \beta_{ij} S_i I_j - d_i I_i - \delta_i I - \gamma_i I_i \\ \tfrac{R_i}{dt} &= \gamma_i I_i - d_i R_i \end{aligned} \tag{1.8}$$

where i,j denote the subpopulations with differences in birth or immigration rate λ, natural death or emigration rate d, disease-induced death rate δ, recovery rate γ_i, or transmissibility β_{ij} between susceptibles of type i and infecteds of type j.

Models with heterogeneous host types have been used to study superspreaders, the effects

of age structure of infectious disease spread and burden, and differences in sex, among others [46, 47, 48, 49, 50].

1.2 Diseases of application

In this thesis we study models that are applicable to specific diseases of interest. For the in-host model, we focus on HIV. The population-level models are applied to Measles, influenza, norovirus, and COVID-19.

1.2.1 Human Immunodeficiency Virus (HIV)

Human Immunodeficiency Virus (HIV) infection, which emerged prominently in the early 1980s, continues to represent one of the most pressing global public health challenges [51, 52]. HIV is a retrovirus that progressively weakens the immune system by targeting and destroying $CD4^+$ T lymphocytes—cells that play a central role in coordinating immune defense [53]. The virus is primarily transmitted through unprotected sexual contact, from mother to child during pregnancy, childbirth, or breastfeeding, and through exposure to contaminated blood or shared needles [54]. According to recent estimates, approximately 39 million people are living with HIV worldwide, with 1.3–2 million new infections and 770,000–1,000,000 HIV-related deaths reported annually [52].

Monitoring HIV infection typically involves two key blood tests: the HIV viral load test, which quantifies the concentration of virus in the bloodstream, and the $CD4^+$ T lymphocyte count, which assesses immune competence and tracks disease progression [55]. Although no definitive cure currently exists, HIV can be effectively controlled through antiretroviral therapy (ART), which suppresses viral replication, promotes immune restoration, and significantly reduces the risk of transmission [56, 57].

Understanding the intricate interplay between viral replication, immune response, and

therapeutic intervention is crucial for characterizing HIV pathogenesis and evaluating treatment efficacy. Within-host mathematical models offer a powerful framework for describing these interactions quantitatively. By formulating systems of differential equations that capture the dynamics of uninfected and infected $CD4^+$ T cells, free virus particles, and immune response factors, such models enable researchers to analyze viral persistence, estimate key biological parameters, and assess the impact of ART on infection control. These models form the foundation for linking cellular-level processes to clinical outcomes and for informing strategies to achieve long-term viral suppression or potential functional cure.

In this thesis, we study an in-host model of HIV infection. Using bifurcation analysis, we look for outcomes that affect HIV clearance.

1.2.2 Measles

Measles is a highly contagious viral disease that predominantly affects children and remains a significant cause of morbidity and mortality in regions with low vaccination coverage. The causative agent, a member of the Paramyxoviridae family, is transmitted through respiratory droplets and aerosols produced by coughing or sneezing and can remain infectious in the air or on contaminated surfaces for up to two hours [58, 59]. Infection occurs when susceptible individuals inhale contaminated air or touch infected surfaces and subsequently contact their eyes, nose, or mouth.

Vaccination is the most effective preventive measure against measles and is typically administered in two doses—first at 12–18 months of age and again at 4–6 years—to ensure long-term immunity [60]. Measles is among the most infectious human diseases, with an estimated basic reproduction number (R_0) ranging between 12 and 18 [61].

Given its high transmissibility and well-characterized transmission pathways, measles provides an important framework for studying infectious disease dynamics. Mathematical models—particularly compartmental models such as the susceptible–infectious–recovered

(SIR) framework—are widely used to quantify disease spread, evaluate vaccination strategies, and assess the threshold immunity required to achieve herd protection.

In this thesis, we quantify outcomes of measles infection in populations considering waning immunity and environmental transmission.

1.2.3 Influenza

Influenza, commonly known as the flu, is an acute respiratory infection caused by negative-sense single-stranded RNA viruses belonging to the family Orthomyxoviridae [62, 63]. The disease spreads primarily through respiratory droplets and aerosols produced when infected individuals cough, sneeze, or speak, as well as through contact with contaminated surfaces or secretions [64]. There are three main types of influenza viruses—A, B, and C—classified based on differences in their matrix and nucleoprotein antigens [65]. Most seasonal epidemics and occasional pandemics are caused by influenza A viruses, while influenza B viruses typically produce milder outbreaks and influenza C viruses are associated with moderate respiratory illness [66].

Due to frequent antigenic drift and occasional antigenic shift, influenza viruses continually evade host immunity, meaning that protection conferred by prior infection or vaccination is often incomplete or short-lived [67]. As a result, annual vaccination is recommended as the primary preventive strategy to reduce infection risk, disease severity, and community transmission [68]. The basic reproduction number (R_0) of influenza varies across strains and seasons but is generally estimated between 1.2 and 3 [69].

Given its rapid antigenic evolution and incomplete or partial immunity from prior infection or vaccination, influenza can induce public health burden in all populations every year. Mathematical models that capture effective immunity in populations, and direct and environmental transmission are thus of interest.

In this thesis, we quantify outcomes of influenza infection in populations considering

changing effective immunity and environmental transmission.

1.2.4 Norovirus

Norovirus is a very contagious virus that causes stomach and intestinal illness. It is a non-enveloped, positive-sense single-stranded RNA virus that belongs to the family Caliciviridae [70, 71]. Norovirus is one of the main causes of acute gastroenteritis around the world. It can cause single cases or large outbreaks in places such as schools, cruise ships, hospitals, and nursing homes [72].

The virus spreads mostly through the fecal–oral route. People can get infected by direct contact with someone who is sick, by eating or drinking contaminated food or water, or by touching contaminated surfaces [73]. Norovirus is very stable in the environment and can stay infectious on surfaces for several days or even weeks [74, 75, 76]. Because only a very small number of viral particles (as few as 18) are needed to cause infection, outbreaks can spread quickly [77].

Typical symptoms include nausea, vomiting, watery diarrhea, and stomach cramps. The illness usually lasts 1–3 days and often goes away on its own [70]. However, people can become infected again because immunity after infection does not last long and the virus has many different types [78]. The basic reproduction number (R_0) for norovirus is estimated to be between 2 and 7, depending on where and how the virus spreads [79].

Because of its high transmission rate, strong environmental stability, and short-term immunity, norovirus is an important example for studying how epidemics start and spread. Mathematical models that include both person-to-person and environmental transmission help researchers understand outbreak patterns, test control strategies, and predict how long the virus can persist in a community.

In this thesis, we quantify the outcomes of norovirus infection considering environmental transmission.

1.2.5 COVID-19

Coronavirus disease 2019 (COVID-19) is an infectious disease caused by Severe Acute Respiratory Syndrome Coronavirus 2 (SARS-CoV-2), an enveloped, positive-sense single-stranded RNA virus belonging to the genus Betacoronavirus [80, 81]. The virus was first identified in Wuhan, China, in December 2019, and was officially named by the World Health Organization (WHO) on 11 February 2020 [82]. COVID-19 spreads primarily through respiratory droplets and aerosols generated when infected individuals cough, sneeze, or speak, and can also be transmitted via contact with contaminated surfaces [83, 84].

Clinical manifestations vary widely: infected individuals may remain asymptomatic or experience symptoms ranging from mild respiratory illness to severe pneumonia, acute respiratory distress syndrome (ARDS), multi-organ failure, and death [85, 86]. Older adults and individuals with underlying medical conditions, such as diabetes or cardiovascular disease, face a significantly higher risk of severe illness and mortality [87].

Vaccination and non-pharmaceutical interventions (e.g., masking, physical distancing, and improved ventilation) have greatly reduced global morbidity and mortality, though the emergence of new variants continues to pose challenges to disease control and public health responses [88, 89, 90].

The heterogeneous transmission dynamics and diverse clinical outcomes of COVID-19 make it a key system for mathematical modelling of infectious diseases. Models of compartmental epidemic frameworks including bifurcation and stability analyses have been used to describe disease spread, assess intervention strategies, and explore critical thresholds that govern epidemic persistence or elimination [91, 92, 93, 94, 95, 96, 97].

In this thesis, we quantify the outcomes of COVID-19 infection considering environmental transmission.

1.3 Model Frameworks

In this thesis, we utilize deterministic and stochastic models. We also apply models with spatial considerations.

1.3.1 Deterministic Models

Deterministic epidemic models provide a mathematical framework for analyzing the transmission dynamics of infectious diseases through systems of differential or difference equations [98, 99]. In these models, the sizes of the susceptible, infected, and recovered (or otherwise classified) subpopulations are represented as continuous, deterministic functions of time [98]. The interactions among these compartments are governed by rate parameters that describe processes such as infection, recovery, and immunity loss [99]. Classical examples of this approach include the SIR and SEIR models, which have been extensively used to study the temporal evolution of epidemics and to assess the potential impact of intervention strategies [98, 100] .

Deterministic models offer several advantages. The underlying mathematical theory is well established, allowing for rigorous analytical treatment of system behaviour, equilibrium points, and stability conditions. Furthermore, the derivation of these models relies less on empirical data than purely statistical approaches, enabling researchers to perform theoretical explorations and scenario-based predictions with relative ease. However, deterministic models also have notable limitations. When population sizes are small, stochastic fluctuations and random events become increasingly influential, leading to deviations from the deterministic trajectories. Under such circumstances, the assumptions of continuity and large population size inherent in deterministic formulations are violated, and stochastic modelling approaches may provide more accurate representations of disease dynamics [25, 101].

1.3.2 Stochastic Models

Stochastic epidemic models incorporate random variation into the representation of disease transmission and progression, acknowledging that real-world epidemics are inherently influenced by chance events. Unlike deterministic models, which assume that population compartments change continuously and predictably over time, stochastic models describe transitions between states (such as susceptible, infected, and recovered) as probabilistic events. These models are typically formulated using stochastic differential equations, the Gillespie Algorithm (or Monte Carlo Markov Chain, MCMC), or agent-based simulations, allowing them to capture the variability and uncertainty inherent in epidemic processes [101, 102, 25, 103].

The primary advantage of stochastic models lies in their ability to represent random fluctuations that become significant in small populations or during the early stages of an outbreak, when the number of infectious individuals is low. This enables the estimation of outbreak probabilities, extinction times, and the likelihood of epidemic fade-out, all phenomena that deterministic models cannot adequately capture. Moreover, stochastic approaches can provide confidence intervals and distributions of possible outcomes rather than a single deterministic trajectory. However, stochastic models are often mathematically and computationally more complex, requiring extensive simulation or numerical methods [101, 25]. They also tend to depend on more detailed parameterization and larger datasets, which may limit their analytical tractability and generalizability compared to deterministic formulations [25, 104, 105].

In this thesis, we use the Gillespie algorithm and agent-based models.

1.3.2.1 Gillespie Simulation

The Gillespie simulation algorithm [102] is well described by Linda J. S. Allen in An Introduction to Stochastic Processes with Applications to Biology [106]. It is a computational

method that tracks discrete events such as infection, birth, death, and recovery using probabilities determined by the current state of the system. The algorithm calculates both the time until the next event and which event will occur, proceeding step by step to construct a possible trajectory of the epidemic over time. By running the Gillespie algorithm multiple times, one can generate different possible realizations of an epidemic that a population might experience. Some simulation runs may not result in an outbreak, which allows estimation of the probability of epidemic extinction or no outbreak. Furthermore, when the number of infected individuals is small, the infection may die out entirely, and such outcomes can be used to estimate the expected duration or end time of the epidemic.

1.3.2.2 Agent-Based Modelling

In agent-based modelling (ABM), a system is represented as a collection of independent agents that make decisions autonomously. Each agent evaluates its own circumstances and acts according to a predefined set of behavioural rules. Agents can engage in various activities relevant to the system being modeled—such as going to work, attending school, or interacting with other agents—which facilitates potential disease transmission. During the COVID-19 pandemic, ABMs were used extensively to investigate the dynamics of disease spread, hospital demand, and the effectiveness of vaccination and other public health interventions. Notable applications include the work of Vicky Ng and collaborators at the Public Health Agency of Canada (PHAC), who developed ABMs to support national pandemic response planning [107, 108], and Seyed M. Moghadas, who employed agent-based simulations to assess the impact of vaccination and mitigation strategies in the United States [109].

In this thesis, we employ AnyLogic [110], a software program that allows for different types of modelling, including system dynamics, spatial models on maps, discrete-event simulation, and agent-based actions and decision-making. In combination, this allows for the study of infectious diseases in space and time. The software has a visual interface and uses Java

programming, so models can be simple or very detailed.

ABMs have three key advantages over other modelling approaches: (i) ABM is adaptable; (ii) ABM offers a natural description of a system; and (iii) ABM captures emergent events. However, to fulfill its function, the model must be constructed with the proper level of description and with precisely the right amount of information. Additionally, when modelling large systems, ABM's high computing requirements continue to be an issue. Finally, some ABMs have limitations in the number of agents that can be used. For example, using AnyLogic, Vicky Ng and colleagues used 100,000 agents to model all of Canada [108], which is not very realistic.

1.4 Model Tools

To investigate the transmission dynamics of infectious diseases, mathematical modelling serves as a central tool. In this thesis, we develop and analyze compartmental models tailored to specific diseases and settings, namely: (i) a within-host HIV model incorporating a virus loss term, (ii) epidemic models for Measles and Influenza that account for waning immunity, and (iii) a theme park infection risk model (of COVID-19, influenza, norovirus, and measles) to capture transmission considering heterogenous populations, spatial aspects, and environmetal transmission.

The modelling frameworks we employ here primarily rely on systems of nonlinear ordinary differential equations (ODEs). These systems allow for the representation of transitions between health states (e.g., susceptible, infected, recovered, waning), as well as additional biological processes such as viral clearance, vaccination, and reinfection. Symbolic manipulation software (e.g., Maple [111], Mathematica [112]) and numerical computation platforms (e.g., MATLAB [113], Anylogic [110]) are used in parallel: the former for deriving analytic threshold conditions (e.g., reproduction numbers, bifurcation thresholds), and the latter for simulating trajectories, visualizing outcomes, and performing sensitivity analysis.

1.5 Analysis of Model

The analysis of infectious disease models involves both qualitative and quantitative approaches. Qualitative analysis aims to understand the overall behaviour of the system and how the model dynamics change in response to variations in parameters or structural assumptions. Quantitative analysis, on the other hand, focuses on identifying equilibrium points, threshold parameters, and possible bifurcations. It also includes numerical simulations that illustrate the time evolution and magnitude of disease prevalence or viral load under different parameter regimes.

Together, these approaches provide valuable insights into the mechanisms driving disease persistence, eradication, and complex dynamical behaviours such as backward bifurcation and multistability. For HIV, such analysis helps clarify the difficulties of achieving viral clearance in-host. For measles and influenza, the focus lies on the effects of waning immunity and repeated exposures on long-term population dynamics. In the context of measles, influenza, norovirus and COVID-19, the analysis emphasizes the interactions between individuals and their environment, the heterogeneity of contact patterns, and how these factors contribute to infection risk.

1.5.1 Bifurcation Analysis

Bifurcation analysis plays a central role in identifying critical thresholds at which the existence and stability of different model equilibria change. The most common example in epidemiology is the basic reproduction number $\mathcal{R}_0$, which typically separates the stability of the disease-free state to the existence and stability of an endemic state of the disease. However, in nonlinear systems such as those studied here, additional thresholds can emerge.

For the HIV model, we perform a bifurcation analysis on our model to look for bifurcations that can aid us in understanding HIV persistence in individuals with low viral load. Here, a backward bifurcation is of particular interest, as it allows the coexistence of a stable endemic

equilibria even when $\mathcal{R}_0 < 1$. Consequently, reducing $\mathcal{R}_0$ below unity may not guarantee viral clearance. In the measles and influenza models, our analysis emphasizes how waning immunity introduces reinfection loops that can alter the stability of equilibria and shift the effective threshold conditions of the reproduction number. In the environmental transmission project, bifurcation techniques help determine whether contact structure, affecting the basic reproduction number, can induce outbreaks once key parameters (e.g., effective contact rate) cross critical values.

In this thesis, to study bifurcations, we employ analytical methods (e.g., deriving polynomial equilibrium conditions and discriminant thresholds) and numerical continuation methods (using software such as MATCONT [114]).

1.5.2 Stability Analysis

Stability analysis is fundamental to bifurcation analysis, as bifurcations occur when the stability of equilibria changes. Linearization techniques, based on the Jacobian matrix of the system, are used to compute eigenvalues that determine whether small perturbations around equilibria decay (stability) or grow (instability). This provides insight into whether disease-free or endemic states are biologically feasible and sustainable under given parameter regimes [99].

In this thesis, for the HIV model, stability analysis highlights the role of viral clearance and infection parameters in determining persistence of infection. For the measles and influenza models, stability results clarify how waning immunity destabilizes equilibria and can lead to oscillatory dynamics or recurrent outbreaks [25, 104]. In the environmental transmission project, stability analysis reveals whether infection can remain controlled when public health interventions are implemented, or whether small perturbations lead to rapid epidemic spread.

Global stability is also examined where possible, often using Lyapunov functions or comparison theorems [115, 116]. Together, local and global stability results provide a rigorous

foundation for interpreting the biological significance of the models and identifying effective control strategies. In this thesis, global stability analysis is not employed so we do not provide further discussion here.

1.5.3 Sensitivity Analysis

Sensitivity analysis is used as a core computational tool to systematically identify the parameters that exert the greatest influence on disease dynamics and equilibrium outcomes. In this dissertation, we utilize sensitivity analysis to identify which parameters have the greatest impact on infection outcomes in HIV, measles, influenza, and environmental transmission models related to theme parks. We implement Latin Hypercube Sampling (LHS) to achieve an efficient global exploration of parameter uncertainties, and we use Partial Rank Correlation Coefficients (PRCC) to evaluate the strength and direction of the influence of each parameter [117, 118, 119, 120]. This approach allows us to identify the dominant drivers of viral load and equilibrium behavior in the HIV system, quantify how waning immunity and vaccination parameters affect the dynamics of measles and influenza, and determine which environmental and behavioral factors most influence the number of reproduction in the theme-park model. Together, LHS–PRCC provides a consistent and comparative framework to classify ranking intervention relevant parameters in all disease settings studied in this thesis.

Sensitivity analysis was conducted using a variance free global framework based on Latin Hypercube Sampling (LHS) combined with Partial Rank Correlation Coefficients (PRCC). LHS is a stratified Monte Carlo sampling technique that efficiently generates representative samples from multidimensional parameter spaces by ensuring that the full range of each parameter is explored with minimal sample size [120, 119]. This approach allows simultaneous variation of all model parameters over their biologically feasible ranges and provides a robust characterization of parameter uncertainty.

PRCC is a rank-based statistical measure that quantifies the strength and direction of the

monotonic (possibly nonlinear) relationships between individual parameters and the model output, while taking into account the influence of other parameters [117, 118]. Unlike local sensitivity measures, PRCC captures nonlinear dependencies and interaction effects among parameters, making it well suited for complex epidemic and within-host models. Together, the LHS–PRCC framework provides a reliable and computationally efficient global sensitivity methodology for identifying dominant parameters governing viral load, outbreak persistence, and intervention thresholds across all disease systems considered in this thesis.

1.6 Thesis outline

This thesis is structured as follows:

Chapter 2 develops and analyzes a within-host HIV model, taking into account virus loss dynamics. Chapter 3 investigates a measles model with waning immunity and derives vaccination thresholds. Chapter 4 extends the analysis to seasonal influenza, incorporating inter-seasonal immune effects. Chapter 5 investigates the infectious disease transmission in a theme park setting. We first consider a deterministic ODE based model to examine the spread of multiple infectious diseases, including COVID-19, influenza, measles, and norovirus. These diseases are chosen to represent a variety of epidemiological characteristics, such as differences in transmissibility, infectious duration, and parameter structures. Also, we develop an agent-based model to capture individual level interactions and more detailed transmission dynamics in the theme park environment. Chapter 6 concludes the thesis and outlines future research options.

Chapter 2

In-host modelling with immunity and virus loss term

This chapter is submitted for publication.

2.1 Introduction

Mathematical models have aided in the understanding of HIV infection and the development of drug treatments. They have also been used to study the inability of drug therapies to eliminate the virus from infected individuals. Examples of such modelling studies can be found in [18, 21, 121, 122, 123, 124, 125, 126, 127, 128, 129]. Recently, Xie et al. [130] studied a model of HIV infection with bi-stability and backward bifurcation whereby there is coexistence and stability of disease-free and infected equilibria when the basic reproduction number of the virus is below unity -- which can render viral clearance impossible. They showed that backward bifurcation may be caused by the activation and proliferation of healthy naive CD4 T cells to become helper T cells, as this process creates new target cells in the presence of the virus.

The model of Xie et al.[130] (and the vast majority of models of HIV infection) ignore

the virus loss term, a term that represents the loss of virus particles due to the infection of a target cell. A common assumption is that virus loss is dominated by the clearance rate of the virus (i.e., virus clearance much greater than virus loss into target cells due to cell infection), and therefore, this term can be ignored. Additionally, ignoring this term allows for an uncoupling of the virus dynamics equation in a mathematical model from the rest of the system, allowing for a simpler model to analyse mathematically.

In previous work, it was found that ignoring the virus loss can reduce the richness in bifurcations of an in-host model of virus infection and therefore miss components of the biology of infection that can inform intervention and treatment [131, 132, 133]. Here, we expand the model of Xie et al. [130] by adding a virus loss term to the virus equation to account for additional viral clearance mechanisms and investigate how this modification influences the systems dynamics. Our model is thus more biologically faithful and provides more reliable thresholds and therapy predictions, while keeping the elegant bifurcation logic of Xie et al. [130].

In this Chapter, we introduce our model, present analytical and numerical results related to the model equilibria, basic reproduction number, bifurcations, and sensitivity analysis. We conclude with a discussion relevant to the virus loss term, richness of bifurcations, and relation to HIV infection outcomes.

2.2 Model Formulation

The model considers target cells and virus. The target cells reside in three classes: uninfected naive T-cells ($\bar{T}$), uninfected helper T-cells ($\bar{T}_H$), and productively infected T-cells ($\bar{I}$). There

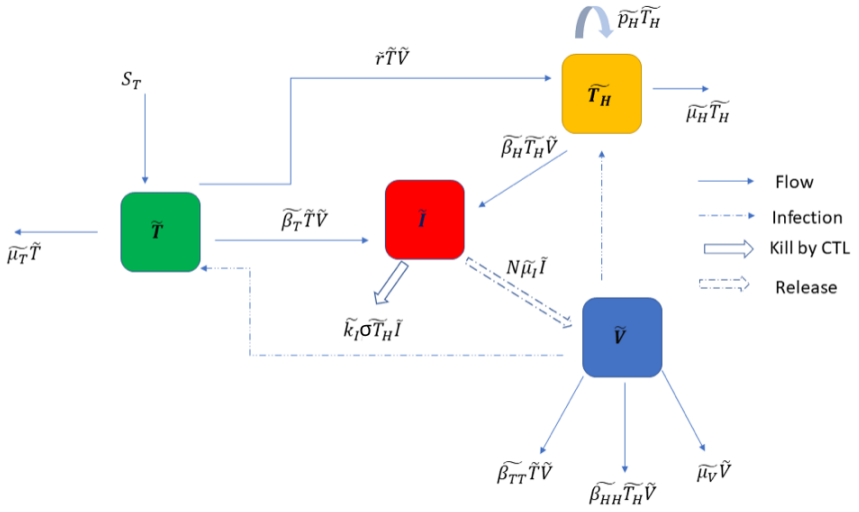

Figure 2.1: Model flow diagram

is one class of virus ($\bar{V}$). The model is given by the four dimensional system:

$$\begin{aligned}
\frac{d\bar{T}}{d\tau} &= S_T - \bar{r}\bar{T}\bar{V} - \bar{\beta}_T\bar{T}\bar{V} - \bar{\mu}_T\bar{T} \\
\frac{d\bar{T}_H}{d\tau} &= \bar{r}\bar{T}\bar{V} - \bar{\beta}_H\bar{T}_H\bar{V} - \bar{\mu}_H\bar{T}_H + \bar{p}_H\bar{T}_H \\
\frac{d\bar{I}}{d\tau} &= \bar{\beta}_H\bar{T}_H\bar{V} + \bar{\beta}_T\bar{T}\bar{V} - \bar{\mu}_I\bar{I} - \bar{k}_I\sigma\bar{T}_H I \\
\frac{d\bar{V}}{d\tau} &= N\bar{\mu}_I\bar{I} - \bar{\mu}_V\bar{V} - \bar{\beta}_{TT}\bar{T}\bar{V} - \bar{\beta}_{HH}\bar{T}_H\bar{V}
\end{aligned} \tag{2.1}$$

Briefly, uninfected T-cells have a production rate S_T and death rate $\bar{\mu}_T$. Helper T-cells are produced through activation of uninfected T-cells by the viral particles ($\bar{r}\bar{T}\bar{V}$) and can proliferate at rate ($\bar{p}_H\bar{T}_H$). $\bar{\beta}_T$ and $\bar{\beta}_H$ are the infection rates of $\bar{T}$ and $\bar{T}_H$ cells, respectively, which result in the loss of virus into the target cells with rates $\bar{\beta}_{TT}$ and $\bar{\beta}_{HH}$, respectively. Infected cells can be removed from the system through natural death ($\bar{\mu}_I$) or by immune system killing ($\bar{k}_I\sigma\bar{T}_H$). It is assumed that N free virus particles are released when an infected cell dies. Free virus are cleared at constant rate $\bar{\mu}_V$. Figure 2.1 shows the model flow diagram. The initial conditions are given by $\bar{T} > 0$, $\bar{T}_H > 0$, $\bar{I} > 0$, $\bar{V} > 0$. All parameters are positive and $\bar{\mu}_H > \bar{p}_H$ for boundedness.

Parameter	Interpretation	Values
S_T	Production rate of healthy naive CD4 T cells (cells/day)	5.425×10^8
μ_T	Natural death rate of naive CD4 T cells	3.875
μ_H	Natural death rate of helper T_H cells	3.875
β_T	Infection rate of naive CD4 T cells by virus	525
β_H	Infection rate of helper T_H cells by virus	525
β_{TT}	Virus loss rate through infection of CD4 T cells	0.001
β_{HH}	Virus loss rate through infection of helper T_H cells	0.001
r	Stimulation rate of naive CD4 T cells by the presence of virus	525
p_H	Proliferation rate of helper T_H cells	1.5
k_I	Killing rate of infected cells by the immune system	1750
μ_I	Death rate of infected cells	3.875
μ_V	Natural Death rate of Virus	3.875
N	Average virus produced by an infected cell at death	300
σ	$\sigma\bar{T}_H$ represents the immune response that can effectively kill infected cells	$1.1525 - 1.1625$

Table 2.1: Parameter values for the non-dimensional system (Model 2.2). Parameter values except β_{TT} and β_{HH} come from Hogue *et al.* model [125] and Xie *et al.* model [130]

A non-dimensional model corresponding to Model (2.1) can be determined by setting: $\bar{T} = S_T T/\bar{\mu}_T$, $\bar{T}_H = S_T T_H/\bar{\mu}_T$, $\bar{I} = S_T I/\bar{\mu}_T$, $\bar{V} = NS_T V/\bar{\mu}_T$, $\tau = t/\bar{\mu}_V$, $\bar{k}_I = k_I\bar{\mu}_T\bar{\mu}_V/(S_T)$, $\bar{r} = r\bar{\mu}_T\bar{\mu}_V/(NS_T)$, $\bar{\beta}_H = \beta_H\bar{\mu}_T\bar{\mu}_V/(NS_T)$, $\bar{\beta}_T = \beta_T\bar{\mu}_T\bar{\mu}_V/(NS_T)$, $\bar{\beta}_{HH} = \beta_{HH}\bar{\mu}_T\bar{\mu}_V/(S_T)$, $\bar{\beta}_{TT} = \beta_{TT}\bar{\mu}_T\bar{\mu}_V/(S_T)$, $\bar{\mu}_I = \mu_I\bar{\mu}_V$, $\bar{\mu}_T = \mu_T\bar{\mu}_V$, $\bar{\mu}_H = \mu_H\bar{\mu}_V$ and $\bar{p}_H = p_H\bar{\mu}_V$. The non-dimensional model is given by:

$$\begin{aligned}
\tfrac{dT}{dt} &= \mu_T - rTV - \beta_T TV - \mu_T T \\
\tfrac{dT_H}{dt} &= rTV - \beta_H T_H V - \mu_H T_H + p_H T_H \\
\tfrac{dI}{dt} &= \beta_H T_H V + \beta_T TV - \mu_I I - k_I\sigma T_H I \\
\tfrac{dV}{dt} &= \mu_I I - V - \beta_{TT} TV - \beta_{HH} T_H V
\end{aligned} \tag{2.2}$$

Model parameter values are listed in Table 2.1.

2.3 Results

2.3.1 Disease Free equilibrium

Model (2.2) has a disease free equilibrium (DFE) $E^0 = (T^0, T_H^0, I, V) = (1, 0, 0, 0)$.

The Jacobian matrix of Model (2.2) evaluated at E^0 is

$$J_0 = \begin{pmatrix} -\mu_T & 0 & 0 & -(r+\beta_T) \\ 0 & -d_H & 0 & r \\ 0 & 0 & -\mu_I & \beta_T \\ 0 & 0 & \mu_I & -\beta_{TT} - 1 \end{pmatrix}$$

where, $d_H = \mu_H - p_H > 0$. The eigenvalues of J_0 are $-\mu_T$, $-d_H$ and the solutions of the quadratic equation $\lambda^2 + (\mu_I + 1 + \beta_{TT})\lambda + \mu_I(1 - (\beta_T - \beta_{TT})) = 0$. Eigenvalues $-\mu_T$ and $-d_H$ are both less than zero. Therefore, if the roots of the quadratic equation are negative, the condition of stability is satisfied; otherwise, E_0 is not stable. Note that the solutions of the quadratic are negative if and only if $\beta_T - \beta_{TT} < 1$.

2.3.2 Basic Reproduction Number

The basic reproduction number is

$$\begin{aligned} \mathcal{R}_0 &= \beta_T - \beta_{TT} \\ &= \frac{(N\bar{\beta}_T - \bar{\beta}_{TT})S_T}{\bar{\mu}_V \bar{\mu}_T} \end{aligned} \tag{2.3}$$

We note that when $\mathcal{R}_0 < 1$ or $\dfrac{\beta_T}{1+\beta_{TT}} < 1$, the DFE is stable. Otherwise, it is unstable.

2.3.3 Infected Equilibrium

The infected equilibria are defined by (T^*, T_H^*, I^*, V^*) where,

$$T^* = \frac{\mu_T}{\mu_T + rV^* + \beta_T V^*}$$

$$T_H^* = \frac{rV^*}{\beta_H V^* + d_H} \frac{\mu_T}{\mu_T + rV^* + \beta_T V^*}$$

$$I^* = \frac{V^*}{\mu_I} \left((\beta_T - \mathcal{R}_0) \frac{\mu_T}{\mu_T + rV^* + \beta_T V^*} + \beta_{HH} \frac{rV^*}{\beta_H V^* + d_H} \frac{\mu_T}{\mu_T + rV^* + \beta_T V^*} + 1 \right)$$

and V satisfies

$$AV^{*4} + BV^{*3} + CV^{*2} + FV^* + G = 0 \tag{2.4}$$

with

$$\begin{aligned}
A &= -\mu_I \beta_H^2 (r + \beta_T)^2 \\
B &= (r + \beta_T)\beta_H((((\beta_H - \beta_{HH})r + \beta_H(\mathcal{R}_0 - 2))\mu_T + 2(p_H - \mu_H)(r + \beta_T))\mu_I - k_Y \mu_T r \sigma) \\
C &= ((-\beta_H((\beta_{HH} - \beta_H)r - \beta_H(\mathcal{R}_0 - 1))\mu_T^2 + (r + \beta_T)((\beta_{HH} - \beta_H)r \\
&\quad -2\beta_H(\mathcal{R}_0 - 2))(p_H - \mu_H)\mu_T - (p_H - \mu_H)^2(r + \beta_T)^2)\mu_I \\
&\quad +k_I r((-\beta_{HH} r - \beta_H(\beta_T - \mathcal{R}_0 + 1))\mu_T + (-\mu_H + p_H)(r + \beta_T))\sigma\mu_T) \\
F &= ((((\beta_{HH} - \beta_H)r - 2\beta_H(\mathcal{R}_0 - 1))\mu_T + (p_H - \mu_H)(\mathcal{R}_0 - 2)(r + \beta_T))\mu_I \\
&\quad +\sigma r k_I \mu_T(\beta_T - \mathcal{R}_0 + 1))(p_H - \mu_H)\mu_T \\
G &= \mu_T^2 \mu_I (p_H - \mu_H)^2(\mathcal{R}_0 - 1)
\end{aligned}$$

We note that there can be multiple positive roots of the equation for V^*. Due to the complexity of solving for V^*, we leave this for numerical calculation.

The Jacobian matrix of Model (2.2) evaluated at the endemic equilibrium

$$E^* = (T^*, T_H^*, I^*, V^*)$$

is:

$$J^* = \begin{pmatrix} a_{11} & a_{12} & a_{13} & a_{14} \\ a_{21} & a_{22} & a_{23} & a_{24} \\ a_{31} & a_{32} & a_{33} & a_{34} \\ a_{41} & a_{42} & a_{43} & a_{44} \end{pmatrix}$$

where,

$$a_{11} = -V^*(\beta_T + r) - \mu_T, \quad a_{12} = 0, \quad a_{13} = 0, \quad a_{14} = -T^*(\beta_T + r)$$

$$a_{21} = V^* r, \quad a_{22} = -V^*\beta_H - d_H, \quad a_{23} = 0, \quad a_{24} = T^* r - T_H^*\beta_H,$$

$$a_{31} = V^*\beta_T = V^*(\mathcal{R}_0 + \beta_{TT}), \quad a_{32} = -I^*\sigma k_I + V^*\beta_H, \quad a_{33} = -T_H^*\sigma k_I - \mu_I, \quad a_{34} = T^*\beta_T + T_H^*\beta_H,$$

$$a_{41} = -V^*(\beta_T - \mathcal{R}_0), \quad a_{42} = -V^*\beta_{HH}, \quad a_{43} = \mu_I, \quad a_{44} = -T^*(\beta_T - \mathcal{R}_0) - T_H^*\beta_{HH} - 1$$

The characteristic equation of J^* is

$$\lambda^4 + p_1\lambda^3 + p_2\lambda^2 + p_3\lambda + p_4 = 0$$

where,

$$p_1 = \quad -a_{44} - a_{33} - a_{22} - a_{11},$$

$$\begin{aligned} p_2 = \quad & (a_{33} + a_{44} + a_{22})a_{11} + (a_{33} + a_{44})a_{22} - a_{23}a_{32} + \\ & a_{33}a_{44} - a_{34}a_{43} - a_{14}a_{41} - a_{24}a_{42} - a_{12}a_{21} - a_{13}a_{31}, \end{aligned}$$

$$\begin{aligned} p_3 = \quad & ((-a_{33} - a_{44})a_{22} + a_{23}a_{32} - a_{33}a_{44} + a_{34}a_{43} + a_{24}a_{42})a_{11} + (a_{13}a_{31} + a_{14}a_{41} \\ & -a_{33}a_{44} + a_{34}a_{43})a_{22} + (a_{12}a_{21} + a_{14}a_{41} + a_{24}a_{42})a_{33} + (a_{12}a_{21} + a_{13}a_{31} + a_{23}a_{32})a_{44} \\ & +(-a_{23}a_{31} - a_{24}a_{41})a_{12} + (-a_{21}a_{32} - a_{34}a_{41})a_{13} + (-a_{21}a_{42} - a_{31}a_{43})a_{14} \\ & -a_{24}a_{32}a_{43} - a_{23}a_{34}a_{42}, \end{aligned}$$

$$
\begin{aligned}
p_4 = \; & ((a_{33}a_{44} - a_{34}a_{43})a_{22} + (-a_{32}a_{44} + a_{34}a_{42})a_{23} + a_{24}(a_{32}a_{43} - a_{33}a_{42}))a_{11} \\
& +((-a_{33}a_{44} + a_{34}a_{43})a_{21} + (a_{31}a_{44} - a_{34}a_{41})a_{23} + a_{24}(-a_{31}a_{43} + a_{33}a_{41}))a_{12} \\
& +((a_{32}a_{44} - a_{34}a_{42})a_{21} + (-a_{31}a_{44} + a_{34}a_{41})a_{22} - a_{24}(-a_{31}a_{42} + a_{32}a_{41}))a_{13} \\
& +a_{14}((-a_{32}a_{43} + a_{33}a_{42})a_{21} + (a_{31}a_{43} - a_{33}a_{41})a_{22} + a_{23}(-a_{31}a_{42} + a_{32}a_{41})).
\end{aligned}
$$

The Routh-Hurwitz stability criterion [134] is $p_1 > 0$, $p_3 > 0$, $p_4 > 0$ and $p_1 p_2 p_3 - p_3^2 - p_1^2 p_4 > 0$. We leave the determination of the eigenvalues for the infected equilibria to numerical calculation.

2.3.4 Bifurcation Analysis

Solutions of Eq. (2.4) depend on the value of $\mathcal{R}_0$. Similar to [135, 136, 130], we utilize $\mathcal{R}_0$ as a bifurcation parameter.

We now consider the existence of a backward bifurcation. Our model consists of four compartments defined as $x = (x_1, x_2, x_3, x_4)^T = (T, T_H, I, V)^T$ and $f_i = \dfrac{dx_i}{dt}$ for the non-dimensional system. The disease free equilibrium is $E_0 = (T^0, T_H^0, I^0, V^0) = (1, 0, 0, 0)$. The linearization of System (2.2) at the bifurcation point $\mathcal{R}_0 = 1$ or $\beta_T = 1 + \beta_{TT}$ yields

$$
J_0 = \begin{bmatrix}
-\mu_T & 0 & 0 & -(r + \beta_{TT} + 1) \\
0 & -(\mu_H - p_H) & 0 & r \\
0 & 0 & -\mu_I & \beta_{TT} + 1 \\
0 & 0 & \mu_I & -(\beta_{TT} + 1)
\end{bmatrix}
$$

The eigenvalues of the matrix are: $-\mu_T, -(\mu_H - p_H), -(\mu_I + \beta_{TT} + 1)$ and 0 and the

corresponding left eigenvector $\mathbf{v}^T$ and right eigenvector $\mathbf{w}$ at eigenvalue zero are:

$$\mathbf{v} = \begin{bmatrix} 0 \\ 0 \\ \frac{\mu_I}{\mu_I+\beta_{TT}+1} \\ \frac{\mu_I}{\mu_I+\beta_{TT}+1} \end{bmatrix}, \qquad \text{and} \qquad \mathbf{w} = \begin{bmatrix} \frac{-(r+\beta_{TT}+1)}{\mu_T} \\ \frac{r}{d_H} \\ \frac{\beta_{TT}+1}{\mu_I} \\ 1 \end{bmatrix}.$$

The theorems of backward bifurcation found in [135, 136] ensure that, if

$$\mathbf{b} = \sum_{i,j=1}^{4} v_i w_j \frac{\delta^2 f_i}{\delta x_j \delta \mathcal{R}_0}(E^0, 1) > 0$$

and

$$\mathbf{a} = \frac{1}{2} \sum_{i,j,k=1}^{4} v_i w_j w_k \frac{\delta^2 f_i}{\delta x_j \delta x_k}(E^0, 1) > 0$$

there is a backward bifurcation at $R_0 = 1$. Alternatively, there will not be a backward bifurcation if $b > 0$ and $a < 0$.

The nonzero second derivatives in $\mathbf{b}$ are

$$\frac{\delta^2 f_1}{\delta x_4 \delta \mathcal{R}_0}(E^0, 1) = -1 \qquad \text{and} \qquad \frac{\delta^2 f_3}{\delta x_4 \delta \mathcal{R}_0}(E^0, 1) = 1.$$

Thus,

$$\mathbf{b} = v_1 w_4 \frac{\delta^2 f_1}{\delta x_4 \delta \mathcal{R}_0}(E^0, 1) + v_3 w_4 \frac{\delta^2 f_3}{\delta x_4 \delta \mathcal{R}_0}(E^0, 1) = \frac{\mu_I}{\mu_I + \beta_{TT} + 1} > 0.$$

The nonzero second derivatives in $\mathbf{a}$ are

$$\frac{\delta^2 f_1}{\delta x_1 \delta x_4}(E^0, 1) = -\beta_{TT} - 1 - r, \qquad \frac{\delta^2 f_1}{\delta x_4 \delta x_1}(E^0, 1) = -\beta_{TT} - 1 - r,$$

$$\frac{\delta^2 f_2}{\delta x_1 \delta x_4}(E^0, 1) = r, \qquad \frac{\delta^2 f_2}{\delta x_4 \delta x_1}(E^0, 1) = r,$$

$$\frac{\delta^2 f_2}{\delta x_2 \delta x_4}(E^0,1) = -\beta_H, \qquad \frac{\delta^2 f_2}{\delta x_4 \delta x_2}(E^0,1) = -\beta_H,$$

$$\frac{\delta^2 f_3}{\delta x_2 \delta x_3}(E^0,1) = -\sigma k_I, \qquad \frac{\delta^2 f_3}{\delta x_3 \delta x_2}(E^0,1) = -\sigma k_I,$$

$$\frac{\delta^2 f_3}{\delta x_4 \delta x_1}(E^0,1) = \beta_{TT} + 1, \qquad \frac{\delta^2 f_3}{\delta x_1 \delta x_4}(E^0,1) = 0,$$

$$\frac{\delta^2 f_3}{\delta x_4 \delta x_2}(E^0,1) = \beta_H, \qquad \frac{\delta^2 f_3}{\delta x_2 \delta x_4}(E^0,1) = \beta_H,$$

$$\frac{\delta^2 f_4}{\delta x_1 \delta x_4}(E^0,1) = -\beta_{TT}, \qquad \frac{\delta^2 f_4}{\delta x_4 \delta x_1}(E^0,1) = -\beta_{TT},$$

$$\frac{\delta^2 f_4}{\delta x_2 \delta x_4}(E^0,1) = -\beta_{HH}, \qquad \frac{\delta^2 f_4}{\delta x_4 \delta x_2}(E^0,1) = -\beta_{HH}.$$

Thus,

$$\begin{aligned}
\mathbf{a} &= \tfrac{1}{2}\Big[v_3 w_2 w_3 \tfrac{\delta^2 f_3}{\delta x_2 \delta x_3} + v_3 w_2 w_4 \tfrac{\delta^2 f_3}{\delta x_2 \delta x_4} + v_3 w_3 w_2 \tfrac{\delta^2 f_3}{\delta x_3 \delta x_2} + v_3 w_4 w_1 \tfrac{\delta^2 f_3}{\delta x_4 \delta x_1} \\
&\quad + v_3 w_4 w_2 \tfrac{\delta^2 f_3}{\delta x_4 \delta x_2} + v_4 w_1 w_4 \tfrac{\delta^2 f_4}{\delta x_1 \delta x_4} + v_4 w_2 w_4 \tfrac{\delta^2 f_4}{\delta x_2 \delta x_4} + v_4 w_4 w_1 \tfrac{\delta^2 f_4}{\delta x_4 \delta x_1} + v_4 w_4 w_2 \tfrac{\delta^2 f_4}{\delta x_4 \delta x_2}\Big] \\
&= \tfrac{\mu_I}{(\mu_I + \beta_{TT} + 1)}\left[\tfrac{r\beta_H}{d_H} - \tfrac{r(1+\beta_{TT})\sigma k_I}{\mu_I d_H} + \tfrac{(\beta_{TT}+1+r)(\beta_{TT}-1)}{2\mu_T} - \tfrac{r\beta_{HH}}{d_H}\right]
\end{aligned}$$

The following theorem applies.

Theorem 1. *There is a forward bifurcation at $\mathcal{R}_0 = 1$ if $a < 0$ and there is a backward bifurcation at $\mathcal{R}_0 = 1$ if $a > 0$ [135, 136, 130].*

We leave a study of the existence of other bifurcations to our numerical analysis.

2.3.5 Numerical Analysis

2.3.5.1 Model Equilibria

The existence of model equilibria is examined using 2000 parameter sets using eleven parameters ($\mu_T, \beta_H, \mu_H, \beta_{TT}, \beta_{HH}, \beta_T, r, k_I, \mu_I, p_H, \sigma$) chosen in a Latin Hypercube. The mean value for each parameter is given in Table 2.1. Ranges for each parameter were chosen over

uniform distributions with minimum (min) and maximum (max) values given by 50% and 150% of the mean, respectively. 124 of the parameter sets give a disease free equilibrium only. 1807 parameter sets have a disease free equilibrium and one infected equilibrium. The remaining 69 parameter sets have a disease free equilibrium and two infected equilibria. These 69 parameter sets satisfy the condition for backward bifurcation.

2.3.5.2 Basin of Attraction Analysis

To assess how the initial viral inoculum influences long–term outcomes, we computed basin-of-attraction curves by simulating Model (2.2) on a grid of initial virus loads $V(0)$ and several values of the basic reproduction number $\mathcal{R}_0 = \beta_T - \beta_{TT}$. For each run, the system was integrated with a stiff solver until the vector field norm fell below a small tolerance, and the *final* virus load $V(t_{\text{end}})$ was recorded. We varied the virus-loss parameters β_{TT} and β_{HH} together to examine how clearance strength shapes the basins.

Weak viral loss ($\beta_{TT} = \beta_{HH} = 0.001$). Figure 2.2(top) shows a clear *threshold* near $V(0) \approx 8 \times 10^{-3}$: for $V(0)$ below this value trajectories converge to the DFE ($V \to 0$), whereas above it they approach a positive endemic level V^*. This dose dependence indicates *bistability*: for $\mathcal{R}_0 \in (R_c, 1)$ both DFE and EE are locally stable. In Section 2.3.4 we confirm this with a backward bifurcation and a fold at $R_c \approx 0.713$; the separatrix in the basin corresponds to the unstable branch there.

Moderate viral loss ($\beta_{TT} = \beta_{HH} = 0.5$). Figure 2.2(middle) exhibits a (numerically) narrow separatrix at larger $V(0)$, implying a smaller endemic basin and higher inoculum needed for persistence. This reflects a weakened backward regime that moves toward forward behaviour as clearance strengthens.

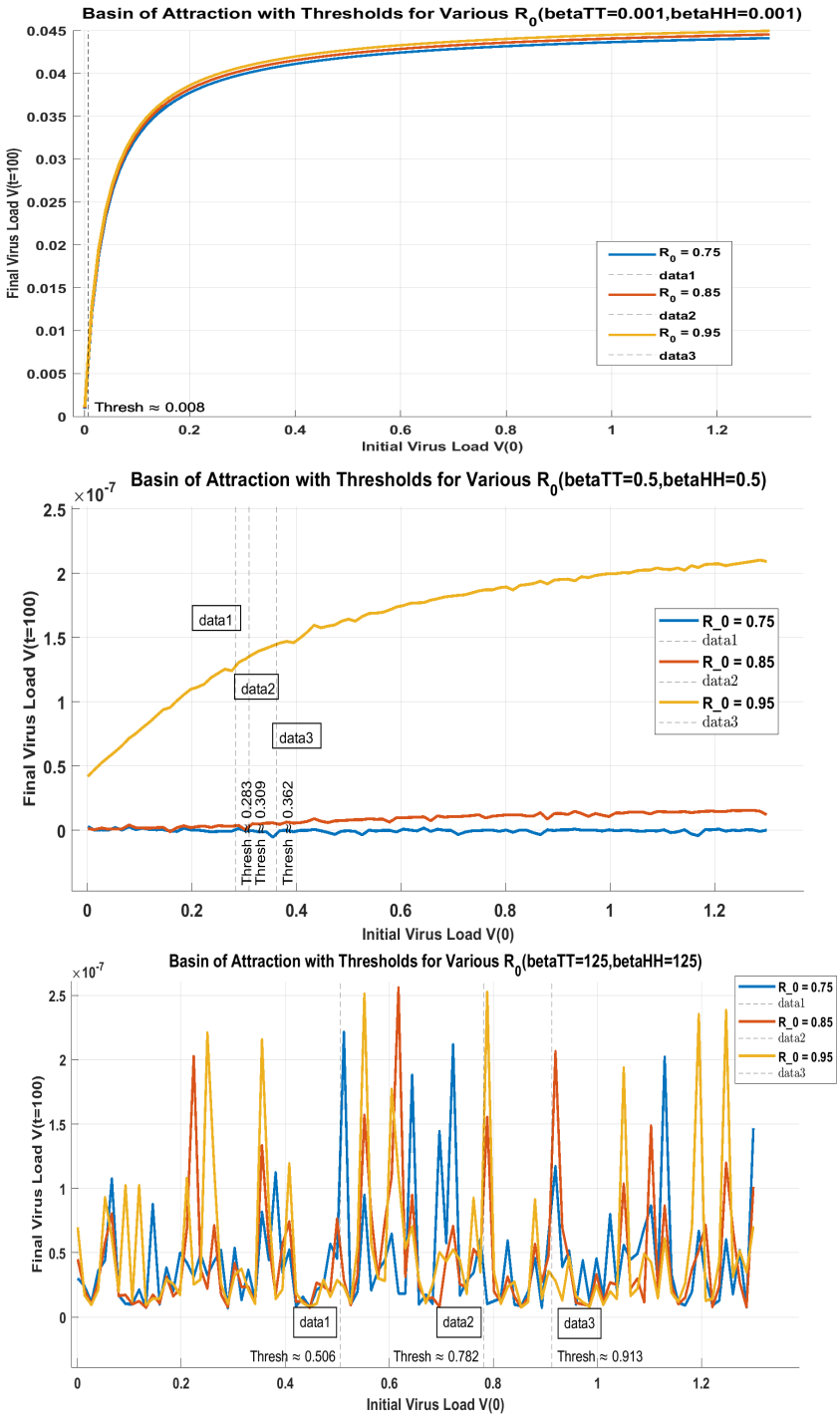

Figure 2.2: Basins of attraction: final virus load $V(t_{\text{end}})$ versus initial inoculum $V(0)$ for several $\mathcal{R}_0$ values and three virus-loss strengths $\beta_{TT} = \beta_{HH} \in \{0.001,\ 0.5,\ 125\}$. Vertical dashed lines (when present) mark the inoculum threshold separating the disease-free equilibrium (DFE) from the endemic equilibrium (EE). Unless otherwise indicated, parameters are $\mu_T = 3.875$, $\mu_H = 3.875$, $\mu_I = 3.875$, $r = 525$, $\beta_H = 525$, $k_I = 1750$, $p_H = 1.5$, and $\sigma = 1.1575$; β_T is set so that $\mathcal{R}_0 = \beta_T - \beta_{TT}$. Baseline values follow Hogue *et al.* [125] and Xie *et al.* [130].

Strong viral loss ($\beta_{TT} = \beta_{HH} = 125$). In Figure 2.2(bottom) all trajectories with $\mathcal{R}_0 < 1$ converge to the DFE regardless of inoculum, indicating disappearance of bistability and a *forward* pattern: endemic states arise only when $\mathcal{R}_0 > 1$.

Together, these basins demonstrate that inoculum size and viral clearance act jointly to determine within-host persistence. Moderate clearance generates a bistable window where early reductions in $V(0)$ (e.g., post-exposure prophylaxis) can push trajectories into the DFE basin even when $\mathcal{R}_0 > R_c$. Very strong clearance removes the window altogether and ensures elimination unless $\mathcal{R}_0$ is driven well above 1. This qualitative picture is consistent with the bifurcation structure presented next.

2.3.5.3 Bifurcation Analysis

Our bifurcation analysis shows that the HIV within-host model with the virus loss term admits both forward and backward bifurcations at the threshold $\mathcal{R}_0 = 1$. Numerical results confirm the theoretical predictions of Theorem 1 and highlight how immune parameters determine the bifurcation type.

Figure 2.3 illustrates that the immune response strength σ governs the transition between different dynamics. For relatively low values ($\sigma = 1.1525$), the system exhibits bistability: the disease-free equilibrium (DFE) coexists with a stable endemic equilibrium even when $\mathcal{R}_0 < 1$. At an intermediate value ($\sigma = 1.1575$), a backward bifurcation occurs, whereby both the DFE and an endemic state remain stable below the threshold. Increasing σ further ($\sigma = 1.1625$) produces the classical forward bifurcation, where infection persists only if $\mathcal{R}_0 > 1$.

A similar pattern is observed when varying the immune killing rate k_I (Figure 2.4). Lower values (e.g. $k_I = 1734$) yield bistability, intermediate values (e.g. $k_I = 1742$) lead to backward bifurcation, and higher values (e.g. $k_I = 1747$) restore the forward bifurcation. Thus, the effectiveness of immune killing (k_I) and the responsiveness of helper T cells (σ) each play a critical role in shaping the infection outcome.

From a biological perspective, the presence of backward bifurcation has important implications: reducing $\mathcal{R}_0$ below unity may not guarantee viral clearance, since a stable endemic equilibrium can still persist. This reflects the difficulty of eradicating HIV, as latent reservoirs and continuous supply of target cells allow infection to be maintained despite unfavorable replication conditions. In contrast, when the system undergoes forward bifurcation, classical threshold behavior applies—viral clearance is ensured once $\mathcal{R}_0 < 1$.

Figure 2.5 further shows that increasing the stimulation rate of naïve $CD4^+$ T cells (r) promotes backward bifurcation by providing a continuous supply of new target cells, which supports viral persistence and bistability. Conversely, smaller values of r lead to a forward bifurcation, eliminating the bistable region and resulting in a single stable equilibrium corresponding to infection clearance. These results illustrate how immune activation and target-cell regeneration critically influence whether the infection outcomes exhibit bistability or a simple threshold behavior.

Overall, incorporating the virus loss term modifies the bifurcation structure of the model, allowing us to capture biologically realistic scenarios of HIV persistence under sub-threshold conditions. This aligns with clinical observations that HIV eradication is rarely achieved, and highlights that therapeutic strategies must target both viral replication and host cell dynamics to ensure durable clearance.

2.3.5.4 Sensitivity Analysis

Our investigation into parameter sets exhibiting multiple infected equilibria and a disease-free equilibrium provides valuable insights into the complex dynamics of the immunological model. Our analysis focuses on the correlations between key parameters and the equilibrium values of target cells (T), helper cells (T_H), infected cells (I), and virus particles (V). Understanding these relationships is crucial for elucidating the underlying mechanisms governing disease spread and control.

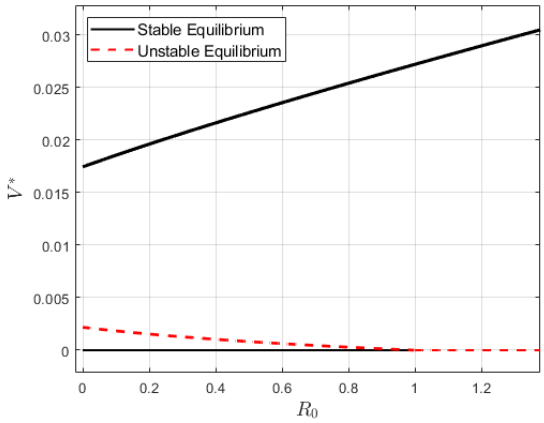

(a) Bistability when $\sigma = 1.1525$

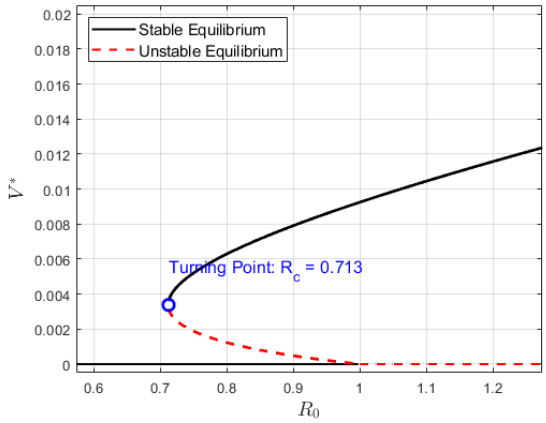

(b) Backward bifurcation when $\sigma = 1.1575$

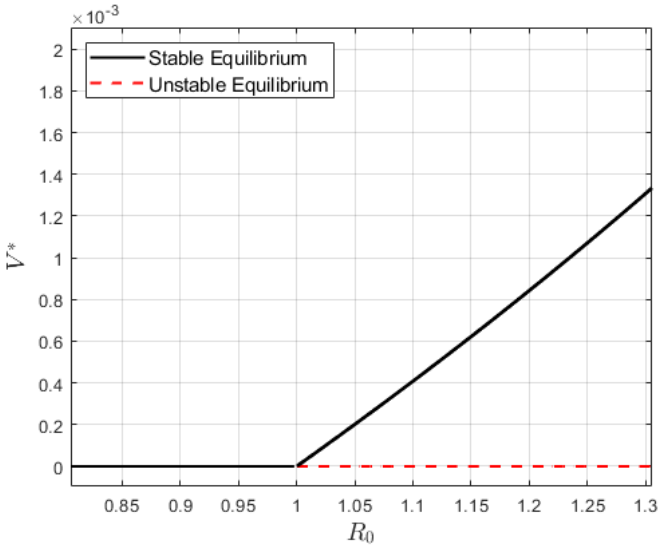

(c) Forward bifurcation when $\sigma = 1.1625$

Figure 2.3: Bifurcation diagram with $\mathcal{R}_0$ as the bifurcation parameter. Here $\mu_H = 3.3875$, $\mu_T = 3.875$, $\mu_I = 3.875$, $r = 525$, $\beta_H = 525$, $\beta_{TT} = 0.001$, $\beta_{HH} = 0.001$. Parameter values except β_{TT} and β_{HH} come from Hogue *et al.* model [125] and Xie *et al.* model [130].

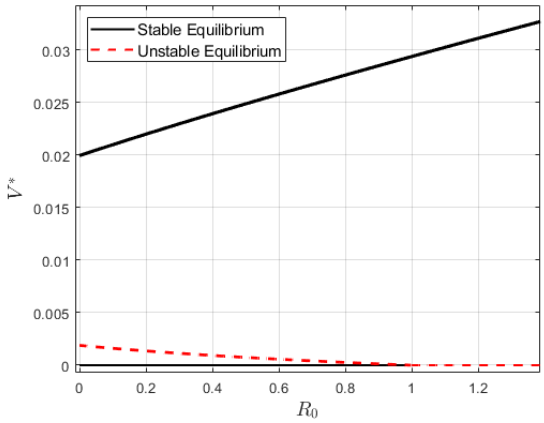

(a) Bistability when $k_I = 1734$

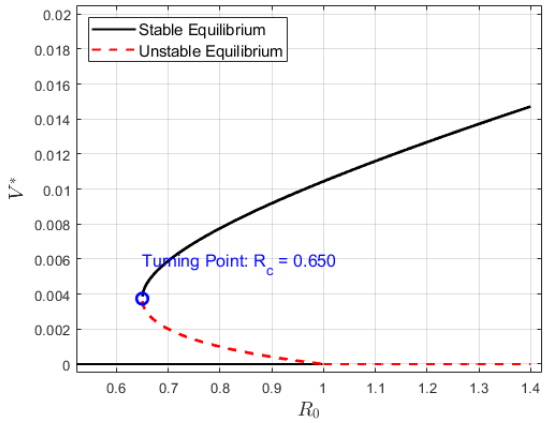

(b) Backward bifurcation when $k_I = 1742$

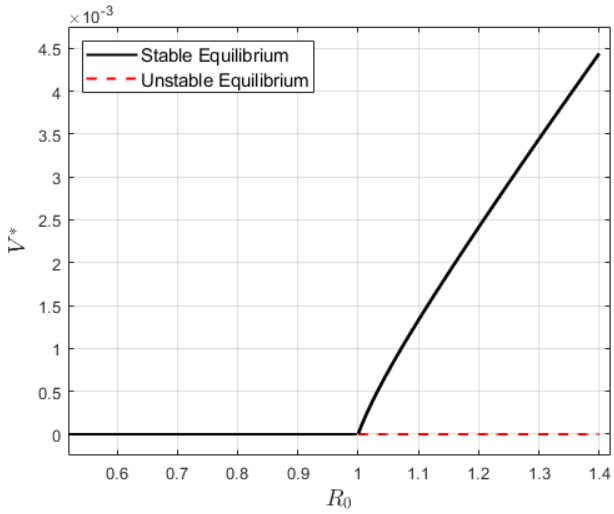

(c) Forward bifurcation when $k_I = 1747$

Figure 2.4: Bifurcation diagram with $\mathcal{R}_0$ as the bifurcation parameter. Here $\mu_H = 3.3875$, $\mu_T = 3.875$, $\mu_I = 3.875$, $r = 525$, $\beta_H = 525$, $\beta_{TT} = 0.001$, $\beta_{HH} = 0.001$. Parameter values except k_I, β_{TT} and β_{HH} come from Hogue *et al.* model [125] and Xie *et al.* model [130].

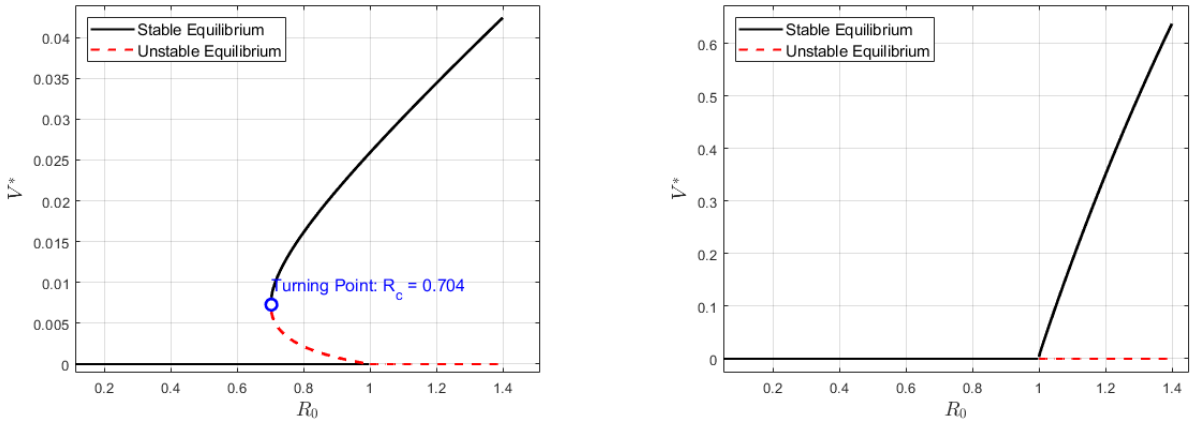

(a) $r = 105$, $S_T = 5425 \times 10^5$ (b) $r = 1.05$, $S_T = 5425 \times 10^5$

Figure 2.5: Bifurcation diagrams of System (2.2) with $\mathcal{R}_0$ as the bifurcation parameter. A large value of r induces a backward bifurcation, whereas a smaller r results in a forward bifurcation by eliminating bistability. In the Hogue *et al.* model [125] , $S_T = 5425 \times 10^5$. The other parameter values are the same as in Fig.2.4.

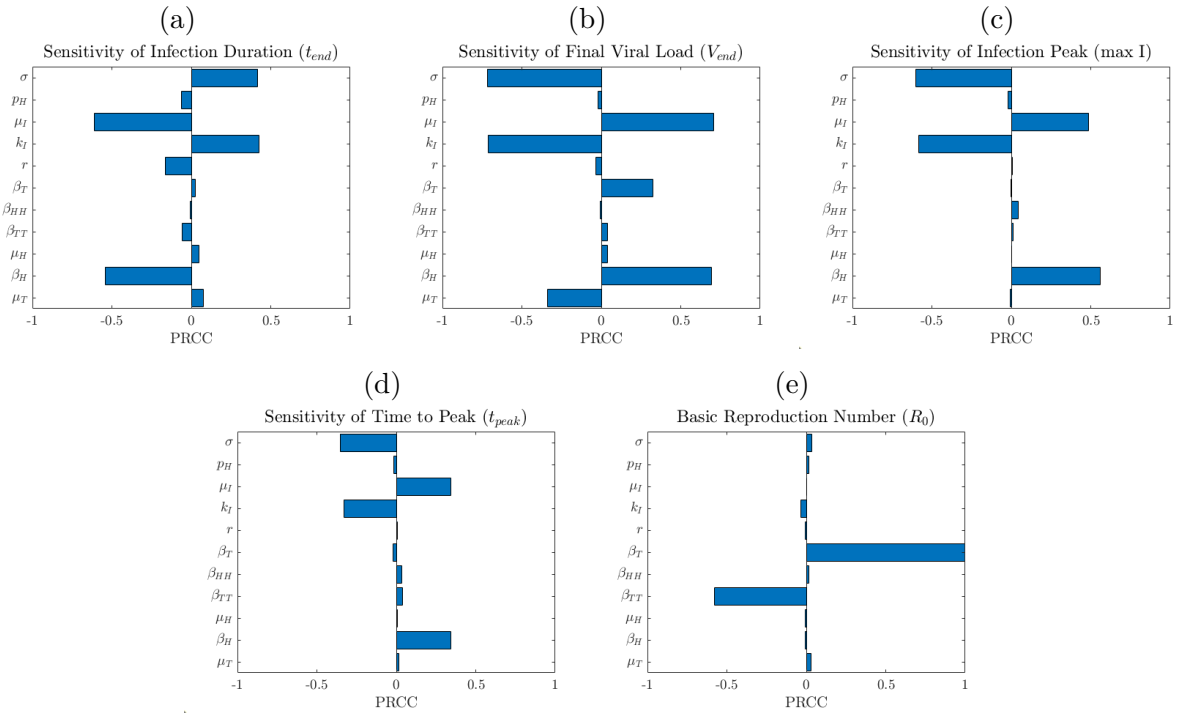

Figure 2.6: Sensitivities of (a) infection duration (t_{end}), (b) final viral load (V_{end}), (c) infection peak ($\max I$), (d) time to infection peak (t_{peak}), and (e) basic reproduction number ($\mathcal{R}_0$).

Our global sensitivity analysis was performed using **Partial Rank Correlation Coefficients (PRCCs)** derived from 2000 Latin Hypercube Sampling (LHS) simulations, derived using uniform distributions with mean shown in Table 2.1 and minimum and maximum values corresponding to 50% and 150% of the mean. LHS-PRCC quantifies how uncertainty in model parameters influences critical infection outcomes while accounting for nonlinear and monotonic dependencies. PRCC values range between -1 and $+1$: positive values indicate that an increase in a parameter leads to an increase in the corresponding outcome, while negative values indicate an inverse relationship. Parameters with PRCC magnitudes close to zero have negligible influence on the respective output.

Figure 2.6 illustrates the PRCCs computed for several biologically relevant infection measures: infection duration (t_{end}) (defined as the time to infection clearance), final viral load (V_{end}), infection peak ($\max I$), time to infection peak (t_{peak}), and the basic reproduction number ($\mathcal{R}_0$).

For the **infection duration** (t_{end}), the most influential parameter is the infected-cell death rate (μ_I), which shows a strong negative correlation. This indicates that an increase in μ_I, representing faster clearance of infected cells, shortens the infection period. Similarly, the helper-cell death rate (μ_H) and the infection rate between helper cells and virus (β_H) also show negative correlations, implying that greater cellular turnover reduces infection persistence. Conversely, the infection progression rate (σ) and helper-cell proliferation parameter (p_H) exhibit weak positive PRCCs, suggesting that higher viral replication efficiency or helper-cell activation slightly prolongs infection.

The **final viral load** (V_{end}) is primarily governed by the infection rate of target cells (β_T), which exhibits the strongest positive PRCC, confirming that increased viral infectivity leads to a higher equilibrium virus level. In contrast, the virus clearance rate (k_I) and infection progression rate (σ) are negatively correlated with V_{end}, suggesting that more efficient clearance or faster infection turnover reduces viral persistence. These results indicate

that V_{end} is most sensitive to parameters controlling viral infectivity and clearance efficiency.

The **infection peak** ($\max I$) depends on both infection and clearance dynamics. Positive PRCC values for β_H and β_T demonstrate that greater infection pressure on helper and target cells increases the maximum number of infected cells, while negative PRCCs for k_I and σ confirm that rapid virus clearance and infection progression suppress the peak. The infected-cell death rate (μ_I) again shows a dominant negative influence, indicating that infected-cell lifespan is a key determinant of how high infection can rise.

The **time to infection peak** (t_{peak}) shows a significant negative correlation with both k_I and σ. This means that faster clearance and infection progression accelerate the infection cycle, causing infection to peak earlier. Other parameters such as r and μ_T have negligible effects, indicating that infection kinetics rather than target availability dictate the timing of the peak.

Finally, the **basic reproduction number** ($\mathcal{R}_0$), defined as $\mathcal{R}_0 = \beta_T - \beta_{TT}$, displays the expected strong positive and negative correlations with β_T and β_{TT}, respectively. This reflects the analytical formulation of $\mathcal{R}_0$ and highlights that infection establishment and persistence depend primarily on the balance between viral transmission and loss rates.

Overall, the PRCC results demonstrate that the parameters most strongly influencing infection outcomes are the infected-cell death rate (μ_I), virus clearance rate (k_I), and infection rate of target cells (β_T). These findings align with biological intuition, confirming that the lifespan of infected cells and the efficiency of viral transmission and clearance are the dominant drivers of infection persistence and control within the host [137, 138, 139, 140, 141]. Consequently, therapeutic strategies that increase infected-cell death or enhance viral clearance could effectively reduce both infection duration and viral load.

In summary, the PRCC-based sensitivity analysis identifies the parameters governing infection dynamics at multiple timepoints from early infection kinetics to steady-state viral persistence offering quantitative guidance for intervention strategies and for prioritizing

parameters in further bifurcation and uncertainty analyses.

2.4 Conclusion

The combined bifurcation, basin of attraction, and sensitivity analyses of the proposed within-host HIV model provide a comprehensive understanding of the mechanisms governing viral persistence and clearance. The bifurcation analysis, supported by numerical simulations, reveals the existence of both forward and backward bifurcation structures, indicating that infection outcomes are not solely determined by the basic reproduction number $\mathcal{R}_0$. Specifically, the model admits multiple stable equilibria when $\mathcal{R}_0 < 1$, implying that infection can persist even when classical threshold conditions predict eradication. This bistable behavior highlights the importance of nonlinear infection dynamics, such as saturation in viral infection rates and the interplay between target-cell depletion and immune activation.

The basin of attraction analysis further supports these findings by illustrating that initial viral loads and immune cell levels critically determine which equilibrium state the system approaches. When the system operates near the bistable region, small perturbations in the initial conditions can shift trajectories from the disease-free equilibrium to a chronic infection state, emphasizing the difficulty of achieving complete viral clearance once infection is established. These results suggest that effective control strategies must not only reduce $\mathcal{R}_0$ below unity but also shift the system's state into the basin of the disease-free equilibrium through aggressive early treatment or immune stimulation.

The global sensitivity analysis based on Partial Rank Correlation Coefficients (PRCCs) identifies the key parameters driving the infection dynamics. The infected-cell death rate (μ_I), virus clearance rate (k_I), and target-cell infection rate (β_T) are the most influential parameters affecting infection duration, viral load, and infection persistence. In particular, an increase in μ_I or k_I substantially reduces infection severity, while higher β_T strongly enhances viral proliferation. These findings confirm that the lifespan of infected cells and

viral clearance efficiency are fundamental determinants of within-host HIV behavior.

Taken together, the model demonstrates that the interplay between bifurcation structure, parameter sensitivity, and initial condition dependence governs the transition between viral clearance and persistence. From a biological perspective, these results underscore that early therapeutic interventions targeting infected-cell clearance and viral replication can shift the system into the basin of the disease-free equilibrium, thereby preventing chronic infection. Mathematically, the coexistence of multiple equilibria and the strong parameter dependencies reinforce the nonlinear and threshold-sensitive nature of HIV infection dynamics within the host.

The model developed in this project advances the framework of Xie et al. [130] by explicitly incorporating the loss of virus adsorption driven by the terms $-\beta_{TT}TV$ and $-\beta_{HH}T_HV$ in the viral equation. In Xie's system, free virions are removed only by natural clearance $\mu_V V$, which means that new infections do not consume virus particles. This creates a mass imbalance at the moment of infection, whereas the modified system enforces strict conservation: each successful infection event removes one virion from circulation. This structural change generates clear mathematical consequences. First, although the leading coefficient $A = -\mu_I\beta_H^2(r+\beta_T)^2$ is not affected by adsorption, the parameters β_{TT} and β_{HH} contribute to the lower order coefficients B, C and F (both directly and through $\mathcal{R}_0 = \beta_T - \beta_{TT}$), altering the sign balance of the quartic equilibrium equation. This reduces the parameter region in which two positive endemic equilibria, and hence backward bifurcation—can exist. Second, the basic reproduction number in the modified model is $R_0 = \beta_T - \beta_{TT}$, which implies that virion adsorption through β_{TT} lowers the value of R_0. As β_{TT} increases, a higher value of β_T is required to push R_0 above 1, which means that infection requires stronger transmission to persist. The parameter β_{HH} does not enter R_0 explicitly, but contributes to the coefficients of the quartic endemic equilibrium polynomial and therefore influences R_c, the size of the bistable region and the possibility of backward bifurcation. Third, although the classification

of bifurcation remains identical backward if $a > 0$ and forward if $a < 0$, the modified model produces a more restrictive expression for a, containing additional negative terms from adsorption, and thus backward bifurcation arises only under more constrained and biologically plausible conditions.

Both models can display backward bifurcation, but the bifurcated region in the modified system is smaller and more mechanistically justified. No Hopf bifurcation was detected for biologically realistic parameter values, indicating that the dynamical class remains consistent with Xie et al.[130], but with more conservative threshold geometry. From a therapeutic point of view, reducing β_{TT} or β_{HH} by inhibiting entry directly decreases the probability of viral establishment, linking intervention strategies with model outcomes in a transparent way. Overall, the contribution of this thesis is not to replace the Xie model but to refine it: to maintain its mathematical structure while correcting the viral mass balance and strengthening the biological interpretation of threshold behavior. This refinement provides a clearer theoretical basis for analyzing treatment strategies and understanding the conditions under which HIV persistence or clearance occurs.

Chapter 3

Measles and Waning Immunity

This chapter is submitted with a larger publication on measles.

3.1 Introduction

Measles, caused by the measles virus (MeV), is a very contagious childhood disease [25]. Despite the existence of a highly effective vaccine [142], measles cases continue to persist worldwide, causing significant morbidity and mortality [142]. The World Health Organization (WHO) [143] recommends that every child receive two doses of the measles vaccine. Seroconversion following a single dose of vaccine is estimated to be 95% [144]. Vaccine effectiveness has been approximated to be 93-96.7%, and 97-99.7%, after one and two doses [145, 146].

In 2024-2025, measles cases have been reported across Canada [147], a country with relatively high vaccination coverage [148]. While measles infections have been mainly reported in the unvaccinated, individuals with one or two doses have also contracted the disease [147]. Measles cases in vaccinated individuals have been reported previously [149, 150, 151]. A recent study by Bolotin et al. [152] showed that antibody immunity can decay over time in vaccinated individuals, whereby some susceptibility could be reached approximately 51 years after full immunization.

Assuming lifelong immunity from vaccination, mathematical models have shown that herd immunity can be achieved in populations that maintain vaccine uptake greater than $p_c = 1 - 1/\mathcal{R}_0$, where $\mathcal{R}_0$ is the basic reproduction number and quantifies the infection transmission potential of a disease [153, 16]. Historically, the basic reproduction number for measles has been reported to fall between 12 to 18 [25], though a recent study has identified a much larger range, with median values for different geographic regions lying between 11-16 [154]. Given these values, it is has been widely accepted that a critical vaccination threshold of at least 95% should be the goal to achieve herd immunity across the globe [143].

If measles immunity gained from vaccination wanes, calculations of the critical vaccination threshold p_c must be revisited. Herewithin, we develop and utilize a mathematical model to determine this critical threshold and investigate its dependence on the waning rate of immunity. Further, we investigate the effects of the waning rate on other important calculations related to measles: the probability of an outbreak, and the final size of such an outbreak. Finally, we apply our mathematical model to a measles outbreak in Southwestern Ontario, Canada. The mathematical models employed here are extensions of the well-known Susceptible-Infected-Recovered (SIR) model to include vaccination and the waning and boosting of vaccine-conferred immunity.

3.2 Model Formulation

In this model, the total population N is divided into seven classes: susceptible individuals (S) (those at risk of infection), primary infectives (I) (individuals fully susceptible at the time of exposure), secondary infectives (I_w) (individuals infected while their immunity is waning), vaccinated individuals (V), individuals with waning immunity (W), primary recovered (R) (individuals who gain lifelong immunity after infection), and secondary recovered (R_w) (who also receive permanent immunity after infection). The model is defined by the following

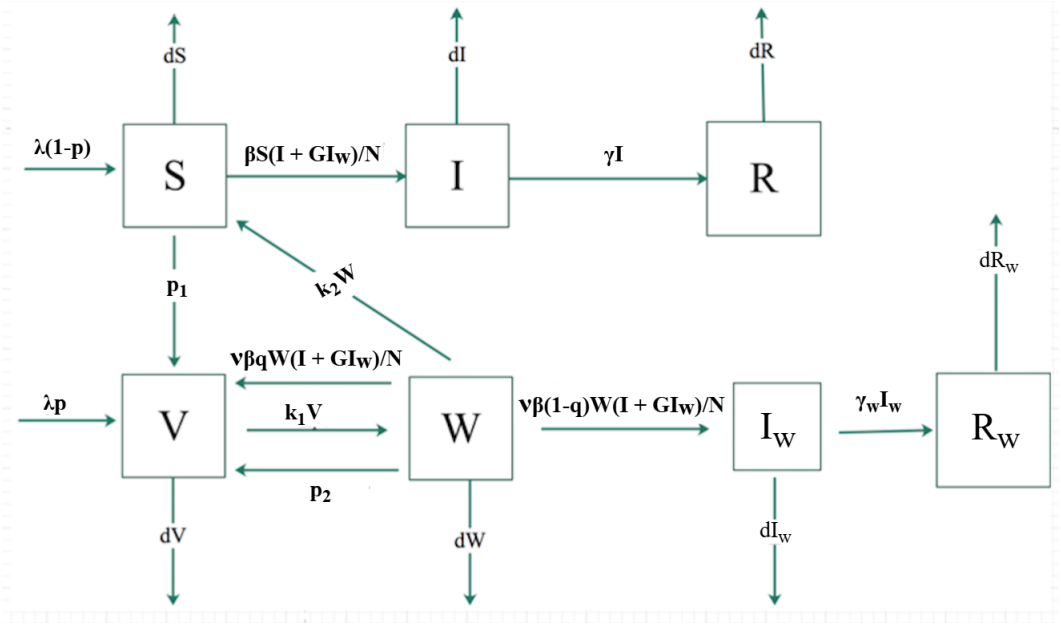

Figure 3.1: Model flow diagram

system of ordinary differential equations:

$$
\begin{aligned}
S' =& \lambda(1-p) - \beta S(I + GI_w) + k_2 W - p_1 S - dS \\
I' =& \beta S(I + GI_w) - \gamma I - dI \\
I'_w =& \nu(1-q)\beta(I + GI_w)W - \gamma_w I_w - dI_w \\
R' =& \gamma I - dR \\
R'_w =& \gamma_w I_w - dR_w \\
V' =& \lambda p - k_1 V + q\nu\beta(I + GI_w)W + p_1 S + p_2 W - dV \\
W' =& k_1 V - \nu\beta(I + GI_w)W - k_2 W - p_2 W - dW
\end{aligned}
\tag{3.1}
$$

Figure 3.1 illustrates the flow diagram of these interactions and dynamics. Table 3.1 lists the model parameters and their corresponding values.

We consider a closed population of size N, where individuals enter the system at twelve months of age - the usual time for receiving the first measles vaccination. At entry, a fraction

Parameter	Definition	Values
d	Natural death rate (year^{-1})	1/82 [155]
p	Fraction of newborns effective vaccination (obtained vaccine and gained a level of neutralizing Immunity)	$[0.75, 1]$
λ	Birth Rate (people x year^{-1})	dN
$\mathcal{R}_0$	Basic Reproduction Number	$[5, 22]$
β	Infection rate (year^{-1})	$[130, 572]$ obtained using $\mathcal{R}_0$
γ	Recovery rate (year$^-1$)	26
γ_w	Recovery rate from I_w (year^{-1})	$(1, 2, 3, 4, 5) * \gamma$
ν	Boosting proportionality constant	$[0, 1]$
G	Infectiousness that I_w can have compared to I	$[0, 1]$
q	Fraction of those boosted that move to V	$[0, 1]$
k_1	Waning rate from V to W (year^{-1})	$[0, 1]$
k_2	Waning rate from W to S (year^{-1})	$[0, 1]$
p_1	Vaccination rate between S and V	$[0, 1/10]$
p_2	Vaccination rate between W and V	$[0, 1/10]$

Table 3.1: Table of Parameters

p of new individuals is vaccinated at rate λ and moves into the V class, while the remaining proportion $(1-p)$ joins the susceptible class S. Unvaccinated individuals in S receive a second vaccine dose at rate p_1, transferring them to the V compartment. Susceptible individuals who remain unvaccinated can become infected after contact with infectious persons at rate β after which they move to compartment I where they are fully infectious.

We assume that vaccinated individuals can experience waning immunity, moving them from V to W with rate k_1, and then from W to S with rate k_2. We also assume that individuals in W can experience infection (with probability $1 - q$) or a boost in immunity (with probability q) upon contact with an infectious person. However, we assume that W individuals are less susceptible than their S counterparts and thus the transmission rate β is reduced by $0 \leq \nu \leq 1$ for W individuals compared to their susceptible S counterparts. If a W becomes infected, they move to compartment I_w where they stay for $1/\gamma_w$ time, on average. We also assume that I_w individuals can be infectious, with a reduced infectiousness

$0 \leq G \leq 1$ compared to their I counterparts. When $G = 1$, secondary infections I_w are as infectious as primary ones I, whereas $G = 0$ indicates that I_w individuals are non-infectious.

The population is assumed to mix homogeneously, and transmission follows frequency-dependent contact, expressed as $\beta\frac{(I+I_w)}{N}$. Individuals in the I compartment remain infectious for an average of $1/\gamma$ time units before recovering and moving to R; similarly, individuals in I_w recover to R_w. Both recovered groups acquire lifelong immunity.

At the time of a measles outbreak, S and W individuals may elect to be vaccinated. These occur with rates p_1 and p_2, respectively. For simplicity, we assume that these values are very close to zero; however, we include these in the model for analysis.

Finally, as we follow the population over time outside and inside measles outbreak, we include demographics in our model – birth λ and natural mortality dS, dI, dI_w, dR, dR_w, dW and dV. However, when we are studying a short time-span i.e., a measles outbreak, we ignore these parameters.

3.3 Results

3.3.1 Disease free Equilibrium:

The disease free equilibrium (DFE) is $E_0 = (S_0, I_0, I_{w0}, R_0, R_{w0}, V_0, W_0)$
$= (S_0, 0, 0, 0, 0, V_0, W_0)$ where

$$\begin{aligned} S_0 =& N\frac{(1-p)(d^2+(k_1+k_2+p_2)d+k_1k_2)+pk_1k_2}{d^2+(k_1+k_2+p_1+p_2)d+(k1+k_2+p_2)p_1+k_1k_2} \\ V_0 =& N\frac{(dp+p_1)(d+k_2+p_2)}{d^2+(k_1+k_2+p_1+p_2)d+(k_1+k_2+p_2)p_1+k_1k_2} \\ W_0 =& N\frac{k1(dp+p_1)}{d^2+(k_1+k_2+p_1+p_2)d+(k1+k_2+p_2)p_1+k_1k_2} \end{aligned} \tag{3.2}$$

3.3.2 The Basic and Control Reproduction Numbers

The basic reproduction number and the control reproduction number of the system are derived from the Next Generation Matrix approach [24, 104].

The basic reproduction number is given by:

$$\mathcal{R}_0 = \frac{\beta N}{(\gamma + d)}$$

Thus, $\mathcal{R}_0$ measures the expected number of secondary infections generated by a single infected individual in a fully susceptible population.

In contrast, the number of control reproduction $\mathcal{R}_c$ accounts for the presence of vaccination and the waning immunity. So, the control reproduction number is

$$\mathcal{R}_c = \frac{\mathcal{R}_0}{N}\left[S_0 + W_0 G\nu(1-q)\frac{d+\gamma}{d+\gamma_w}\right] \tag{3.3}$$

where S_0 and W_0 are given by the eqn 3.2. We note that when $p_1, p_2 = 0$, which is typically the case when measles infections are not occurring in the population, $\mathcal{R}_c$ becomes

$$\mathcal{R}_c = \mathcal{R}_0\left[(1-p) + p\frac{k_1 k_2}{(d+k_1)(d+k_2)} + Gp\frac{(1-q)\nu k_1 d(d+\gamma)}{(d+k_1)(d+k_2)(d+\gamma_w)}\right]. \tag{3.4}$$

Here, the first two terms represent infections originating from individuals in the susceptible class, while the third term accounts for infections arising from individuals in the waning immunity class (W). This is particularly relevant for different values of G, since $0 \leq G \leq 1$, if G = 0, secondary infections (I_w) do not appear; if G = 1, secondary infections (I_w) transmit at the same rate as primary infections (I); when $0 < G < 1$, secondary infections (I_w) occur and transmit, but at a lower rate than I.

Note that when $p_1, p_2 = 0$ and when the waning rates k_1, k_2 approach zero, meaning that immunity is almost permanent, the control reproduction number is approximately $\mathcal{R}_c \approx (1-p)\mathcal{R}_0$. In contrast, if immunity is short-lived and wanes rapidly, the system behaves

as if there is no lasting immunity, leading to $\mathcal{R}_c \approx \mathcal{R}_0$.

3.3.3 The Critical Vaccination Threshold

To determine the minimum vaccination coverage required to achieve herd immunity, we use the expression for $\mathcal{R}_c$. Setting $\mathcal{R}_c = 1$ and substituting $p = p_c$, we solve for p_c, which represents the critical vaccination threshold necessary to suppress sustained disease transmission. We obtain

$$\begin{aligned} p_c = \left(1 - \frac{1}{\mathcal{R}_0}\right) \frac{(d(d + k_1 + k_2 + p_2) + k_1 k_2)(d + \gamma_w)}{d((d + k_1 + k_2 + p_2)(d + \gamma_w) - G k_1 \nu (1 - q)(d + \gamma))} \\ - p_1 \frac{((d + k_1 + k_2 + p_2)(d + \gamma_w) - G k_1 \nu (1 - q)(d + \gamma)\mathcal{R}_0)}{\mathcal{R}_0 d((d + k_1 + k_2 + p_2)(d + \gamma_w) - G k_1 \nu (1 - q)(d + \gamma))} \end{aligned} \tag{3.5}$$

and when $p_1, p_2 = 0$ we have,

$$p_c = \left(1 - \frac{1}{\mathcal{R}_0}\right) \frac{(d + k_1)(d + k_2)(d + \gamma_w)}{d((d + k_1 + k_2)(d + \gamma_w) - G k_1 \nu (1 - q)(d + \gamma))}\,. \tag{3.6}$$

Note that Eq. (3.6) is lowest when $G k_1 \nu (1 - q)$ is zero, which occurs when individuals with waning immunity are not susceptible ($\nu = 0$), when I_w are not infectious ($G = 0$), when W individuals only experience boosts to V upon encounters with infectious individuals ($q = 1$) and when vaccine-induced immunity is lifelong ($k_1 = 0$).

For herd immunity to be achievable ($p_c < 1$), a specific mathematical condition must hold. This ensures that vaccination alone can reduce measles transmission below the level required for sustained outbreaks. If this condition is not met, it would indicate that even with full vaccination efforts, measles could still circulate in the population. So, the following conditions should be satisfied for $p_c < 1$, as derived from (3.5).

$$\mathcal{R}_0 < \frac{(d^2 + (k_1 + k_2 + p_1 + p_2)d + (k_2 + p_1)k_1 + (p_2 + k_2)p_1)\,(d + \gamma_w)}{k_1 k_2 (d + \gamma_w) + G k_1 \nu (1 - q)(p_1 + d)(d + \gamma)}\,. \tag{3.7}$$

Also, the denominator should not be zero and always positive to satisfy the condition. So,

$$k_1k_2(d+\gamma_w) + Gk_1\nu(1-q)(p_1+d)(d+\gamma) > 0\,.$$

Figure 3.2 illustrates the contour plots of the vaccination threshold (p_c) in ($\mathcal{R}_0$, k_1, k_2) parameter space (see Table 3.1 for parameter values). The color bar represents the critical vaccination coverage required to maintain herd immunity under different combinations of waning rates. As expected, p_c increases monotonically with $\mathcal{R}_0$: higher transmission potential demands higher vaccine coverage to prevent outbreaks. The effect of the waning parameters k_1 (loss of vaccine-induced immunity) and k_2 (loss of partial immunity) is also evident. When both k_1 and k_2 are small, immunity is long-lasting and the required vaccination threshold remains low. However, as either waning rate increases, more individuals return to the susceptible class, thereby elevating p_c. This effect is most pronounced for large $\mathcal{R}_0$ values, where even moderate waning can significantly raise the critical coverage needed for disease control. At extremely high k_1 or k_2 values, the surfaces begin to plateau, indicating that beyond a certain level of immunity loss, further increases in waning have little additional impact because herd immunity is already unsustainable. Overall, the figure emphasizes that the interplay between transmission intensity and immunity waning strongly determines the vaccination effort required to achieve and sustain measles elimination.

3.3.4 Type Reproduction Numbers

Infected individuals in I and I_w can transmit infection to susceptibles in S and individuals with waning immunity in W. We are interested in quantifying the type reproduction numbers $R_{0,A\to B}$, $B \in I, I_w$, defined as the expected number of new infections of type $B \in I, I_w$ caused by a single infectious individual of type $A \in I, I_w$ in an otherwise susceptible population. These expressions are derived under the assumption that the epidemic is in its initial phase, so that S_0 and W_0 are constant (at the DFE) and the system dynamics can be approximated by

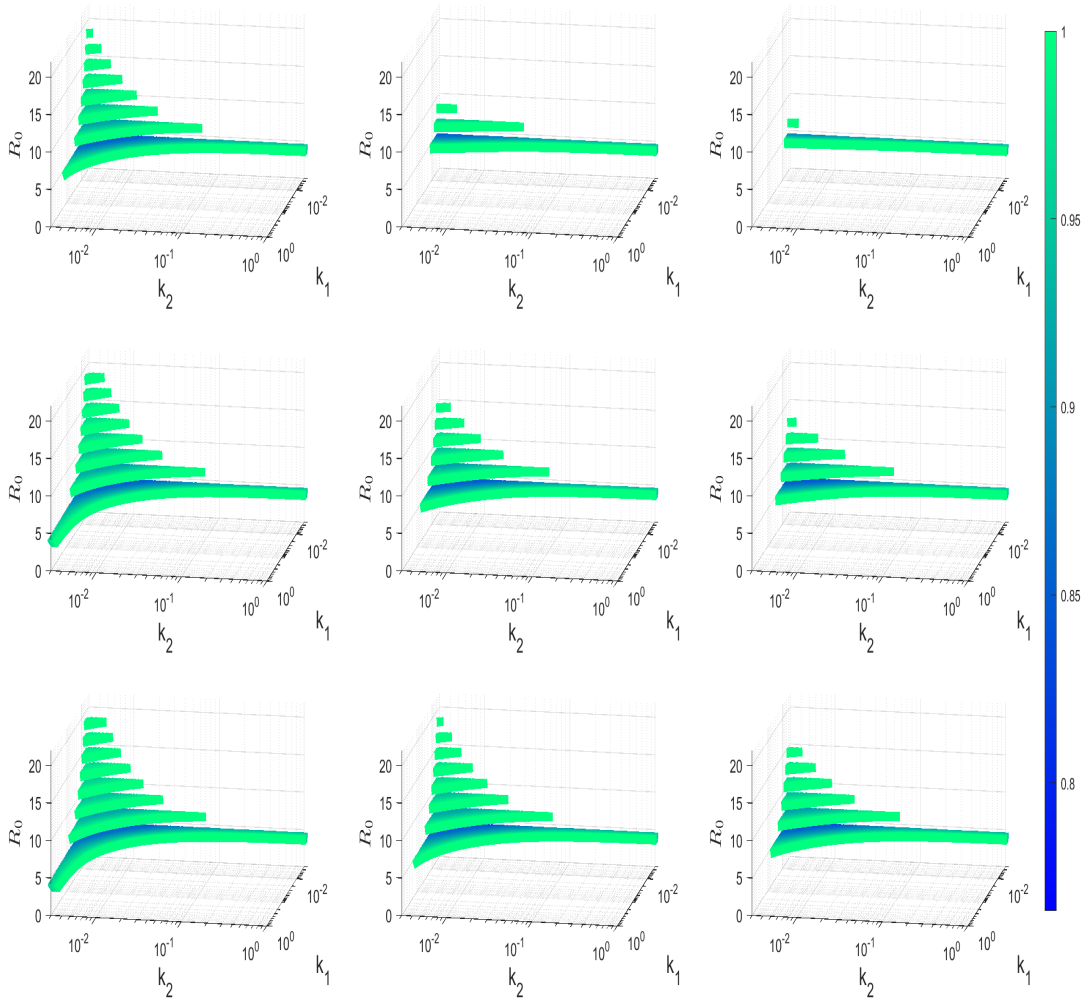

Figure 3.2: Critical vaccination threshold p_c (colourbar) for different values of $\mathcal{R}_0$, k_1, and k_2, when $\gamma_w = [\gamma, 3\gamma, 5\gamma]$ **(top to bottom row)**, $d = 1/82$ years^{-1}, $G\nu(1-q) = (0.1, 0.5, 0.8)$ **(left to right panels)**. k_1 and k_2 are shown in log scale.

Type Reproduction Number	Duration of Infection	Infectiousness	Susceptible Population Magnitude	Susceptibility	Probability of Becoming and Infected
$\mathcal{R}_{0,I\to I}$	$1/\gamma$	β	S_0	1	1
$\mathcal{R}_{0,I\to I_w}$	$1/\gamma$	β	W_0	ν	$1-q$
$\mathcal{R}_{0,I_w\to I}$	$1/\gamma_w$	βG	S_0	1	1
$\mathcal{R}_{0,I_w\to I_w}$	$1/\gamma_w$	βG	W_0	ν	$1-q$

Table 3.2: Type Reproduction Numbers: Derivation

a branching process. The terms incorporate heterogeneity in susceptibility and infectiousness: waned individuals W are less susceptible (scaled by $\nu(1-q)$, and infected individuals with waned immunity I_w may transmit at a reduced rate (scaled by G). The reproduction numbers are given by:

$$\begin{aligned}
\mathcal{R}_{0,I\to I} &= \frac{\beta S_0}{\gamma} \\
\mathcal{R}_{0,I\to I_w} &= \frac{\beta\nu(1-q)W_0}{\gamma} \\
\mathcal{R}_{0,I_w\to I} &= \frac{\beta G S_0}{\gamma_w} \\
\mathcal{R}_{0,I_w\to I_w} &= \frac{\beta G\nu(1-q)W_0}{\gamma_w}
\end{aligned}$$

We note that each type reproduction number is given by the product of (1) the duration of infection of the infected individual $(1/\gamma, 1/\gamma_w)$, (2) the infectiousness of the infected individual $(\beta, G\beta)$, (3) the magnitude of the susceptible populations at the DFE (S_0, W_0), (4) the susceptibility of the susceptibles $(1, \nu)$, (5) and the probability that the newly exposed contact becomes and infected $(1, (1-q))$. The components of all type reproduction numbers are given in Table 3.2.

3.3.5 Final Size Relation

We are interested in knowing how many infections we should expect in a given measles outbreak. This can be calculated using the final size relation. We now derive the final size relation using the Arino method in [156].

Consider the following submodel of Model (3.2) without demographics ($\lambda, d = 0$)

$$\begin{aligned}
\frac{dS}{dt} &= -\beta S(I + GI_w) + k_2 W - p_1 S \\
\frac{dW}{dt} &= -\nu\beta W(I + GI_w) + k_1 V - k_2 W - p_2 W \\
\frac{dI}{dt} &= \beta S(I + GI_w) - (\gamma + d)I \\
\frac{dI_w}{dt} &= \nu(1 - q)\beta W(I + GI_w) - (\gamma_w + d)I_w
\end{aligned}$$

The infected classes are I and I_w, originating from S and W respectively. Let $I_0 = I(0)$ and $I_{w,0} = I_w(0)$ be the initial number of infecteds.

Let the vector of infectious classes be:

$$y(t) = \begin{bmatrix} I(t) \\ I_w(t) \end{bmatrix}$$

and the vector of susceptible classes be:

$$x(t) = \begin{bmatrix} S(t) \\ W(t) \end{bmatrix}$$

We have the initial conditions

$$S(0) = S_0, \quad W(0) = W_0, \quad I(0) = I_0, \quad I_w(0) = I_{w0}.$$

Let $S_\infty = \lim_{t\to\infty} S(t)$ and $W_\infty = \lim_{t\to\infty} W(t)$ be the size of the S and W populations

at the end of the measles outbreak. Also, at the end of the outbreak, we define $I_\infty = \lim_{t\to\infty} I(t) = 0$ and $I_{w,\infty} = \lim_{t\to\infty} I_w(t) = 0$.

In the Arino framework [156], the model is cast as:

$$\boldsymbol{x}' = \Pi D y \cdot \beta \cdot \boldsymbol{b} x - V x \tag{3.8}$$

$$\boldsymbol{y}' = -D y \cdot \beta \cdot \boldsymbol{b} x \tag{3.9}$$

where x is a vector of susceptible populations and y is a vector of infected populations. Here, $x = [S, W]'$ and $y = [I, I_w]'$. Following the Arino framework, we also have

$$D = \begin{bmatrix} 1 & 0 \\ 0 & \nu \end{bmatrix} \tag{3.10}$$

$$b = \begin{bmatrix} 1 & G \end{bmatrix} \tag{3.11}$$

$$\Pi = \begin{bmatrix} 1 & 0 \\ 0 & 1-q \end{bmatrix} \tag{3.12}$$

$$V = \begin{bmatrix} \gamma + d & 0 \\ 0 & \gamma_w + d \end{bmatrix} \tag{3.13}$$

where D is a matrix of susceptibility weights, b is an infectivity vector of I and I_w, Π is a matrix of the contributions to the infected classes upon infection of each susceptible class, and V is a matrix of the rates at which infecteds leave the infected classes. We compute the average length of time that an individual is infected in each class as

$$V^{-1} = \begin{bmatrix} \frac{1}{\gamma+d} & 0 \\ 0 & \frac{1}{\gamma_w+d} \end{bmatrix} \tag{3.14}$$

Let

$$\Gamma = \beta b V^{-1} \Pi D = \beta \left[\tfrac{1}{\gamma+d}, \tfrac{G\nu(1-q)}{\gamma_w+d} \right] = \left[\Gamma_1, \Gamma_2 \right]$$

then, as per the Arino framework, the final size equations for our model are

$$\ln\left(\frac{S_0}{S_\infty}\right) = \Gamma_1(S_0 - S_\infty) + \Gamma_2(W_0 - W_\infty) + \Gamma_1 I_0 + \Gamma_2 I_{w0} \tag{3.15}$$

$$\ln\left(\frac{W_0}{W_\infty}\right) = \nu\left[\Gamma_1(S_0 - S_\infty) + \Gamma_2(W_0 - W_\infty)\right] + \Gamma_1 I_0 + \Gamma_2 I_{w0} \tag{3.16}$$

where Eq. (3.15) corresponds to the unvaccinated class, Eq. (3.16) includes the vaccine-modified susceptibility via $(1-q)$, and $\Gamma_1 = \dfrac{\beta}{\gamma + d}$, $\Gamma_2 = \dfrac{\beta G \nu (1-q)}{\gamma_w + d}$.

Subtracting both equations gives:

$$\ln\left(\frac{S_o}{S_\infty}\right) - \frac{1}{\nu}\ln\left(\frac{W_0}{W_\infty}\right) = 0 \quad \Rightarrow \quad \frac{S_0}{S_\infty} = \left(\frac{W_0}{W_\infty}\right)^{\frac{1}{\nu}}$$

This yields

$$\frac{W_\infty}{W_0} = \left(\frac{S_\infty}{S_0}\right)^{\nu}$$

Therefore, the final size of an epidemic is determined by solving the nonlinear system

$$\begin{aligned} \ln\left(\frac{S_0}{S_\infty}\right) &= \Gamma_1(S_0 - S_\infty) + \Gamma_2\left(W_0 - W_\infty\right) + \Gamma_1 I_0 + \Gamma_2 I_{w0} \\ W_\infty &= W_0\left(\frac{S_\infty}{S_0}\right)^{\nu}. \end{aligned}$$

Finally, we have,

$$\begin{aligned} \ln\left(\frac{S_0}{S_\infty}\right) &= \frac{\beta}{\gamma + d}(S_0 - S_\infty) + \frac{\beta G \nu (1-q)}{\gamma_w + d}\left(W_0 - W_\infty\right) + \frac{\beta}{\gamma + d} I_0 + \frac{\beta G \nu (1-q)}{\gamma_w + d} I_w 0 \\ W_\infty &= W_0\left(\frac{S_\infty}{S_0}\right)^{\nu}, \end{aligned}$$

and thus, given parameters $\beta, G, \gamma, \gamma_w, d, p, q$, and initial total population N_0 (which is defined by the DFE, including S_0 and W_0), these equations can be solved numerically to find S_∞ and W_∞.

3.3.6 Probability of No Outbreak

Model (3.2) is deterministic. However, the world is stochastic in that there is always a probability of no disease transmission from an infected to the susceptible S or waning immunity W populations. Thus, at the beginning of an outbreak there is a probability that an index infected does not transmit the infection. We now determine the probability of no outbreak under this assumption.

To derive the expression for the probability of no new infections upon the introduction of a single infected individual into the vaccinated population, we use a **branching process approximation**. This approximation is valid when the number of infected individuals is small, and the rest of the population (especially susceptible and vaccinated individuals) remains approximately constant during the early phase of the outbreak. Here, we will assume that there is only one initial infected and that this initial infected is introduced into a population at the DFE. To derive the probability of no outbreak, we follow the steps outlined below.

Step 1: Identify the Initial Infection Pathways

There are two possible initial conditions:

- A single standard infected individual is introduced: $\Pr(I_0 = 1)$
- A single waned-immunity infected individual is introduced: $\Pr(I_{w,0} = 1)$

Step 2: Use the Branching Process Approximation

In the early stage of the outbreak, the initial infected individual either recovers before causing any secondary infections or transmits to others. We compute the probability of no secondary transmission for each case.

Case 1: Initial Infected is Standard ($I_0 = 1$)

Consider the equation

$$\frac{dI}{dt} = \beta S(I + GI_w) - \gamma I \, .$$

We thus have a total infection rate of:

$$\beta S_0 + \beta\nu(1-q)W_0$$

where βS_0 is the infections caused in susceptibles and $\beta\nu(1-q)W_0$ is the infections caused in waned individuals.

The probabilility that an infected individual I recovers before it can infect anyone is

$$\frac{\gamma}{\gamma + \beta S_0 + \beta\nu(1-q)W_0} = \frac{1}{1 + \beta S_0/\gamma + \beta\nu(1-q)W_0/\gamma}$$

Given the type reproduction numbers

$$R_{0,I\to I} = \frac{\beta S_0}{\gamma}, \quad R_{0,I\to I_w} = \frac{\beta\nu(1-q)W_0}{\gamma}$$

we have

$$\Pr(I(t) = 0, I_w(t) = 0 \mid I_0 = 1) = \frac{1}{1 + R_{0,I\to I} + R_{0,I\to I_w}}$$

which is the probability that there are no new infections produced by an initial infected in the I class when it is introduced into a population at the DFE.

Case 2: Initial Infected is Waned ($I_{w,0} = 1$)

Consider the equation

$$\frac{dI_w}{dt} = \nu(1-q)\beta(I + GI_w)W - \gamma_w I_w \, .$$

Thus, for a single I_w individual, the infection rate is

$$\beta G S_0 + \beta G \nu (1-q) W_0 \,.$$

Given the recovery rate γ_w, the probability of no new infections is

$$\frac{\gamma_w}{\gamma_w + \beta G S_0 + \beta G \nu (1-q) W_0} = \frac{1}{1 + \beta G S_0/\gamma_w + \beta G \nu (1-q) W_0/\gamma_w} \,.$$

Again, given the type reproduction numbers

$$R_{0,I_w \to I} = \frac{\beta G S_0}{\gamma_w}, \quad R_{0,I_w \to I_w} = \frac{\beta G \nu (1-q) W_0}{\gamma_w}$$

we have

$$\Pr(I(t) = 0, I_w(t) = 0 \mid I_{w,0} = 1) = \frac{1}{1 + R_{0,I_w \to I} + R_{0,I_w \to I_w}}$$

which is the probability that there are no new infected made by an initial I_w infected when it is introduced into a population at the DFE.

Step 3: Combine the Two Probabilities

Assuming mutually exclusive initial conditions we have the probability that there are no new infecteds given the introduction of an I or I_w infected with probabilities $\Pr(I_0 = 1)$ and $\Pr(I_{w,0} = 1)$. This is given by

$$\begin{aligned} \Pr(I(t) = 0, I_w(t) = 0) = \; & \Pr(I_0 = 1) \cdot \frac{1}{1 + R_{0,I \to I} + R_{0,I \to I_w}} \\ & + \Pr(I_{w,0} = 1) \cdot \frac{1}{1 + R_{0,I_w \to I} + R_{0,I_w \to I_w}} \end{aligned}$$

The above analysis provides the probability of no outbreak given the probability that an initial infected does not transmit infection. We are interested in understanding the

probability of different sized outbreaks from our model. In the following, we employ our model to look at the probability of no outbreak (no new infections) and outbreaks that consist of 50 or more new infection. Stochastic simulations of Model 3.2 are conducted using a Monte Carlo Markov Chain approach (or Gillespie simulation) [157]. To assess the impact of importation, a single infectious individual—either I or I_w with equal probability is introduced into a large population of 100,000 individuals initially at the disease-free equilibrium, defined by p, p_1, p_2, d, k_1, and k_2. The numbers of I and I_w individuals are then tracked over a 90-day period. A total of 1000 independent simulations are performed for each parameter combination of $\mathcal{R}_0, k_1, k_2, p, p_1, p_2, \nu, (1-q)$, and G.

In summary, in this section, we investigate the probability of a measles outbreak under different parameter settings of $\mathcal{R}_0, k_1$, and k_2, considering various levels of vaccine uptake (p), rates of transition from the W class to the I_w class upon exposure $(\nu(1-q))$, and the relative infectivity of I_w individuals (G). We also consider p_1 and p_2, representing vaccination of S and W individuals during an outbreak.

Figures 3.3-3.13 plot the probability that no new infections are produced by an initially imported infected individual (dots) when $\mathcal{R}_0 = 8, 12,$ or $16, p = 0.8, 0.9, 0.93,$ or $0.95, p_1, p_2 =$ 0 or $1/10, G = [0, 1], \gamma_w = [\gamma, 3\gamma, 5\gamma]$ $[year^{-1}]$. Other parameter values are $\nu = 1, (1-q) = [0, 0.2, 0.5, 0.8, 1]$, and k_1 and $k_2 = [1/300$(denoted by L)$, 1/100, 1/50, 1/25, 1/10]year^{-1}$. The probabilities of outbreaks resulting in more than 50 new infections (combined $I + I_w$ cases) are also shown (stars). Figures 3.3-3.13 show that the probability of no new infections (dots) can range from 4% to 85%, depending on the values of $G, \mathcal{R}_0, p, p_1, p_2, \gamma_w, (1-q), k_1$, and k_2. We note that these probabilities are in close agreement with our analytical calculation above. The probability of more than 50 new infections also varies with these parameters, ranging from 5% to 96%. Higher vaccination coverage (p) and greater vaccination participation (p_1, p_2) increase the probability of no new infections, whereas larger $\mathcal{R}_0$, faster waning (k_1, k_2), and higher infectivity $(G = 1)$ increase the likelihood of outbreaks.

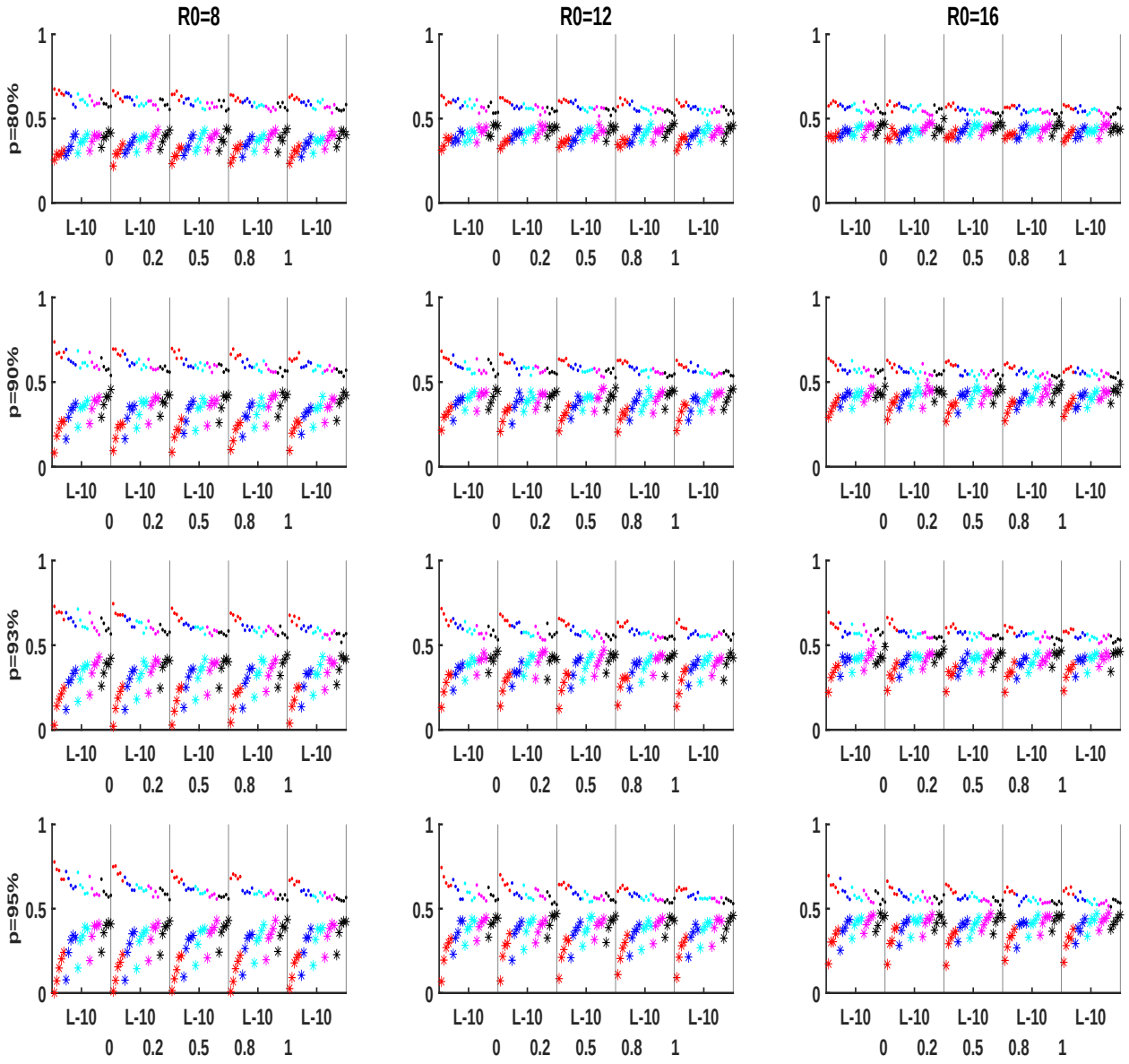

Figure 3.3: Probability of zero (dots) or > 50 (stars) new infections $(I + I_w)$ when $\mathcal{R}_0 = 8, 12, \text{or } 16$, $p = 0.80, 0.90, 0.93, \text{or } 0.95$, $\boldsymbol{\gamma_w} = \boldsymbol{\gamma}$ **years**$^{-1}$, $\boldsymbol{G} = \mathbf{0}$, $\nu = 1$, $(1-q) = [0, 0.2, 0.5, 0.8, 1]$ and $p_1 = p_2 = 0$. The symbols within each colour correspond to the probabilities as k_2 increases. The colour change as k_1 increases. $(1-q)$ increases for each subplot within each panel.

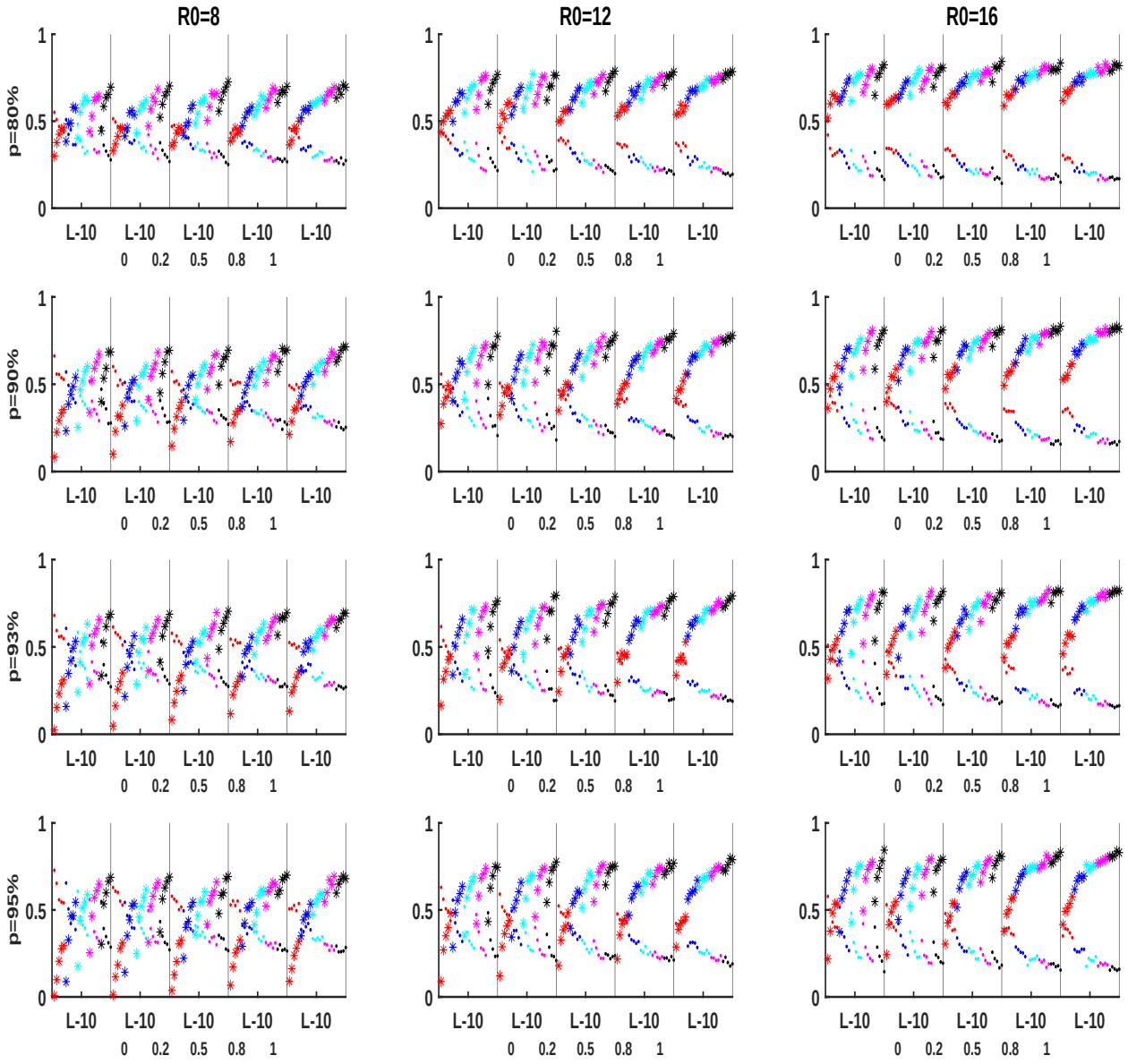

Figure 3.4: Probability of zero (dots) or > 50 (stars) new infections ($I + I_w$) when $\mathcal{R}_0 = 8, 12,$ or 16, $p = 0.80, 0.90, 0.93,$ or 0.95, $\boldsymbol{\gamma_w = 5\gamma}$ **years**$^{-1}$, $\boldsymbol{G = 1}$, $\nu = 1$, $(1-q) = [0, 0.2, 0.5, 0.8, 1]$ and $p_1 = p_2 = 0$. The symbols within each colour correspond to the probabilities as k_2 increases. The colour changes as k_1 increases. $(1-q)$ increases for each subplot within each panel.

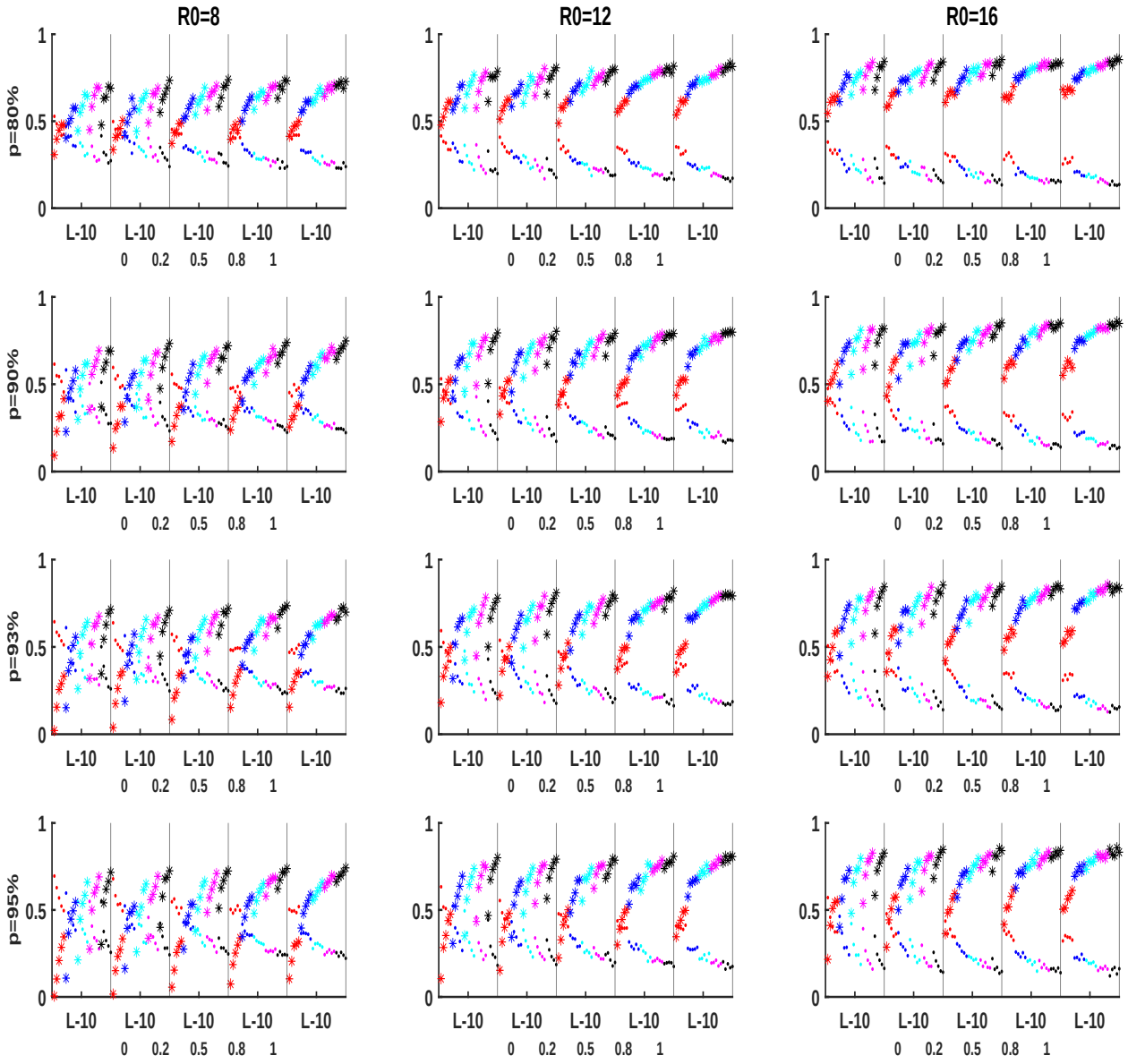

Figure 3.5: Probability of zero (dots) or > 50 (stars) new infections ($I + I_w$) when $\mathcal{R}_0 = 8, 12, \text{or } 16$, $p = 0.80, 0.90, 0.93, \text{or } 0.95$, $\boldsymbol{\gamma_w = 4\gamma}$ **years**$^{-1}$, $\boldsymbol{G = 1}$, $\nu = 1$, $(1-q) = [0, 0.2, 0.5, 0.8, 1]$ and $p_1 = p_2 = 0$. The symbols within each colour correspond to the probabilities as k_2 increases. The colour changes as k_1 increases. $(1-q)$ increases for each subplot within each panel.

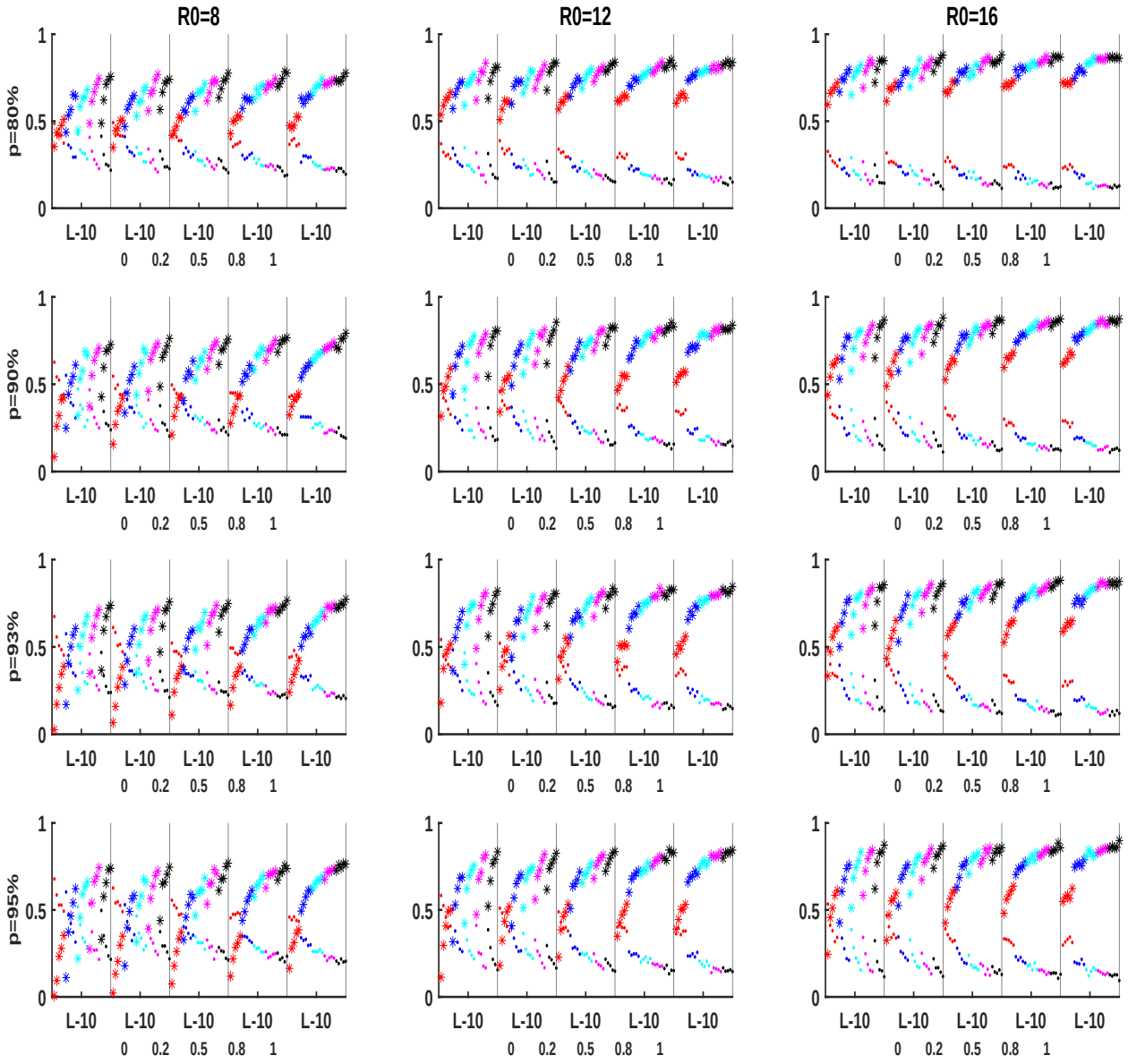

Figure 3.6: Probability of zero (dots) or > 50 (stars) new infections ($I + I_w$) when $\mathcal{R}_0 = 8, 12, \text{or } 16$, $p = 0.80, 0.90, 0.93, \text{or } 0.95$, $\boldsymbol{\gamma_w = 3\gamma}$ **years**$^{-1}$, $\boldsymbol{G = 1}$, $\nu = 1$, $(1-q) = [0, 0.2, 0.5, 0.8, 1]$, and $p_1 = p_2 = 0$. The symbols within each colour correspond to the probabilities as k_2 increases. The colour changes as k_1 increases. $(1-q)$ increases for each subplot within each panel.

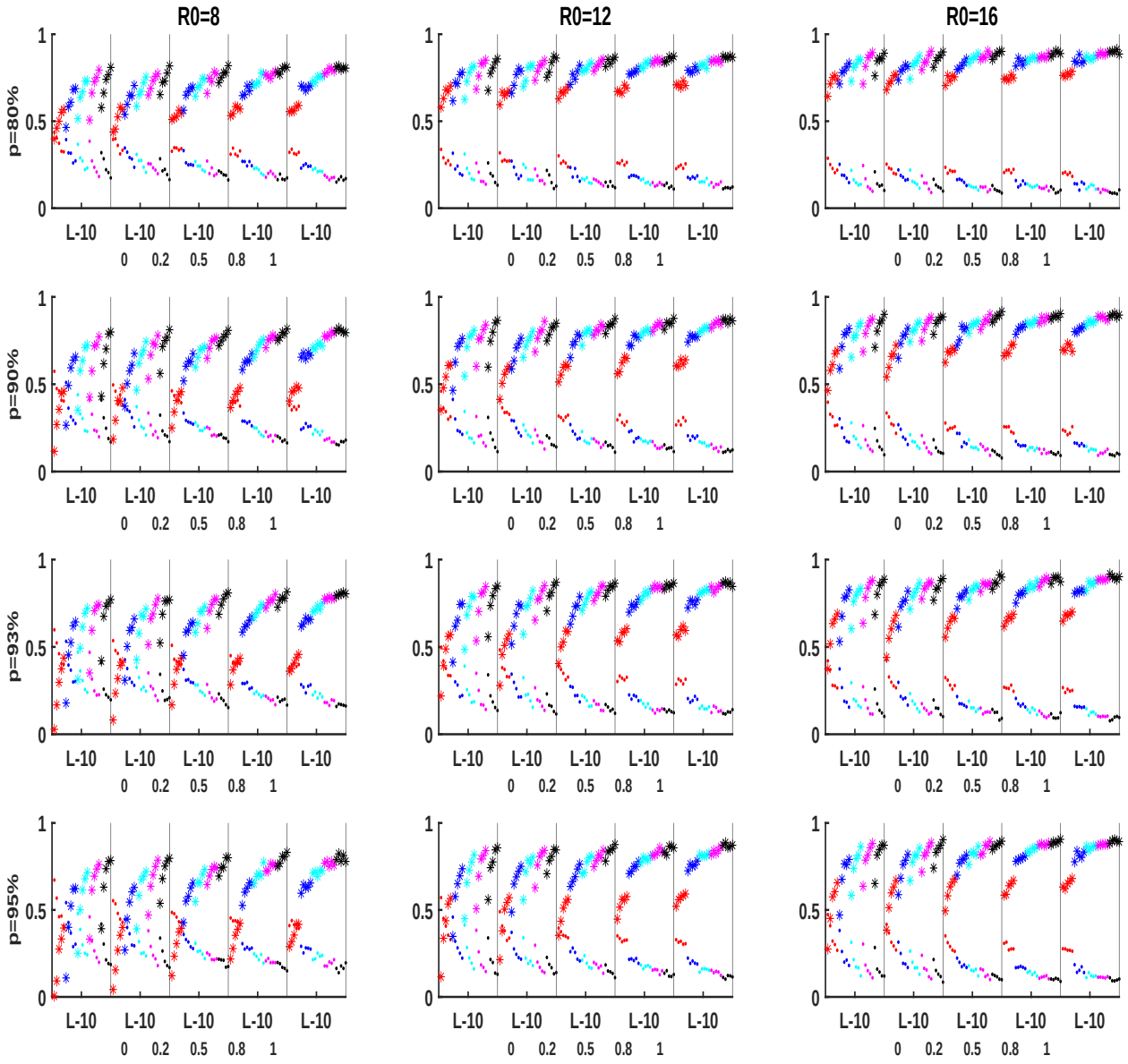

Figure 3.7: Probability of zero (dots) or > 50 (stars) new infections ($I + I_w$) when $\mathcal{R}_0 = 8, 12,$ or 16, $p = 0.80, 0.90, 0.93,$ or 0.95, $\boldsymbol{\gamma_w = 2\gamma}$ **years**$^{-1}$, $\boldsymbol{G = 1}$, $\nu = 1$, $(1-q) = (0, 0.2, 0.5, 0.8, 1)$, and $p_1 = p_2 = 0$. The symbols within each colour correspond to the probabilities as k_2 increases. The colour changes as k_1 increases. $(1-q)$ increases for each subplot within each panel.

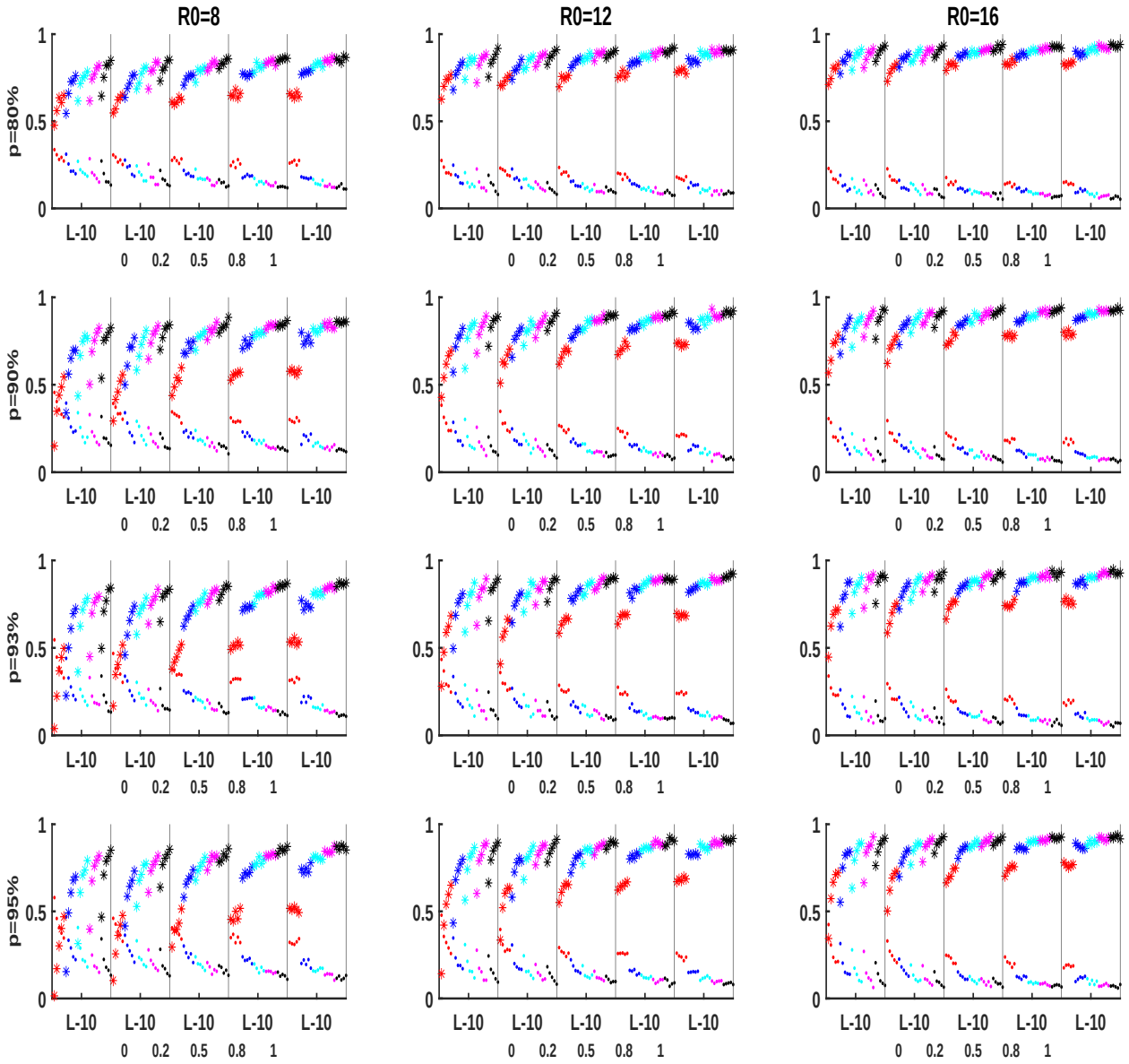

Figure 3.8: Probability of zero (dots) or > 50 (stars) new infections $(I + I_w)$ when $\mathcal{R}_0 = 8, 12,$ or 16, $p = 0.80, 0.90, 0.93,$ or 0.95, $\boldsymbol{\gamma_w} = \boldsymbol{\gamma}$ **years**$^{-1}$, $\boldsymbol{G} = \mathbf{1}$, $\nu = 1$, $(1-q) = (0, 0.2, 0.5, 0.8, 1)$, and $p_1 = p_2 = 0$. The symbols within each colour correspond to the probabilities as k_2 increases. The colour changes as k_1 increases. $(1-q)$ increases for each subplot within each panel.

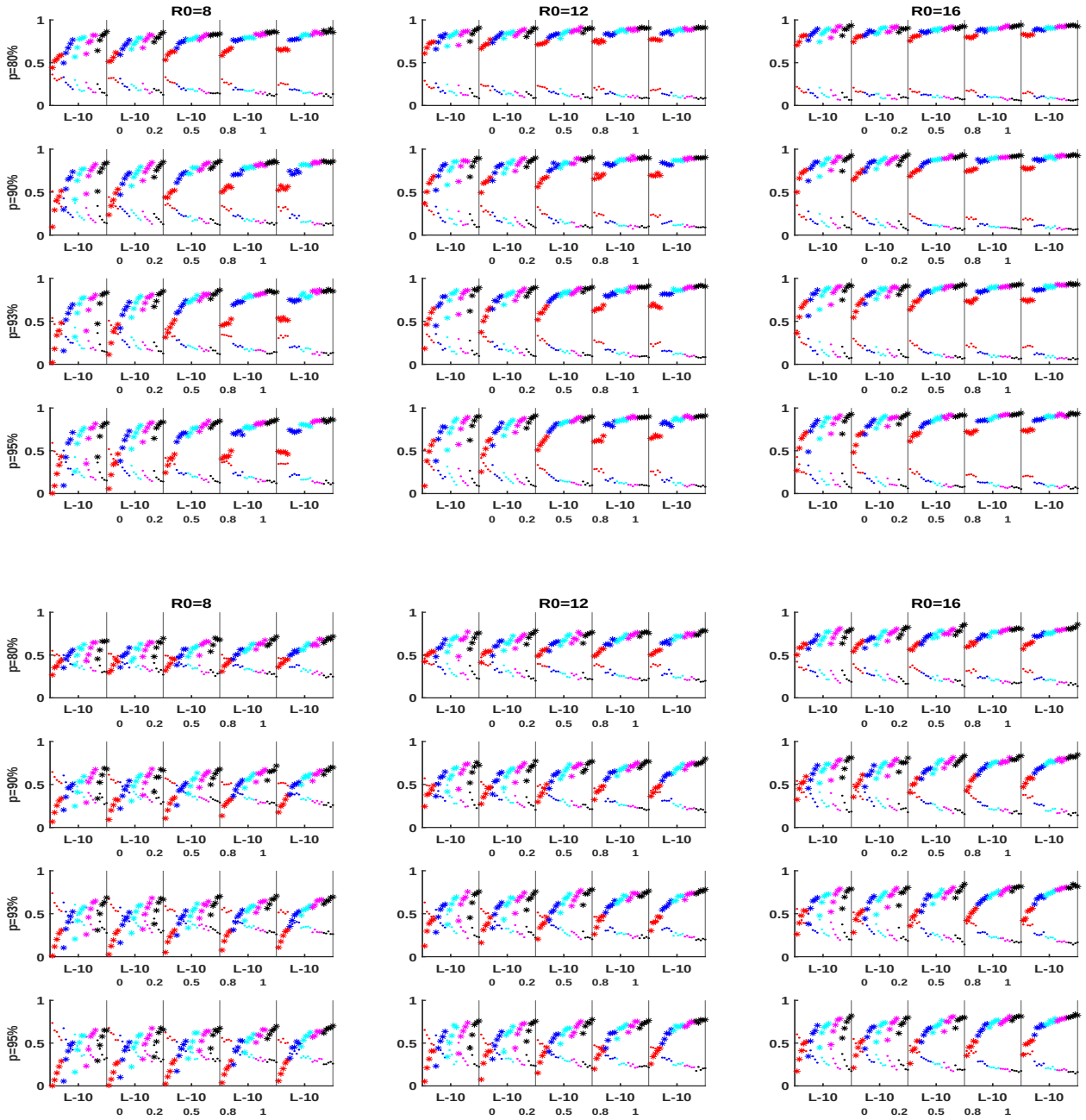

Figure 3.9: Probability of zero (dots) or > 50 (stars) new infections ($I + I_w$) when $\mathcal{R}_0 = 8, 12,$ or 16), $p = 0.80, 0.90, 0.93,$ or 0.95, $\boldsymbol{\gamma_w = (\gamma, 5\gamma)}$ **years**$^{-1}$ (top, bottom), $\boldsymbol{G = 1}$, $\nu = 1$, $(1 - q) = (0, 0.2, 0.5, 0.8, 1)$, and $\boldsymbol{p_1 = p_2 = 1/1000}$. The symbols within each colour correspond to the probabilities as k_2 increases. The colour changes as k_1 increases. $(1 - q)$ increases for each subplot within each panel.

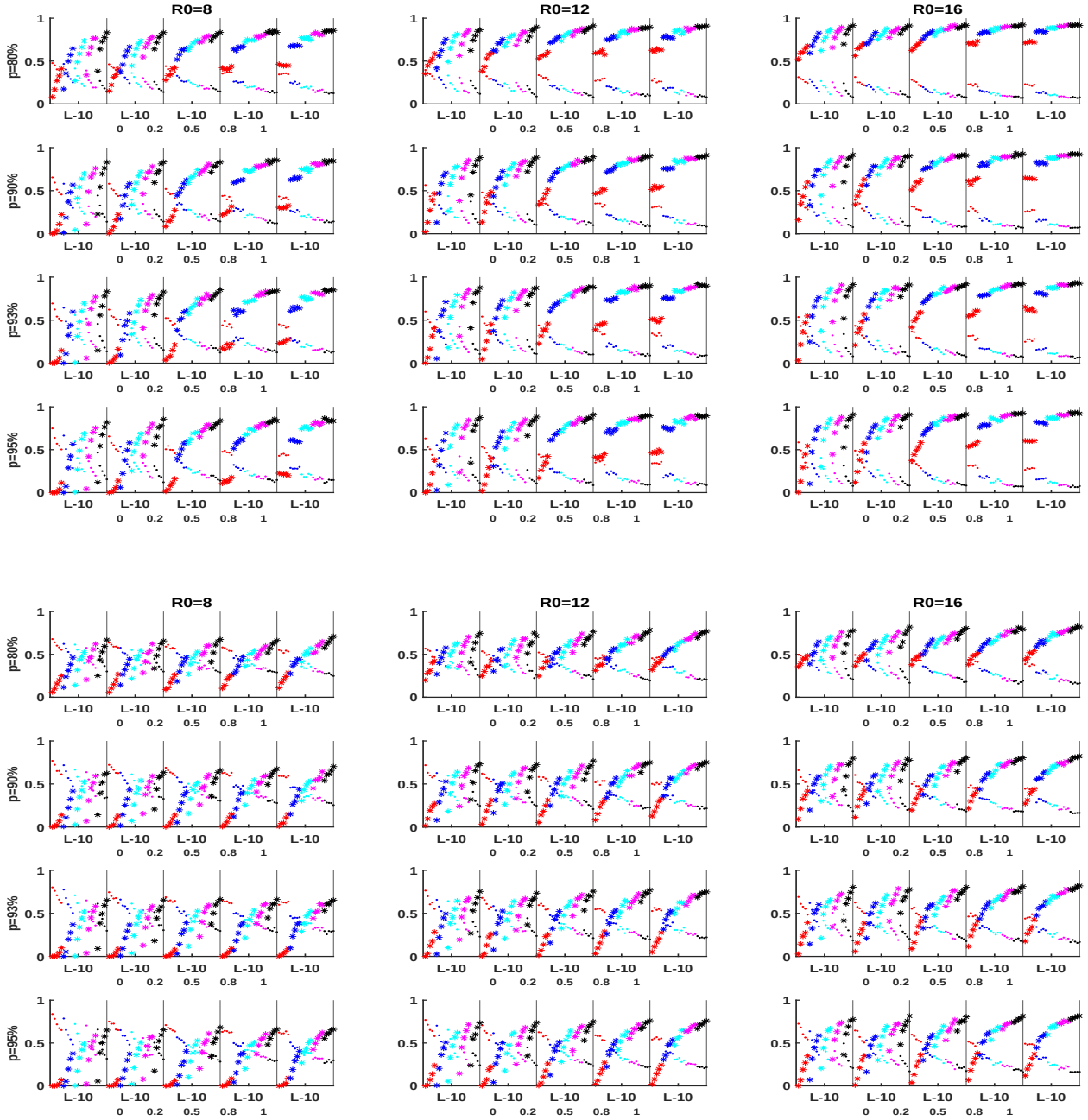

Figure 3.10: Probability of zero (dots) or > 50 (stars) new infections $(I + I_w)$ when $\mathcal{R}_0 = 8, 12,$ or 16, $p = 0.80, 0.90, 0.93,$ or 0.95, $\boldsymbol{\gamma_w = (\gamma, 5\gamma)\ \text{years}^{-1}}$ (top, bottom), $\boldsymbol{G = 1}$, $\nu = 1$, $(1 - q) = (0, 0.2, 0.5, 0.8, 1)$, and $\boldsymbol{p_1 = p_2 = 1/100}$. The symbols within each colour correspond to the probabilities as k_2 increases. The colour changes as k_1 increases. $(1 - q)$ increases for each subplot within each panel.

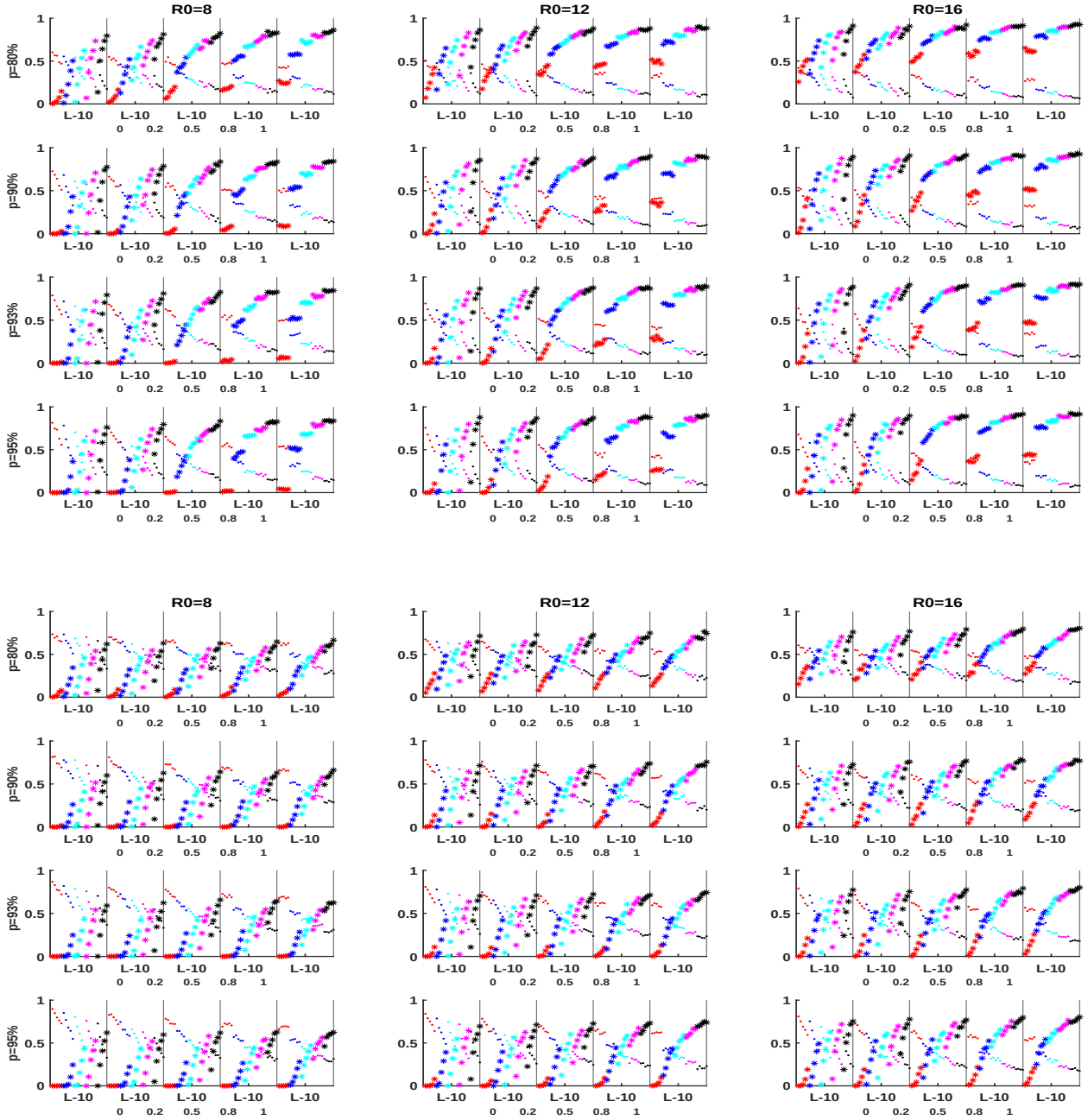

Figure 3.11: Probability of zero (dots) or > 50 (stars) new infections ($I + I_w$) when $\mathcal{R}_0 = 8, 12,$ or 16, $p = (0.80, 0.90, 0.93,$ or 0.95, $\boldsymbol{\gamma_w = (\gamma, 5\gamma)}$ **years**$^{-1}$ (top, bottom), $\boldsymbol{G = 1}$, $\nu = 1$, $(1-q) = (0, 0.2, 0.5, 0.8, 1)$, and $\boldsymbol{p_1 = p_2 = 1/50}$. The symbols within each colour correspond to the probabilities as k_2 increases. The colour changes as k_1 increases. $(1 - q)$ increases for each subplot within each panel.

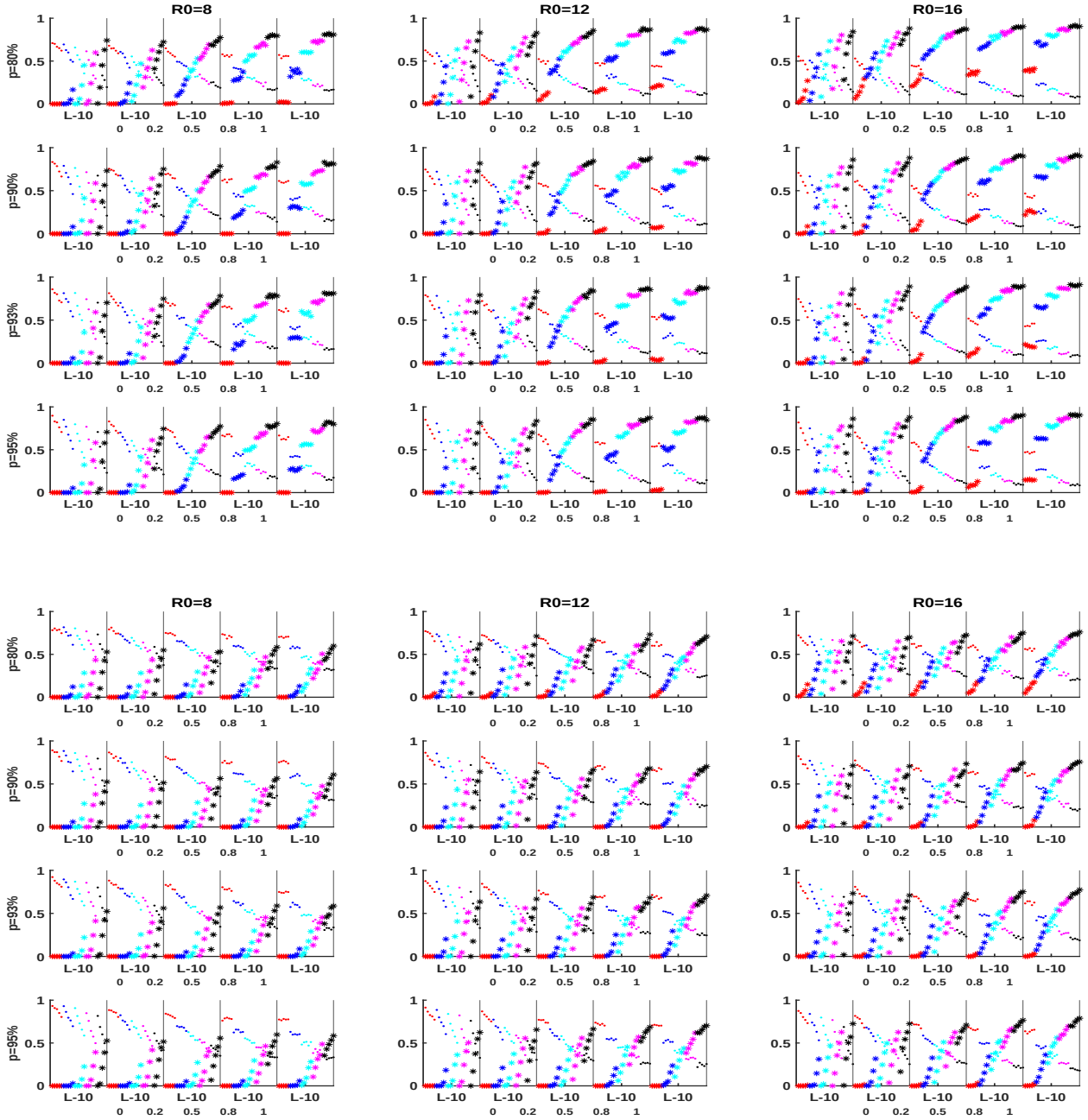

Figure 3.12: Probability of zero (dots) or > 50 (stars) new infections ($I + I_w$) when $\mathcal{R}_0 = 8, 12,$ or 16, $p = 0.80, 0.90, 0.93,$ or 0.95, $\boldsymbol{\gamma_w = (\gamma, 5\gamma)}$ **years**$^{-1}$ (top, bottom), $\boldsymbol{G = 1}$, $\nu = 1$, $(1-q) = (0, 0.2, 0.5, 0.8, 1)$, and $\boldsymbol{p_1 = p_2 = 1/25}$. The symbols within each colour correspond to the probabilities as k_2 increases. The colour changes as k_1 increases. $(1 - q)$ increases for each subplot within each panel.

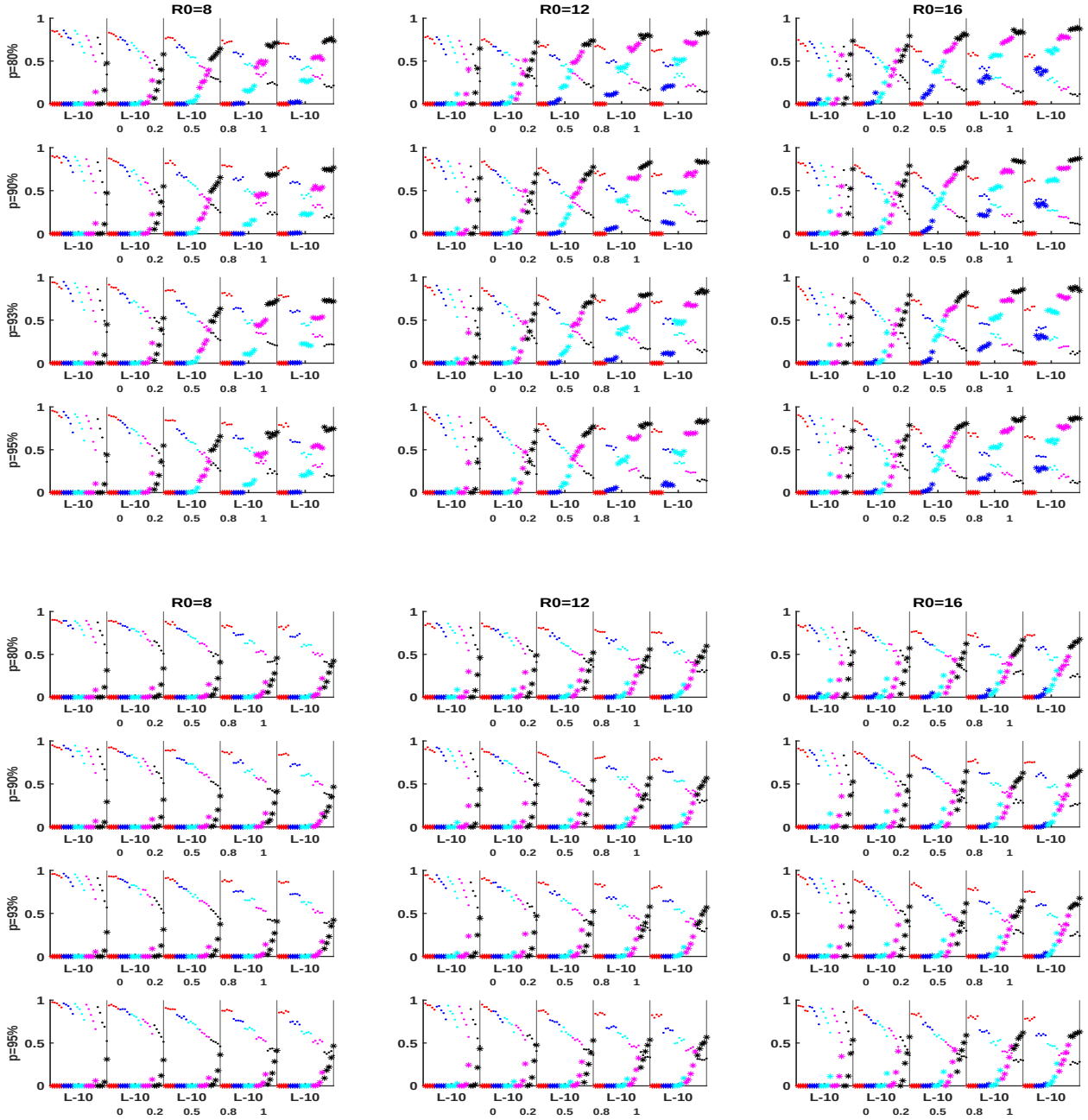

Figure 3.13: Probability of zero (dots) or > 50 (stars) new infections ($I + I_w$) when $\mathcal{R}_0 = 8, 12,$ or 16, $p = 0.80, 0.90, 0.93,$ or 0.95, $\boldsymbol{\gamma_w = (\gamma, 5\gamma)}$ **years**$^{-1}$ (top, bottom), $\boldsymbol{G = 1}$, $\nu = 1$, $(1-q) = (0, 0.2, 0.5, 0.8, 1)$, and $\boldsymbol{p_1 = p_2 = 1/10}$. The symbols within each colour correspond to the probabilities as k_2 increases. The colour changes as k_1 increases. $(1 - q)$ increases for each subplot within each panel.

3.3.7 Sensitivity Analysis

The sensitivity analysis of the model is performed using Latin Hypercube Sampling (LHS) with 2000 runs to investigate the influence of various parameters $p_1, p_2, \beta, k_1, k_2$ and G on specific public health measures of interest. Here, we consider the peak magnitude of I_w infections as this gives us a measure of the peak load of infections from the vaccinated individuals, the peak magnitude of the vaccinated population (V), or the initial condition V_0, as this allows us to compare waning immunity and vaccination rates in order of importance, and the total infections ($I + I_w$) over an outbreak as this gives us a measure of the total burden on the healthcare system. Partial Rank Correlation Coefficients (PRCC) are used to quantify the impact and direction of these parameters.

Figure 3.14(a), clearly indicates that the transmission rate (β) is the most critical factor, showing a strong positive correlation with the peak magnitude of I_w. This highlights its significant role in the prevention of I_w infections. Vaccination rate p_2 demonstrates a strong negative correlation, indicating that effective vaccination program of people with waning immunity are essential to reduce infections in this population. The waning rates k_1 and k_2 also significantly affect peak I_w where an increase in k_2 and a decrease in k_1 are needed to lessen the peak number of infections, emphasizing the need to address waning immunity to limit the resurgence of infections. In addition, parameters G and p_1 exhibit negligible effects on peak I_w.

From Figure 3.14(b), we can see that the total number of infections ($I+I_w$) is most strongly influenced by the waning immunity rates k_1, k_2, as well as the transmission rate (β), all showing a strong positive correlation with total infections.This underscores the combined role of transmission intensity and waning immunity in driving outbreak magnitude. Vaccination rates p_1 and p_2 exhibited significant negative correlations, with p_1 (vaccination from susceptible class) being more impactful, highlighting the importance of targeted vaccination campaigns. Parameter G has negligible effects on total infections.

Figure 3.14(c) plots the incidence of the peak magnitude of the vaccinated population (V), which is a measure of the initial number of individuals in the V class at the DFE. Intuitively, the vaccination rate of the susceptible class (p_1) has the strongest positive influence, highlighting its importance in increasing the vaccinated population. The waning rate from the vaccinated to the waning class (k_1) has a significant negative effect, indicating that reducing waning immunity can sustain vaccination levels. The booster vaccination rate (p_2), positively impacted V and the waning rate (k_2) from the waning to the susceptible class have a negative effect, but both with weaker effects compared to p_1 and k_1. Parameters β and G have minimal influence on the equilibrium vaccinated population.

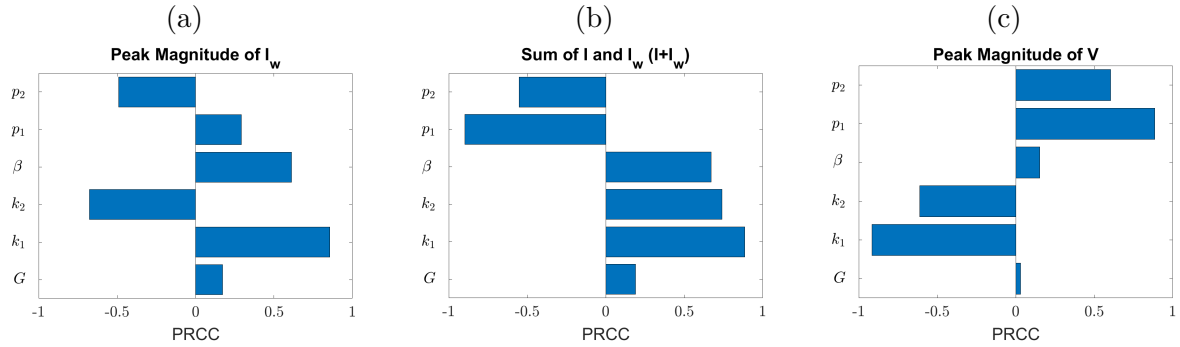

Figure 3.14: Sensitivity Analysis of (a) Peak magnitude of I_w, (b) Total infections ($I + I_w$), and (c) Peak magnitude of vaccinated individuals V

3.4 Discussion

Measles vaccine-induced immunity may wane [152]. In turn, individuals with waning vaccine-induced immunity may contract measles infection and contribute to the spread of measles. Considering this, to provide best-informed public health decision-making, new mathematical definitions of the control reproduction number, critical vaccination threshold, outbreak probability, and the final size of an outbreak of measles must be determined.

We have determined that the current and very popular approximations of the control reproduction number, $\mathcal{R}_c = \mathcal{R}_0(1-p)$ and the critical vaccination threshold, $p_c = 1 - 1/\mathcal{R}_0$,

increase if vaccine-induced immunity wanes and allows for infection in individuals with waning immunity. The new definitions of $\mathcal{R}_c$ and p_c are shown in Eq.'s (3.3) and (3.5). Figure 3.2 shows that the increase in p_c may make vaccine-induced herd immunity impossible to achieve.

Measles outbreaks are not often observed in highly vaccinated populations. Eq. (3.16) confirms this. When the type reproductions numbers $\mathcal{R}_{0,I\to I_w}$, $\mathcal{R}_{0,I_w\to I}$ and $\mathcal{R}_{0,I_w\to I_w}$ decrease, for example, when W_0, ν, $(1-q)$, and G decrease, the probability of no measles outbreak increases.

At the beginning of an outbreak it is possible to estimate the expected number of infecteds. This can be done using the final size equations shown in Eq. (3.15),(3.16). During or upon conclusion of an outbreak, these equations can also be used to estimate model parameters including the effective population that was involved in the outbreak (N), the rates of waning immunity that the vaccinated population is experiencing (k_1, k_2), and how susceptible and infectious individuals with waning vaccine-induced immunity are (G, ν, q). This is a course for future work for an analysis of the current Measles outbreak in Canada.

We have provided important updates to calculations that are commonly used to assess the risk and potential of a measles epidemic. The results of our study, however, can be improved in several aspects. First, the model assumes that the population is well-mixed. Rather, there should be a contact network whereby individuals have many contacts with their friends, family and co-workers, but less with others in the population. Second, measles is mostly a childhood infection, and the measles vaccine is provided in the childhood vaccination program. Therefore, including age structure in the model will make the model results more applicable to current observations. Finally, apart from our study of the probability of no new infections, the current model framework ignores stochastic effects throughout the outbreak. This renders any study of the variability in important public health measures such as the epidemic peak size, peak time, end time and final size infeasible. Stochastic contact- and age-structured models represent courses for future work.

Chapter 4

Influenza and Waning Immunity

4.1 Introduction

Influenza is an infectious disease that occurs frequently throughout the world and, unlike many childhood diseases such as measles, it does not provide lifelong immunity [158]. Instead, individuals who have previously been infected or vaccinated can become susceptible again due to the waning immune protection and constant evolution of the virus [159, 160]. Seasonal influenza viruses undergo ongoing antigenic drift, modifying surface proteins sufficiently to evade existing immunity in hosts [161, 162]. As a result, immunity decreases over time, not only because of the natural decline of immune memory but also because of viral changes — even populations that have been previously exposed can become susceptible to infection again. This ongoing loss of protection drives annual vaccination initiatives and supports the seasonal pattern of influenza outbreaks [163, 164]. These characteristics of viral evolution and immune response would be less concerning if influenza were a mild or self-limiting disease [165]. However, historical data reveal otherwise, emphasizing the importance of understanding how immunity is lost and restored over time [159, 166, 160, 167].

Influenza causes significant seasonal epidemics and leads to considerable illness and death worldwide. Historical records indicate its severity: the twentieth century experienced three

major pandemics — in 1918, 1957, and 1968 — each significantly influencing public health priorities [165]. The 1918 Spanish flu infected almost a third of the world's population, resulting in an estimated 250,000 deaths in Britain, more than 400,000 in France, more than 50,000 in Canada and between 500,000 and 675,000 in the United States [166]. Smaller populations faced proportionally greater losses, including nearly 12,000 deaths in Western Samoa, while Japan recorded 23 million cases and 390,000 deaths [166]. Although advances in modern medicine have reduced mortality rates, seasonal influenza still accounts for hundreds of thousands of deaths each year, with large outbreaks continuing to arise unexpectedly [167].

Despite medical advances, influenza persists because immunity does not last long [159]. Immunity decreases between seasons, allowing individuals to be reinfected and allowing the virus to resume transmission year after year [160]. Therefore, a key factor in the seasonal recurrence is not just the virus's ability to spread, but also the speed at which immunity declines and individuals return to the susceptible population [159]. The evolving nature of immunity is therefore crucial to understand the epidemiology of influenza. Individuals may experience multiple infections throughout their lives, approaching the next season with varying levels of remaining immunity based on past infections, vaccination coverage, and the rate of loss of immunity. The interaction between susceptible individuals (S) and those with reduced but not non-existent immunity (W) significantly influences transmission. Slight increases in the number of individuals with waning immunity can enhance the potential for outbreaks, alter the timing of epidemics, and determine whether seasonal infections remain mild or escalate into large-scale events [160, 158, 159].

The progression of infection also reflects biological timelines. Influenza has latent, incubation, and infectious phases [168], with an average latent period of approximately 1.9 days and an infectious time frame ranging from 2 to 10 days [169, 170, 171]. However, unlike diseases that have stable antigenic characteristics, these timelines alone do not determine long-term epidemic risk — the rate at which immunity is lost, and consequently how quickly

individuals return to the susceptible group, plays a crucial role [159, 172, 173].

To thoroughly analyze these dynamics, a mathematical framework is essential — one that differentiates between individuals who have full immunity, partial immunity, or renewed susceptibility following loss of immunity. This need prompts the creation of transmission models that can accurately reflect the redistribution of immunity from season to season and the pathways of reinfection. Mathematical transmission models offer a means to clarify these processes. Recent research has integrated factors such as household interactions, travel patterns, vaccination, and viral evolution [174, 175], yet fewer studies have specifically quantified how the redistribution of immunity from one season to the next impacts the likelihood of outbreaks and the final scale of epidemics [176, 177].

In this study, we develop and evaluate a compartmental model for seasonal influenza that accounts for both primary infections (I) and reinfections in individuals whose immunity has decreased (I_w). Our goal is to assess how factors such as vaccination rates, waning immunity, and residual immunity $R_0, R_{w,0}$, and V_0 impact effective susceptible populations S_0 and W_0 at the beginning of the season, the probability that a new influx leads to a prolonged outbreak, and the ultimate size of an epidemic wave. By clearly indicating the effects of waning immunity, we are able to measure the conditions necessary for influenza to re-establish transmission every season and identify parameter ranges in which vaccination alone may not be adequate to prevent recurring epidemics.

4.2 Model

This influenza model is an extension of the standard $SEIRS$ framework [99, 178, 25, 179, 180, 181] and is similar to the model that we analyzed in chapter 3. However, we now allow for immunity waning from the recovered classes.

The population is segmented into seven subgroups: susceptible (S): individuals at risk of contracting the disease, vaccinated (V): individuals who have received a vaccination for

influenza, waning (W): individuals in the waning stage of immunity after vaccination or recovery, primary infective (I): individuals who are fully susceptible at the time of exposure to the influenza virus, secondary infective (I_w): individuals who are exposed to the virus while in the waning stage of immunity, primary recovered (R): individuals who have recovered from primary infection and are resistant to future exposure to the influenza virus and secondary recovered (R_w): individuals who have recovered from secondary infections and are resistant to further infections.

We consider a closed population of size N, where individuals enter the system at birth or at the age of influenza vaccination. Vaccination occurs at a rate λ, which reflects the timing of seasonal influenza vaccination campaigns. A fraction p of newly recruited individuals receives the influenza vaccine and transitions to the vaccinated compartment (V), while the remaining fraction $(1-p)$ enters the susceptible compartment (S). The unvaccinated individuals in S then receive vaccination at a rate p_1, transferring to V. Susceptible individuals (S) also become infected upon contact with infectious individuals.

The infection process accounts for different levels of infectiousness between primary infecteds I and secondary infecteds I_w. We consider cases when both primary infections (I) and secondary infections (I_w) have the same level of infectiousness, when secondary infecteds I_w cannot transmit, and when I_w have a reduced level of infectiousness. The parameter G differentiates these scenarios, with $G = 1$ indicating full infectiousness for I_w, $G = 0$ indicating no infectiousness, and $0 < G < 1$ representing partial infectiousness.

The population is assumed to mix homogeneously, and the rate of infection depends on the frequency: $\beta\frac{(I+GI_w)}{N}$. Individuals in the I and I_w compartments remain infectious for $\frac{1}{\gamma}$ and $\frac{1}{\gamma_w}$ time units on average, respectively. Upon recovery, both I and I_w individuals acquire temporary immunity and transition to R or R_w, respectively. Recovered individuals R and R_w can lose immunity over time. It is assumed that immunity decays with rates k_3 and k_4 from these compartments, respectively, to the waning immunity class W.

In our model we assume that vaccinated individuals receive full protection from infection. However, we also assume that vaccination only provides temporary immunity, and individuals transition from V to W after a period of $\frac{1}{k_1}$ on average. Individuals in W may lose immunity over time (rate k_2) and return to S. Alternatively, contact with infected individuals may lead to either immunity boosting after which an individual will transition back to V, or secondary infection through which they transition to I_w. The transition rate from W to V or I_w is governed by $\nu\beta(I + GI_w)$, with a proportion q moving to V and $1 - q$ moving to I_w. Parameter $0 \leq \nu \leq 1$ denotes reduced susceptibility of W compared to S. The waning individuals in the compartment W can receive vaccination at a rate p_2 and move to the Vaccinated class V.

Natural mortality for all model compartments i.e., dS, dI, dI_w, dW, dV, dR, and dR_w, is included in our model. We assume that birth and natural death are balanced so that we are working with a constant population size.

The following set of ordinary differential equations describes the model

$$\begin{aligned}
S' &= \lambda(1-p) - \beta S(I + GI_w) + k_2 W - p_1 S - dS \\
I' &= \beta S(I + GI_w) - \gamma I - dI \\
I'_w &= \nu(1-q)\beta(I + GI_w)W - \gamma_w I_w - dI_w \\
R' &= \gamma I - k_3 R - dR \\
R'_w &= \gamma_w I_w - k_4 R_w - dR_w \\
V' &= \lambda p - k_1 V + q\nu\beta(I + GI_w)W + p_1 S + p_2 W - dV \\
W' &= k_1 V - \nu\beta(I + GI_w)W - k_2 W - p_2 W + k_3 R + k_4 R_w - dW
\end{aligned} \tag{4.1}$$

Figure 4.1 illustrates the flow diagram of these dynamics. Table 4.1 lists the model parameters.

Parameter	**Definition**	**Values**
λ	Birth Rate (people x year^{-1})	$1/82$
p	Fraction of newborns effective vaccination (obtained vaccine and gained a level of neutralizing Immunity)	$[0.7, 1]$
d	Natural death rate (year^{-1})	$1/82$
$\mathcal{R}_0$	Basic reproduction number	$[1.5, 3]$
β	Infection rate (year^{-1})	$[39.018, 78.036]$ Calculated from $\mathcal{R}_0$
γ	Recovery rate (year^{-1})	$365/5$
γ_w	Recovery rate from I_w (year^{-1})	$(1, 2, 3, 4, 5) * \gamma$
ν	Boosting proportionality constant	$[0, 1]$
G	Infectiousness that I_w can have comparing I	$[0, 1]$
q	Fraction of those boosted that move to V. (1-q) experience mild infection and are boosted to R (via I_w)	$[0, 1]$
k_1	Waning rate from V to W (year^{-1})	$[1/300, 1/10]$
k_2	Waning rate from W to S (year^{-1})	$[1/300, 1/10]$
k_3	Waning rate from R to W (year^{-1})	$[0, 4/10]$
k_4	Waning rate from R_w to W (year^{-1})	$[0, 4/10]$
p_1	Vaccination rate between S and V	$[0, 1/10]$
p_2	Vaccination rate between W and V	$[0, 1/10]$

Table 4.1: Table of parameters for Model (4.1)

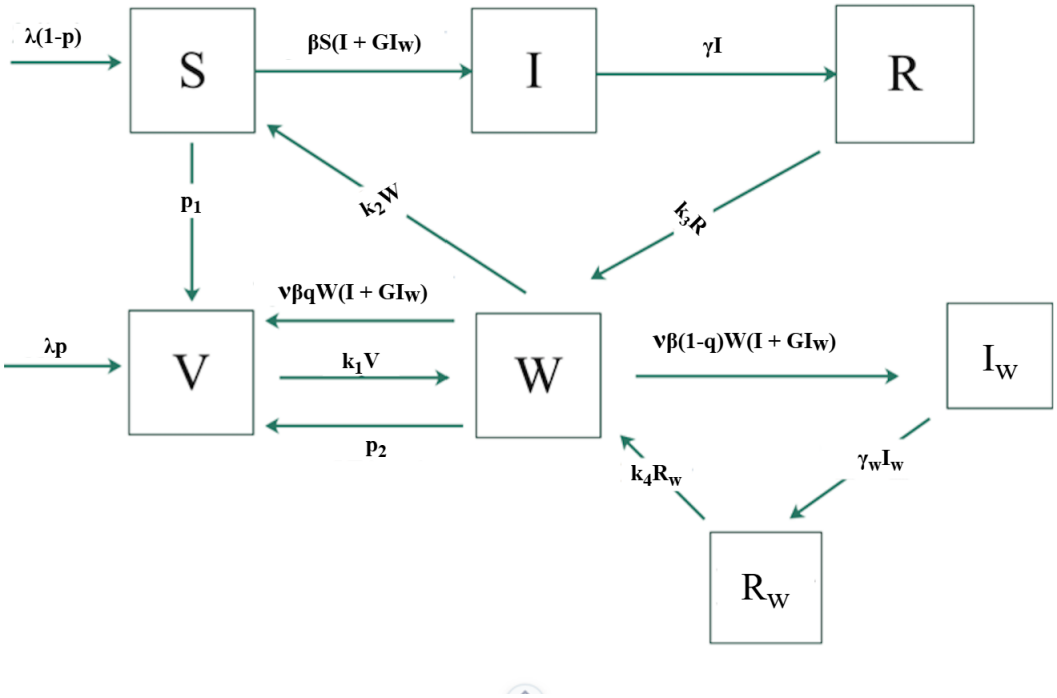

Figure 4.1: Flow diagram of Model (4.1)

4.3 Results

4.3.1 Disease free equilibrium

Model (4.1) has a disease free equilibrium $E_0 = (S_0, I_0, I_{w0}, R_0, R_{w0}, V_0, W_0)$ $= (S_0, 0, 0, 0, 0, V_0, W_0)$ where

$$\begin{aligned} S_0 &= \frac{d(1-p)(d+k_1+k_2+p_2)+k_1k_2}{d^2+(k_1+k_2+p_1+p_2)d+(k_1+k_2+p_2)p_1+k_1k_2} \\ V_0 &= \frac{(dp+p_1)(d+k_2+p_2)}{d^2+(k_1+k_2+p_1+p_2)d+(k_1+k_2+p_2)p_1+k_1k_2} \\ W_0 &= \frac{k_1(dp+p_1)}{d^2+(k_1+k_2+p_1+p_2)d+(k_1+k_2+p_2)p_1+k_1k_2} \end{aligned} \tag{4.2}$$

4.3.2 Basic Reproduction Number

Using the Next Generation Method [24, 104], the basic reproduction number of Model (4.1) is

$$\mathcal{R}_0 = \frac{\beta N}{(\gamma + d)} .$$

4.3.3 Control Reproduction Number

The control reproduction number of Model (4.1) can be determined for a particular outbreak and is related to the distribution of S and W at the time of outbreak start. If the outbreak starts at the DFE, Using the Next Generation Method [24, 104] the control reproduction number corresponds to

$$\begin{aligned}\mathcal{R}_c = \quad & \mathcal{R}_0 \left[\tfrac{d(1-p)(d+k_1+k_2+p_2)+k_1k_2}{d^2+(k_1+k_2+p_1+p_2)d+(k_1+k_2+p_2)p_1+k_1k_2}\right] \\ & +\mathcal{R}_0 \left[Gk_1\nu(1-q)\tfrac{(d+\gamma)(dp+p_1)}{(d^2+(k_1+k_2+p_1+p_2)d+(k_1+k_2+p_2)p_1+k_1k_2)(d+\gamma_w)}\right] .\end{aligned}$$

However, for any initial conditions of S and W, which is relevant to this case since influenza initial conditions for a flu season are unlikely to reside at the DFE, we have the following

$$\mathcal{R}_c = \quad \tfrac{\mathcal{R}_0}{N}\left[S_0 + W_0 G\nu(1-q)\tfrac{(d+\gamma)}{d+\gamma_w}\right] .$$

4.3.4 Critical Vaccination Threshold

Setting $\mathcal{R}_c = 1$ we have the following inequality that we need to satisfy in order for a population to have protection against infection

$$G\nu(1-q)\left(\frac{d+\gamma}{d+\gamma_w}\right) < \left(\frac{N-\mathcal{R}_0 S_0}{\mathcal{R}_0 W_0}\right) \tag{4.3}$$

$$G\nu(1-q)\left(\frac{d+\gamma}{d+\gamma_w}\right) > \left(\frac{N-\mathcal{R}_0 S_0}{\mathcal{R}_0 W_0}\right) \tag{4.4}$$

which relates the reduced infectiousness of I_w (G), the susceptibility of W (ν), the probability that a newly exposed W becomes an $I_w(1-q)$, and the ratio of the average time that one spends in the I and I_w classes, to the total population size N and the initial population sizes of S_0 and W_0. Noting that $N = S_0 + W_0 + V_0 + R_0$ at the beginning of an influenza outbreak, if we have some measure of these initial conditions and the model parameters involved in the calculation of $\mathcal{R}_c$, we can determine how many S and W individuals need to be vaccinated so that the population is protected from infection.

If the system resides at the DFE, the critical vaccination threshold corresponds to that found for the measles system in the previous chapter, Eq.(3.5). However, unlike measles, seasonal influenza is characterized by waning post-infection and post-vaccination immunity, as well as a partial susceptibility in the W class. Consequently, vaccination must account not only for the removal of susceptible individuals (S), but also for boosting waned individuals (W), both of whom can contribute to early transmission. To reflect this biological reality, we consider vaccination applied uniformly to both classes by setting:

$$p_1 = p_2 = p_c,$$

and substitute this into Eq. (3.5). This represents a realistic public-health decision question for influenza: *what proportion of the population (both susceptible and waned) must receive vaccination before the season begins in order to prevent epidemic growth?*

Carrying out this substitution in Eq. (3.5) and introducing the shorthand

$$H_0 = d + k_1 + k_2, \qquad F = Gk_1\nu(1-q),$$

we obtain

$$p_c = \left(1 - \frac{1}{\mathcal{R}_0}\right) \frac{\Big(d(H_0 + p_c) + k_1k_2\Big)(d + \gamma_w)}{d\Big((H_0 + p_c)(d + \gamma_w) - F(d + \gamma)\Big)}$$

$$- p_c \frac{(H_0 + p_c)(d + \gamma_w) - F(d + \gamma)\mathcal{R}_0}{\mathcal{R}_0 d\Big((H_0 + p_c)(d + \gamma_w) - F(d + \gamma)\Big)}. \tag{4.5}$$

Define:

$$D(p_c) = (H_0 + p_c)(d + \gamma_w) - F(d + \gamma), \tag{4.6}$$

$$N_1(p_c) = \Big(d(H_0 + p_c) + k_1 k_2\Big)(d + \gamma_w), \tag{4.7}$$

$$N_2(p_c) = (H_0 + p_c)(d + \gamma_w) - F(d + \gamma)\mathcal{R}_0. \tag{4.8}$$

Then Eq. (4.5) can be written as:

$$p_c = \left(1 - \frac{1}{\mathcal{R}_0}\right) \frac{N_1(p_c)}{d\, D(p_c)} - p_c \frac{N_2(p_c)}{\mathcal{R}_0 d\, D(p_c)}. \tag{4.9}$$

Multiplying Eq. (4.9) by the common denominator $\mathcal{R}_0 d\, D(p_c)$ and rearranging gives

$$(\mathcal{R}_0 - 1)\, N_1(p_c) - p_c\, N_2(p_c) - p_c\, \mathcal{R}_0 d\, D(p_c) = 0. \tag{4.10}$$

Expanding $N_1(p_c)$, $N_2(p_c)$, and $D(p_c)$ in powers of p_c and collecting like terms yields a quadratic equation in p_c of the form:

$$A p_c^2 + B p_c + C = 0, \tag{4.11}$$

where

$$A = (d + \gamma_w)\Big(\mathcal{R}_0 d + 1\Big), \tag{4.12}$$

$$B = (d + \gamma_w)\Big(\mathcal{R}_0 d^2 + \mathcal{R}_0 d(k_1 + k_2 - 1) + 2d + k_1 + k_2\Big) - \mathcal{R}_0(d + 1)(d + \gamma)\, G k_1 \nu (1 - q), \tag{4.13}$$

$$C = -(\mathcal{R}_0 - 1)(d + \gamma_w)(d + k_1)(d + k_2). \tag{4.14}$$

Thus, the explicit critical vaccination threshold needed to block seasonal influenza transmission is

$$\boxed{p_c = \frac{-B + \sqrt{B^2 - 4AC}}{2A}} \qquad 0 \le p_c \le 1. \tag{4.15}$$

This formula quantifies the minimum proportion of the population that must be vaccinated (between both S and W groups) at the start of a season to ensure $\mathcal{R}_c < 1$, and therefore prevent the establishment of a seasonal influenza outbreak.

4.3.5 Final Size Relation

We consider Model (4.1) without demographics in order to quantify the outcome of an influenza outbreak. Let set $I_0 = I(0)$, $I_{w,0} = I_w(0)$.

Pre-wave reallocation (seasonal closure): explicit $S_0 = f(\cdot)$ and $W_0 = g(\cdot)$

To model the start of a yearly influenza wave, we posit a short pre-wave window $[0^-, 0]$ of length $\Delta > 0$ during which infections are negligible ($I \approx I_w \approx 0$), but the linear vaccination/waning/return flows act. Over this window

$$S' \approx k_2 W - (p_1 + d)S, \tag{4.16}$$

$$W' \approx k_1 V - (k_2 + p_2 + d)W + k_3 R + k_4 R_w, \tag{4.17}$$

$$V' \approx -(k_1 + d)V + p_1 S + p_2 W, \tag{4.18}$$

$$R' \approx -(k_3 + d)R, \qquad R_w' \approx -(k_4 + d)R_w. \tag{4.19}$$

(Over a few days, the birth input λ contributes only $O(\lambda\Delta)$ and is neglected in this closure.)

Quasi-steady ratios for (S, W, V) at 0^- (no R, R_w inflow yet). At the start of the window ($t = 0^-$), we balance the homogeneous linear (S, W, V) subsystem by setting the

drifts (without $k_3R + k_4R_w$) to zero:

$$0 = k_2W^- - (p_1 + d)S^-, \qquad 0 = k_1V^- - (k_2 + p_2 + d)W^-. \tag{4.20}$$

This gives the ratios

$$W^- \;=\; \frac{k_1}{k_2 + p_2 + d}\,V^-, \qquad S^- \;=\; \frac{k_2}{p_1 + d}\,W^- \;=\; \frac{k_1k_2}{(p_1 + d)(k_2 + p_2 + d)}\,V^-. \tag{4.21}$$

First-order update over $[0^-, 0]$. Integrating Eq.'s (4.16)–(4.19) to first order in Δ we have

$$S_0 \equiv S(0) \;\approx\; S^- + \Big[k_2W^- - (p_1 + d)S^-\Big]\Delta, \tag{4.22}$$

$$W_0 \equiv W(0) \;\approx\; W^- + \Big[k_1V^- + k_3R_0 + k_4R_{w,0} - (k_2 + p_2 + d)W^-\Big]\Delta, \tag{4.23}$$

$$V_0 \equiv V(0) \;\approx\; V^- + \Big[-(k_1 + d)V^- + p_1S^- + p_2W^-\Big]\Delta. \tag{4.24}$$

Using Eq. (4.20), the brackets in Eq. (4.22) cancel and the first/last terms in Eq. (4.23) cancel, so

$$S_0 = S^-, \qquad W_0 = W^- + \Big(k_3R_0 + k_4R_{w,0}\Big)\Delta, \qquad V_0 = V^- + O(\Delta^2). \tag{4.25}$$

To first order, we may therefore set $V^- \approx V_0$ in Eq. (4.21). Substituting $V^- \mapsto V_0$ into Eq. (4.21) and then using Eq. (4.25) yields the explicit pre-wave maps

$$\begin{aligned} S_0 \;&=\; \frac{k_1k_2}{(p_1 + d)\,(k_2 + p_2 + d)}\,V_0, \\ W_0 \;&=\; \frac{k_1}{k_2 + p_2 + d}\,V_0 \;+\; \Big(k_3R_0 + k_4R_{w,0}\Big)\,\Delta, \end{aligned} \tag{4.26}$$

i.e., $S_0 = f(R_0, R_{w,0}, V_0)$ and $W_0 = g(R_0, R_{w,0}, V_0)$.

Observation 2 (Seasonal interpretation). The state $(R_0, R_{w,0}, V_0)$ at the start of a season reflects immunity from the previous influenza season (and off-season vaccination). The short pre-wave reallocation Eq. (4.26) produces the *effective* susceptible stocks (S_0, W_0) that face the coming wave.

Susceptible integrals (Step 1)

During the influenza season (a wave of infection), we adopt the standard short-wave approximation (demography/vaccination/waning are slow versus the wave), so

$$\frac{dS}{dt} \approx -\beta S(I + GI_w), \qquad \frac{dW}{dt} \approx -\nu\beta W(I + GI_w).$$

Integrating from 0 to ∞ gives the following:

$$\ln\Big(\frac{S_0}{S_\infty}\Big) = \beta \int_0^\infty (I + GI_w)\, dt, \qquad \ln\Big(\frac{W_0}{W_\infty}\Big) = \nu\beta \int_0^\infty (I + GI_w)\, dt. \tag{4.27}$$

Total infectious time (Step 2)

Consider a matrix of removals from the infected classes $\mathcal{V} = \mathrm{diag}(\gamma + d, \gamma_w + d)$ and the following

$$I' = F_I(t) - (\gamma + d)I, \qquad I'_w = F_w(t) - (\gamma_w + d)I_w,$$

with inflows $F_I = \beta S(I + GI_w)$, $F_w = \nu(1 - q)\beta W(I + GI_w)$. Integrating and using $I(\infty) = I_w(\infty) = 0$,

$$\int_0^\infty I\, dt = \frac{1}{\gamma + d}\Big(\int_0^\infty F_I\, dt + I_0\Big), \qquad \int_0^\infty I_w\, dt = \frac{1}{\gamma_w + d}\Big(\int_0^\infty F_w\, dt + I_{w,0}\Big). \tag{4.28}$$

But cumulative inflows are equal to losses from S, W:

$$\int_0^\infty F_I\, dt = S_0 - S_\infty, \qquad \int_0^\infty F_w\, dt = W_0 - W_\infty. \tag{4.29}$$

Therefore,

$$\int_0^\infty I\,dt = \frac{S_0 - S_\infty + I_0}{\gamma + d}, \qquad \int_0^\infty I_w\,dt = \frac{W_0 - W_\infty + I_{w,0}}{\gamma_w + d}. \tag{4.30}$$

Final size equations (Step 3)

We now substitute Eq.(4.30) into Eq. (4.27) and define

$$\Gamma_1 := \frac{\beta}{\gamma + d}, \qquad \Gamma_2 := \frac{\beta G \nu (1-q)}{\gamma_w + d}.$$

and we obtain the following final size relation:

$$\ln\Big(\frac{S_0}{S_\infty}\Big) = \Gamma_1(S_0 - S_\infty) + \Gamma_2(W_0 - W_\infty) + \Gamma_1 I_0 + \Gamma_2 I_{w,0}, \tag{4.31}$$

$$\ln\Big(\frac{W_0}{W_\infty}\Big) = \nu\Big[\Gamma_1(S_0 - S_\infty) + \Gamma_2(W_0 - W_\infty) + \Gamma_1 I_0 + \Gamma_2 I_{w,0}\Big]. \tag{4.32}$$

Eliminating W_∞ via

$$W_\infty = W_0\left(\frac{S_\infty}{S_0}\right)^\nu, \tag{4.33}$$

and substituting Eq. (4.33) into Eq. (4.31) to get a scalar nonlinear equation in S_∞:

$$\ln\Big(\frac{S_0}{S_\infty}\Big) = \Gamma_1(S_0 - S_\infty) + \Gamma_2\left[W_0 - W_0\left(\frac{S_\infty}{S_0}\right)^\nu\right] + \Gamma_1 I_0 + \Gamma_2 I_{w,0}. \tag{4.34}$$

Here S_0 and W_0 are the *explicit* pre-wave functions Eq. (4.26) of $(R_0, R_{w,0}, V_0)$ and parameters (including the short window Δ). And

$$W_\infty = W_0\left(\frac{S_\infty}{S_0}\right)^\nu.$$

4.3.6 Sensitivity Analysis

The sensitivity analysis of the influenza model was performed using Latin Hypercube Sampling (LHS) with 2000 runs to investigate the influence of various parameters $p_1, p_2, \beta, k_1, k_2, k_3, k_4, G$ on the peak magnitude of secondary infections (I_w), the peak magnitude of the vaccinated population (V), and the total infections ($I + I_w$). Partial Rank Correlation Coefficients (PRCC) were used to quantify the impact and direction of these parameters.

Figure 4.2(a) clearly indicates that the transmission rate (β) is the most critical factor, showing a strong positive correlation with the peak magnitude of I_w. This highlights its significant role in the prevention of secondary infections. All other parmeters are not deemed significant, but the correlation coefficient for p_1 is close to a magnitude of 0.5. This shows that vaccination to reduce the S class will help to decrease peak I_w.

From Figure 4.2(b) we can see that the transmission rate (β) is the dominant parameter affect the total number of $I + I_w$ produced over the flu season. This underscores the critical need to implement measures that reduce disease spread. Vaccination rates p_1 and p_2, while having non-significant PRCC values, exhibit negative correlations, so targeted vaccination could be important.

Figure 4.2(b) plots the incidence of the Peak Magnitude of the vaccinated population (V). The vaccination rate of the susceptible class (p_1) has the strongest positive influence, highlighting its importance in increasing the vaccinated population. The waning rate from the vaccinated to the waning class (k_1) has a significant negative effect, indicating that reducing waning immunity can sustain vaccination levels. Other parameters, such as the booster vaccination rate (p_2) and the transmission rate (β), also positively impacted V but to a lesser extent.

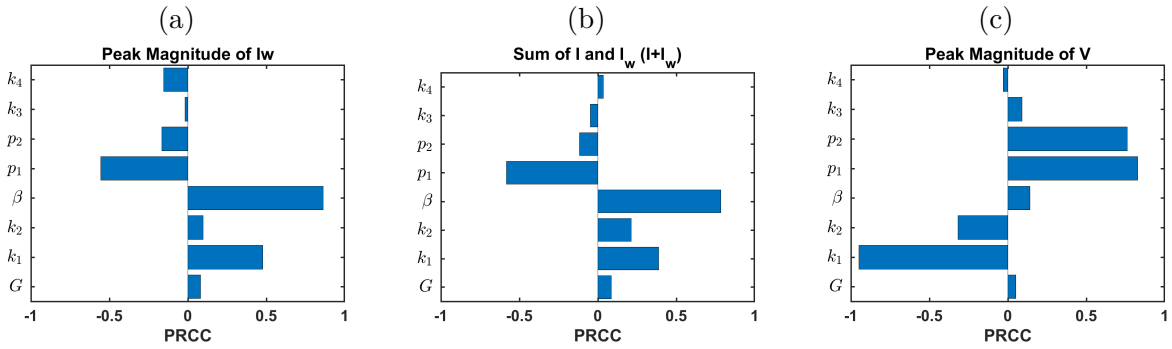

Figure 4.2: Sensitivity Analysis of (a) Peak magnitude of secondary infection I_w, (b) Sum of primary and secondary infection $(I + I_w)$, and (c) Peak magnitude of vaccinated individuals V

4.3.7 Influenza Outbreaks

In the early phase of the wave, when $S \approx S_0$ and $W \approx W_0$ are effectively constant and I, I_w are rare, the infection dynamics can be approximated by an approximation of the branching process with infectious types I (primary infections) and I_w (infections in previously waned individuals). Linearizing the infection subsystem around $(I, I_w) = (0, 0)$ yields

$$I' = \beta S_0(I + GI_w) - \gamma I, \qquad I'_w = \nu(1-q)\beta W_0(I + GI_w) - \gamma_w I_w.$$

As in the final size derivation, we define

$$\Gamma_1 := \frac{\beta}{\gamma}, \qquad \Gamma_2 := \frac{\beta G \nu(1-q)}{\gamma_w},$$

so that the type reproduction numbers $\mathcal{R}_{0,A\to B}$ (expected number of new infections of type $B \in \{I, I_w\}$ caused by a single infectious individual of type $A \in \{I, I_w\}$) are

$$\mathcal{R}_{0,I\to I} = \frac{\beta S_0}{\gamma} = \Gamma_1 S_0,$$
$$\mathcal{R}_{0,I\to I_w} = \frac{\beta \nu(1-q)W_0}{\gamma},$$

$$\mathcal{R}_{0,I_w\to I} = \frac{\beta G S_0}{\gamma_w},$$
$$\mathcal{R}_{0,I_w\to I_w} = \frac{\beta G \nu (1-q) W_0}{\gamma_w} = \Gamma_2 W_0.$$

The total expected number of secondary infections (of either type) produced by a single infectious individual of type A is then

$$\mathcal{R}^{\text{tot}}_{0,I} := \mathcal{R}_{0,I\to I} + \mathcal{R}_{0,I\to I_w} = \frac{\beta}{\gamma}\Big(S_0 + \nu(1-q)W_0\Big),$$
$$\mathcal{R}^{\text{tot}}_{0,I_w} := \mathcal{R}_{0,I_w\to I} + \mathcal{R}_{0,I_w\to I_w} = \frac{\beta G}{\gamma_w}\Big(S_0 + \nu(1-q)W_0\Big).$$

Following the same approximation used in the measles case (Chapter:3.3.6), we assume that the total number of secondary infections generated by a single infectious individual of type A is distributed with mean $\mathcal{R}^{\text{tot}}_{0,A}$. Under this assumption, the probability that a branching process starting from one individual of type A eventually goes extinct (i.e., there is no macroscopic outbreak) is approximated by

$$\Pr(\text{no outbreak} \mid A_0 = 1) \approx \frac{1}{1+\mathcal{R}^{\text{tot}}_{0,A}}, \qquad A \in \{I, I_w\}.$$

Explicitly, for the influenza model,

$$\Pr(\text{no outbreak} \mid I_0 = 1) \approx \frac{1}{1+\mathcal{R}^{\text{tot}}_{0,I}} = \frac{1}{1+\frac{\beta}{\gamma}\Big(S_0 + \nu(1-q)W_0\Big)}, \tag{4.35}$$

$$\Pr(\text{no outbreak} \mid I_{w,0} = 1) \approx \frac{1}{1+\mathcal{R}^{\text{tot}}_{0,I_w}} = \frac{1}{1+\frac{\beta G}{\gamma_w}\Big(S_0 + \nu(1-q)W_0\Big)}. \tag{4.36}$$

If the epidemic is seeded by a single infectious individual of type I with probability $\Pr(I_0 = 1)$ and by a single infectious individual of type I_w with probability $\Pr(I_{w,0} = 1)$ (with $\Pr(I_0 = 1)+$

$\Pr(I_{w,0} = 1) = 1)$, the overall probability of no outbreak is:

$$\begin{aligned}\Pr(\text{no outbreak}) &\approx \Pr(I_0 = 1) \cdot \frac{1}{1 + \mathcal{R}_{0,I}^{\text{tot}}} + \Pr(I_{w,0} = 1) \cdot \frac{1}{1 + \mathcal{R}_{0,I_w}^{\text{tot}}} \\ &= \Pr(I_0 = 1) \cdot \frac{1}{1 + \frac{\beta}{\gamma + d}\Big(S_0 + \nu(1-q)W_0\Big)} \\ &+ \Pr(I_{w,0} = 1) \cdot \frac{1}{1 + \frac{\beta G}{\gamma_w + d}\Big(S_0 + \nu(1-q)W_0\Big)}\end{aligned}$$

Here S_0 and W_0 are the effective pre-wave susceptible stocks given explicitly by Eq. (4.26) as functions of $(R_0, R_{w,0}, V_0)$ and the parameters (including the short pre-wave window length Δ). Thus, the branching-process approximation links the outbreak probability in the upcoming influenza season directly to the immunity carried over from the previous season.

We perform stochastic simulations for the influenza model using the same methodology as we applied in Chapter 3 for measles, now incorporating the waning of natural immunity through parameters k_3 and k_4, allowing individuals in R and R_w to gradually return to susceptibility. We explore a range of biological uncertainties by varying $k_3, k_4 \in [0, 0.4]$ yrs^{-1}, and we simulate different values of $R_0 = 1.5, 2, \text{or } 3)$ and vaccination coverage $p = 0.45, 0.55, 0.65, \text{or } 0.80$. Since seasonal influenza vaccination campaigns generally occur before the epidemic season rather than during active transmission, we assume $p_1 = p_2 = 0$, meaning no additional vaccine is administered once an outbreak begins, and outbreak dynamics are driven primarily by pre existing immunity.

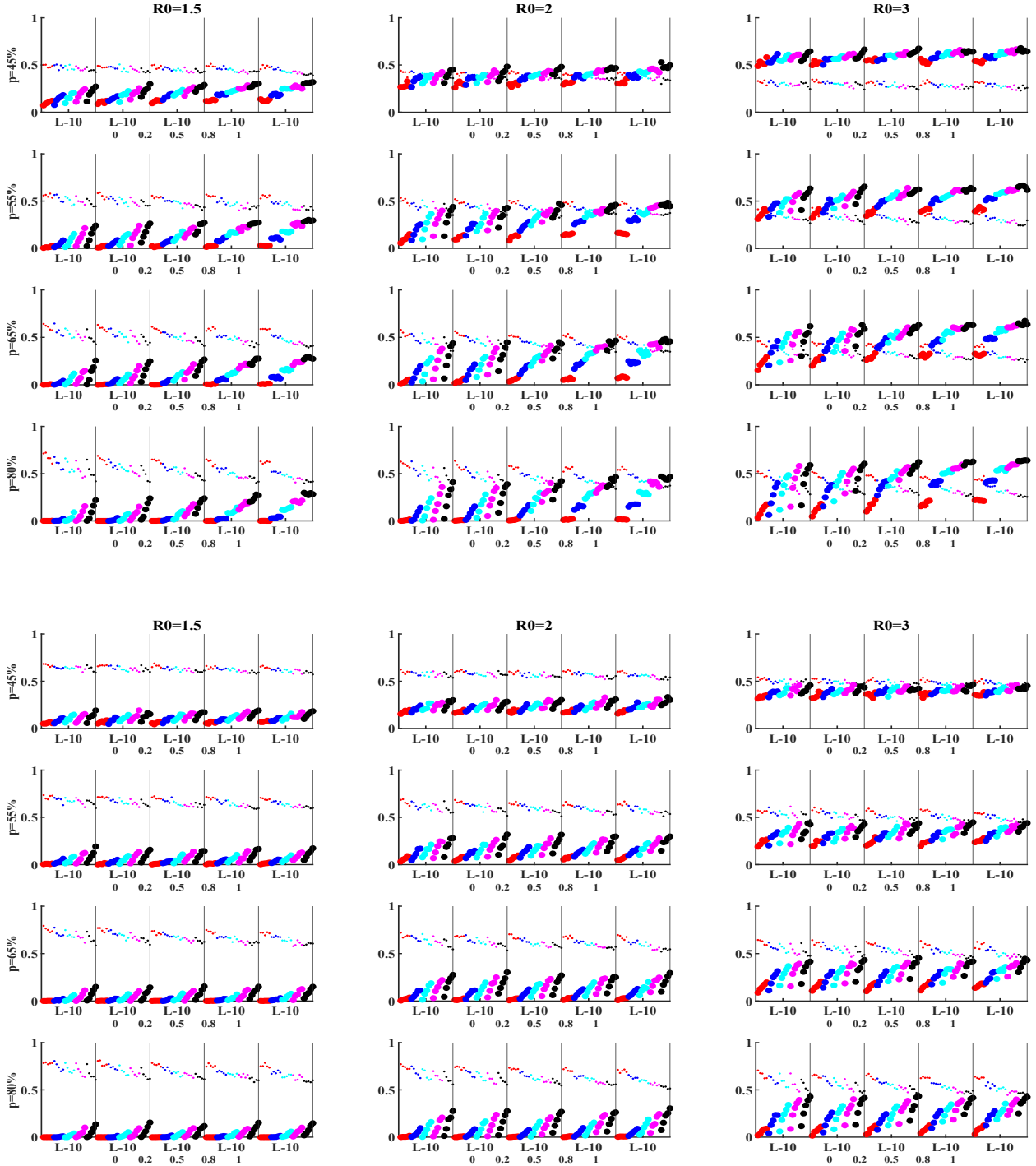

Figure 4.3: Probability of zero (dots) or $>$ 50 (stars) new infections $(I + I_w)$ when $\mathcal{R}_0 = 1.5, 2, \text{or } 3$, $p = 0.35, 0.55, 0.65, \text{or } 0.75)$, $\boldsymbol{\gamma_w} = \boldsymbol{(\gamma, 5\gamma)}$ $\mathbf{yrs}^{-1}$ (top, bottom), $\gamma = \frac{52}{0.5}$, $G = 1$, $\nu = 1$, $(1 - q) = (0, 0.2, 0.5, 0.8, 1)$, $p_1 = p_2 = 0$, $k_1 = k_2 =$ [1/300 (defined by L), 1/100, 1/50, 1/25, 1/10], and $\boldsymbol{k_3 = k_4 = 0}$. The symbols within each colour correspond to the probabilities as k_2 increases. The colour changes as k_1 increases. $(1 - q)$ increases for each subplot within each panel.

Figures 4.3 to 4.6 show the probability that an infectious individual initially does not produce infection afterward (dots) and the probability that more than 50 secondary cases occur (stars) for $R_0 = 1.5, 2,$ or 3, vaccination coverage $p = 0.45, 0.55, 0.65,$ or 0.80, immunity-waning rates $k_3, k_4 \in [0, 0.4]$, and influenza-specific infectious period values $\gamma_w = \gamma * (1, 3, 5)$. Our results indicate that the probability of no outbreak ranges from very low ($< 5\%$) to as high as 80%, depending strongly on the level of pre-existing immunity and the speed at which recovered immune protection is lost. Higher vaccination coverage substantially increases the chance of outbreak extinction, whereas higher waning rates (k_3, k_4) reduce it, producing more frequent outbreaks and greater epidemic growth. Increasing R_0 from 1.5 to 3 similarly reduces the probability of extinction, highlighting that the intensity of influenza transmission critically shapes the risk of outbreak. Loss of natural immunity plays a major role, allowing influenza outbreaks to re-emerge even when initial vaccination levels are moderate.

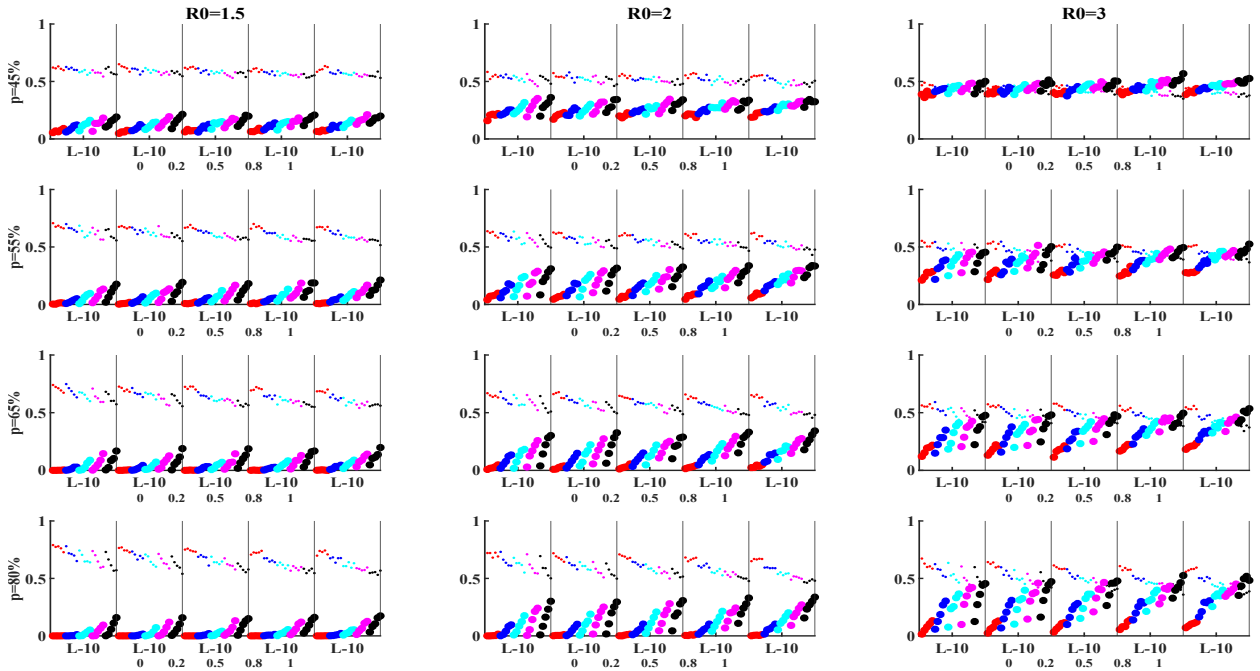

Figure 4.4: Probability of zero (dots) or > 50 (stars) new infections $(I + I_w)$ when $\mathcal{R}_0 = 1.5, 2,$ or 3), $p = 0.35, 0.55, 0.65,$ or 0.75), $\boldsymbol{\gamma_w = 3\gamma}$ **yrs**$^{-1}$, $\gamma = \frac{52}{0.5}$, $G = 1$, $\nu = 1$, $(1 - q) = (0, 0.2, 0.5, 0.8, 1)$, $p_1 = p_2 = 0$, $k_1 = k_2 = [1/300$ (defined by L), $1/100, 1/50, 1/25, 1/10]$, and $\boldsymbol{k_3 = k_4 = 0}$. The symbols within each colour correspond to the probabilities as k_2 increases. The colour changes as k_1 increases. $(1 - q)$ increases for each subplot within each panel.

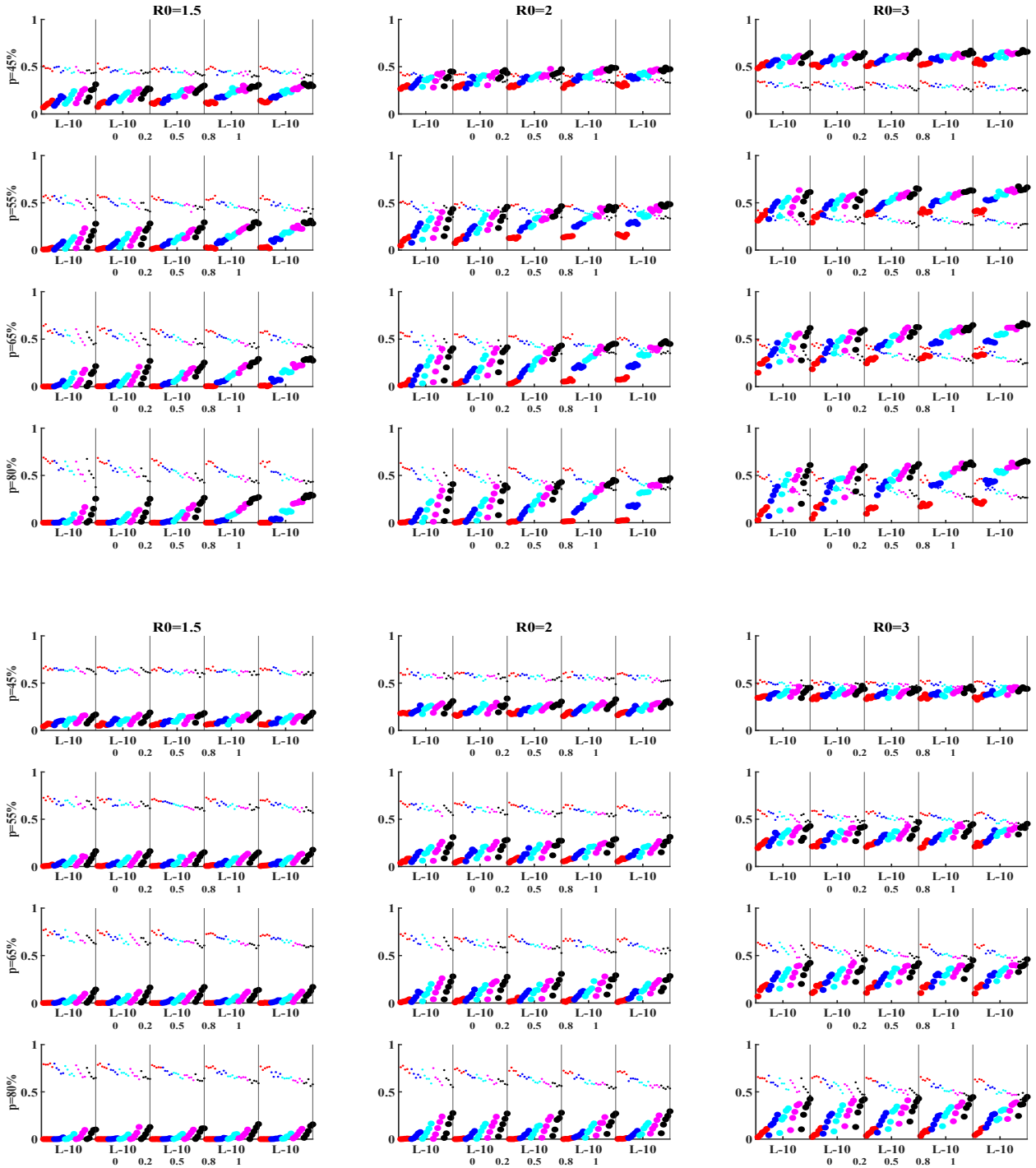

Figure 4.5: Probability of zero (dots) or > 50 (stars) new infections $(I + I_w)$ when $\mathcal{R}_0 = 1.5, 2,$ or 3, $p = 0.35, 0.55, 0.65,$ or 0.75, $\boldsymbol{\gamma_w = (\gamma, 5\gamma)}$ $\mathbf{yrs}^{-1}$, $G = 1$, $\nu = 1$, $(1 - q) = (0, 0.2, 0.5, 0.8, 1)$, $p_1 = p_2 = 0$, $k_1 = k_2 = [1/300$ (defined by L), $1/100, 1/50, 1/25, 1/10]$, and $\boldsymbol{k_3 = k_4 = 0.4}$. The symbols within each colour correspond to the probabilities as k_2 increases. The colour changes as k_1 increases. $(1 - q)$ increases for each subplot within each panel.

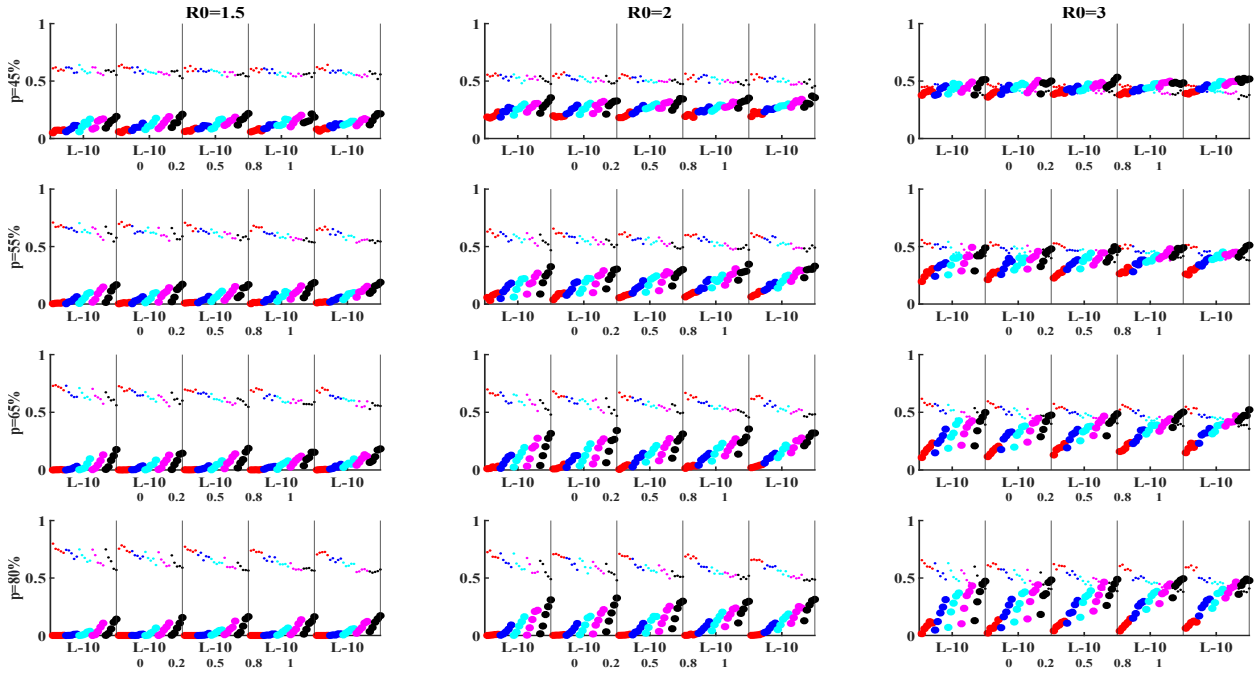

Figure 4.6: Probability of zero (dots) or $>$ 50 (stars) new infections ($I + I_w$) when $\mathcal{R}_0 = 1.5, 2,$ or 3, $p = 0.35, 0.55, 0.65,$ or 0.75, $\boldsymbol{\gamma_w = 3\gamma}$ **yrs**$^{-1}$, $G = 1$, $\nu = 1$, $(1-q) = (0, 0.2, 0.5, 0.8, 1)$, $p_1 = p_2 = 0$, $k_1 = k_2 = [1/300$ (defined by L), $1/100, 1/50, 1/25, 1/10]$, and $\boldsymbol{k_3 = k_4 = 0.4}$. The symbols within each colour correspond to the probabilities as k_2 increases. The colour changes as k_1 increases. $(1-q)$ increases for each subplot within each panel.

4.4 Discussion

In this chapter, we develop and analyze a compartmental model of seasonal influenza that explicitly incorporates waning immunity following both vaccination and natural infection. Unlike classical SEIR or SEIRS models that assume a single recovered class, our framework distinguishes between fully susceptible individuals (S), vaccinated individuals (V), individuals with waning immunity (W), primary infections (I), secondary infections (I_w), and two recovered classes (R and R_w). This structure allows the model to capture the biological reality that influenza immunity is temporary and that individuals may experience repeated infections over successive seasons.

A key contribution of this chapter is the derivation of analytical expressions that link the seasonal immunity structure to the outbreak risk. We obtained explicit expressions for the disease-free equilibrium and the control reproduction number R_c, demonstrating that R_c depends not only on the classical transmission parameter β but also on the distribution of individuals between the susceptible (S_0) and the waning (W_0) classes at the beginning of the influenza season. This result reflects an important biological insight: influenza outbreaks are shaped by memory of the immune system carried over from previous seasons.

We further derived an explicit quadratic expression for the critical vaccination threshold p_c required to ensure $R_c < 1$. Unlike diseases with lifelong immunity, the influenza vaccination threshold must account for fully susceptible and partially immune individuals. This finding highlights that vaccination policies targeting only the susceptible class may be insufficient when immunity decays rapidly.

To quantify the magnitude of the epidemic, we derived a final size relation that incorporates both primary and secondary infections. By introducing a short pre-wave reallocation window, we linked effective susceptible stocks (S_0, W_0) at the start of a season to immunity levels from the previous season. This seasonal mapping provides a mechanistic explanation for influenza recurrence: even moderate waning of natural or vaccine-induced immunity can replenish the susceptible pool sufficiently to permit epidemic growth.

Our sensitivity analysis identified the transmission rate β as the dominant parameter influencing both the peak levels of infection and the total size of the epidemic. Although vaccination rates (p_1, p_2) reduce the magnitude of the outbreak, their effect is weakened when immunity wanes rapidly (large k_1, k_2, k_3, k_4). In particular, loss of natural immunity (k_3, k_4) significantly increases the probability of persistence of outbreaks, strengthening the biological understanding that influenza differs fundamentally from infections such as measles, where post-infection immunity is long-lasting.

Stochastic simulations using a branching-process approximation further demonstrated

that the probability of an outbreak varies widely depending on the structure of preseason immunity. Higher vaccination coverage and slower waning rates increased the probability that a single imported case would die out, whereas larger R_0 values and faster immunity decay substantially increased the probability of the outbreak. These results emphasize that sustained immunity, in addition to vaccination coverage, is central to influenza control.

Several limitations of the model suggest directions for future research. First, the current framework assumes that vaccinated individuals (V) are fully protected from infection. Biologically, the effectiveness of the influenza vaccine is imperfect and time-dependent. A more realistic formulation would allow breakthrough infections among vaccinated individuals and incorporate time-varying vaccine efficacy. Second, the age structure could be incorporated to capture heterogeneous contact patterns and age-specific immune responses. Third, the assumption of homogeneous mixing could be replaced by structured contact networks or household transmission models. Finally, coupling this framework with antigenic evolution models would provide more insight into how viral drift interacts with waning immunity to shape long-term epidemic patterns.

In general, this chapter demonstrates that the seasonal influenza dynamics is governed not only by transmission intensity but also by the redistribution of immunity between seasons. Waning immunity plays a central role in replenishing the susceptible pool and enabling recurrent outbreaks. These findings provide a quantitative basis for understanding why influenza persists annually and underscore the importance of strategies that improve both the coverage of vaccination and the durability of immune protection.

Chapter 5

Disease Dynamics in Theme Park

Part A has been submitted for publication

Part A: Deterministic model of COVID-19, influenza, measles and norovirus transmission in a theme-park

5.1 Introduction

COVID-19, influenza, measles, and norovirus can be transmitted directly from human to human and have the potential to be indirectly transmitted through a contaminated environment [182, 183, 184, 185] (virus particles can survive on surfaces for several hours to days with varied time duration [186]).

Amusement parks attract large numbers of visitors from all over the world. Approximately 21 and 19 million people visited Walt Disney World's Magic Kingdom and Disneyland, respectively, in 2019 [187]. Even during the COVID-19 pandemic, these parks attracted over 6 and 3 million visitors in 2020 [187]. Given the expected large number of visitors to amusement parks, it is necessary to implement safety measures to mitigate the spread of

infectious diseases. Such mitigation strategies can involve: limiting the number of guests each day, increasing cleaning and sanitization services, recommending or mandating mask wearing for visitors and/or staff, recommending or mandating the use of other personal protective equipment (PPE), temperature checks for visitors and workers upon gate entry, and regular hand sanitization routines [186, 188, 189, 190, 191, 192, 193].

Mathematical models of pathogen spread have highlighted the importance of adopting social distancing measures to reduce human-to-human contact. For examples, see [194, 195, 196, 197, 198, 199]. Models of environmental contamination control have also been studied. Considering an indirect mode of transmission only, Xie et al., examined the importance of adopting frequent sanitization routines to reduce transmission via contaminated surfaces [200]. Using a hybrid multi-scale model including direct and indirect transmission, Bounchinta et al. showed that infected surfaces can play a crucial role in disease transmission [201]. We extend the study of direct and indirect transmission to a theme park setting where both transmission routes will affect virus spread. In the following, we quantify the effects of environmental sanitization in reducing indirect transmission. We also quantify the effects of social distancing and PPE adherence rates in reducing direct transmission of the virus. A multi-patch model is employed to capture transmission outcomes in two different areas of the park. Both areas include a queue and a ride environment.

5.2 Methods

5.2.1 Model formulation and assumptions

A model flow diagram is presented in Figure 5.1 (see Figure 6.1 in this Chapter's Appendix for a more detailed diagram and model description). Briefly, we consider a multi-patch infectious disease modelling framework with n patches. Within each patch i, there are worker and visitor populations that are further delineated by disease status: susceptible S_i^k, exposed

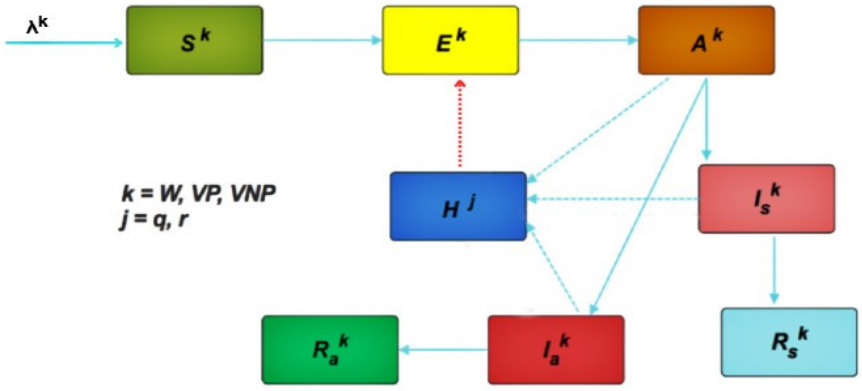

Figure 5.1: Flow diagram

E_i^k, pre-symptomatic infectious A_i^k, asymptomatic infectious $I_{a,i}^k$, symptomatic infectious $I_{s,i}^k$ and immune R_i^k (from infection, or vaccinated), where $k = V, W$ denotes the worker W and visitor V populations. The visitor population is further split into PPE compliant (VP) and non-compliant (VNP) groups. We assume that all workers are PPE compliant as this would be part of their job duties. Within each patch, the model includes environmental reservoirs H_m to consider ride ($m = r$) and queuing ($m = q$) locations where direct (human-human) and indirect (environment-human) transmission can occur.

When individuals present at the park gate, they are first assigned to worker (W), visitor PPE compliant (VP), and visitor PPE non-compliant (VNP) populations. Individuals are then assigned a disease status, which depends on the disease prevalence in the surrounding community, including that of the visiting tourist population. If an individual can enter the park, that is, they are not showing symptoms (and perhaps during an outbreak, pass any diagnostic test at the park gate like a temperature check), the individual is assigned to a home patch i within the park, with a certain probability. Depending on the home patch and whether they are a worker or a visitor, the individual is assigned a proportion of time spent in each of the n patches.

The mathematical model tracks human-human and environment-human pathogen transmission, and pathogen shedding into the environment from infected individuals. It thus tracks the changing infection/disease landscape of all visitors, workers, and environmental reservoirs in the park. We note that some individuals may enter the park while asymptomatically infectious. If these individuals progress to symptomatic disease we assume they quickly exit the park, minimizing transmission capability.

The model incorporates periodic cleaning of the rides and queues throughout the day. When cleaning occurs, we assume that the pathogen load in these environmental reservoirs is set to zero. Additionally, we assume that the park closes at the end of the day and is cleaned so that there is no pathogen load the next morning at opening time.

For ease of mathematical analysis, we consider a variant of the full model with two patches.

5.2.2 Model Parameters

We consider a total daily visitor population of $20,000$ and a total daily worker population of 200, similar to that experienced when theme parks were re-opened during the COVID-19 pandemic [187]. We assume that 5% of the visitors/workers entering the park are asymptomatically infected, but this proportion can vary and can be informed by the prevalence of a particular infectious disease in the community.

We assume that the theme park is open for 12 hours per day. It is assumed that workers work in one area of the park and spend all of their time in that area of the park only. We do not consider transit time to their work location via other areas to be of any significance for disease exposure. Visitors are assigned a home patch where they spend most of their day, but they are assigned a fraction of their day within which they spend in other parts of the park. In general, more popular areas of a theme park will attract more visitors. Additionally, visitors may be more likely to spend longer periods in the more popular locations. These

times, and the attraction wait and ride times are informed by [202].

The mathematical model is parameterized for COVID-19, measles, influenza, and norovirus. Disease-specific parameter values are discussed and listed in the Appendix. For all infections, we assume that new symptomatic infections (when A transitions to I) quickly exit the park. The exit rate is given by $\gamma_2 = 1/2$ hour^{-1}.

When entering the park, visitors are assigned a PPE compliance status. This is given by vp_{size} and varies between zero and unity.

Infection can be transmitted via human-human transmission. The infection rate is determined by disease specific parameters (see Table 6.2, the contract rates between visitors and workers, and the efficacy of PPE in reducing the probability of transmission (related to parameters s_h, π^{NP}, π^{P} and π^{PNP}). Here, we assume average contact rates between visitors (c^V) to be 5 or 10, between workers (c^W) to be 2, and between workers and visitors (c^{WV}) to be 4 [203].

Infection can also be transmitted to humans through contaminated environments in the ride or queue areas of the park. These infection rates are determined by the infection transmission rates from rides and queues to humans with and without PPE protection (related to parameters f, β_r^{HNP}, β_q^{HNP}, β_r^{HP}, and β_q^{NP}).

5.2.3 Basic reproduction number

The transmission of an infection is related to the basic reproduction number, $\mathcal{R}_0$; the number of secondary cases that an infected individual generates when introduced into a totally susceptible population, without any public health controls. Reported estimates of the reproduction number for COVID-19 range from 2-6 [204, 205] for the wild-type strain, but as high as $5.5 - 24$ for the Omicron variant [206]. The reproduction numbers for measles, seasonal influenza, and norovirus are reported to be $12 - 18$ [154, 182], $1 - 2$ [207], and $1.2 - 7.2$ [40], respectively. We explored values of model parameters π^{NP} (the probability of

generating a new infection given a contact between unprotected individuals, i.e., no PPE) and κ (pathogen shedding rate) that produce similar and realistic $\mathcal{R}_0$ estimates of COVID-19, measles, influenza and norovirus given different contact rates between workers, visitors, and workers and visitors, c^W, c^V, and c^{WV}, respectively (5 or 10 contacts are used from [203], on average). We note that base values π^{NP} and κ are chosen so that the ranges of $\mathcal{R}_0$ for each pathogen align with the literature on that disease. These values are also free parameters that can be used to inform public health policies within the park.

The Next Generation Matrix method [208, 24, 209, 136] is employed to derive the basic reproduction number. Given the complexity of the model, an analytical expression of $\mathcal{R}_0$ is not feasible, hence it is evaluated numerically.

5.2.4 Sensitivity Analysis

A sensitivity analysis using Latin Hypercube Sampling/ Partial Rank Correlation Coefficient (LHS/PRCC) method [119, 120] is used to study the effects of parameter variability on the total number of newly made asymptomatic infections in one day of park operations (12 hours). We vary the: effectiveness of PPE in halting human-human transmission (s_h); effectiveness of PPE in halting transmission from the environment (f); proportion of visitors wearing PPE correctly (vp_{size}); number of infected individuals entering the park (i_{ap}); shedding rate of the pathogen into the environment (κ); contact rates between workers and visitors (c^v, c^w, c^{wv}); probability of generating new infections in the park between unprotected individuals (π^{NP}) under different cleaning policies: cleaning once a day before opening, and cleaning multiple times throughout the day. For each scenario, we generate 3000 samples, and the monotonic relationship between model parameters and outputs is verified. Model parameters are varied using uniform distributions. The upper and lower bound values are shown in Table S1.

PRCC values are reported from the LHS/PRCC analysis. These values lie within the range of -1 to 1. The sign of the PRCC value provides a measure of the nature of the linear

association (correlation) between the parameter and the model outcome being measured. The magnitude of the PRCC value then provides a measure of the strength of this linear association. A relation between model output and a given parameter value is considered significant if the magnitude of the PRCC value is greater than 0.5 [210, 119, 120].

5.3 Results

5.3.1 Basic reproduction number ($\mathcal{R}_0$)

Fig. 5.2 displays the contour plots of $\mathcal{R}_0$ over parameter space $\pi^{NP} - \kappa$, given the average contacts between visitors to be 5 or 10, between workers to be 2, and between workers and visitors to be 4 [203]. We note that $f = s_h = 0$ here, as the basic reproduction number is estimated when public health control mechanisms are not in place. Intuitively, as κ and π^{NP} increase, $\mathcal{R}_0$ increases. $\mathcal{R}_0$ values that lie in realistic ranges, between 2-6 [204, 205] for COVID-19, 1-2 [207] for influenza, 12-18 [154, 182] for measles, 1.2-7.2 [40] for norovirus, are indicated with dot markers on the relevant contours. Herewithin, we take values of κ and π^{NP} in these ranges.

5.3.2 Numerical Simulations

Theme park disease spread intervention strategies should be implemented so that the transmission probability is decreased. Thus, reducing the number of secondary infections (A) produced over one day is of interest. Here, we compare the number of secondary infections (A) generated during the open hours of the park while varying the proportion of infected visitors or workers entering the park (i_{ap}), the proportion of visitors correctly wearing PPE (vp_{size}), and the effectiveness of the PPE (f, s_h). We also compare model dynamics when cleaning occurs every 2, 3, 4, and 6 hours versus only overnight (once a day).

Figures 5.3 - 5.6 plot the incidence of new A infections over the course of the opening

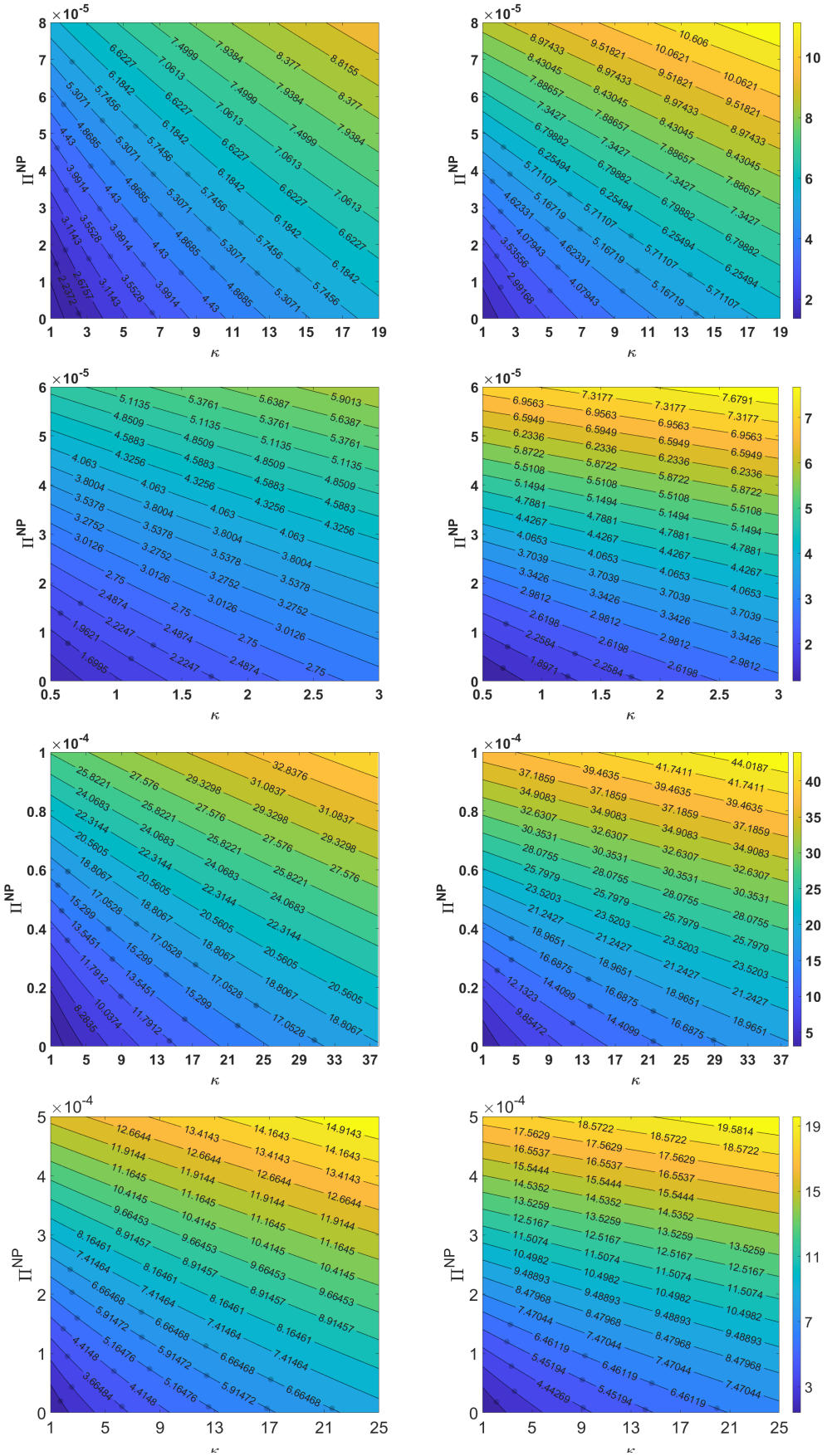

Figure 5.2: Contour-plots of the basic reproduction number $\mathcal{R}_0$ in $\pi^{NP} - \kappa$ parameter space given contacts of (left) 5 or (right) 10 between visitors, 2 between workers, and 4 between workers and visitors for COVID-19 (top row), influenza (2nd row), measles (3rd row) and norovirus (bottom row). Here, $f = s_h = 0$.

hours of the theme park for COVID-19, influenza, measles, and norovirus, respectively, when $f = 0.1$, $s_h = 0.1$, $\mathrm{i}_{ap} = 0.05$, $vp_{size} = 0.1$, 0.5, 0.9 (left, middle, right panels) and the theme-park is cleaned every 2 (black lines), 3 (red lines), 4 (cyan lines) or 6 (magenta lines) hours or once a day (green lines). We note that the top, middle and bottom rows of Figures 5.3 - 5.6 show outcomes when infected individuals are seeded into the visitor population that is not wearing PPE (top), the visitor population that is wearing PPE (middle), and when infected individuals are distributed between the two visitor populations these two classes and the worker population (bottom). In all cases, 5% of the total population is seeded as infected.

Figures 5.3 - 5.6 show that reductions in A are experienced as PPE compliance increases (comparing left, middle and right columns). However, we observe that increased cleaning rates (from green to black lines) have the greatest effect in reducing the number of secondary infections for each disease. The costs of cleaning versus the provision and enforcement of PPE compliance must therefore be considered by all theme parks.

Figure 5.7 plots the percent efficacy of cleaning every 2, 3, 4, and 6 hours compared to a once-a-day cleaning scenario as baseline, considering different visitor population proportions that are wearing PPE correctly ($vp_{size} = 0.1$, 0.5, and 0.9, left to right columns) for all four diseases (top to bottom rows). Figure 5.7 supports our observation that heightened cleaning frequency can effectively reduce the incidence of secondary infections across all four diseases in the theme park. It also shows that increased cleaning frequency results in greater reductions in secondary infection incidence than increases in vp_{size}.

5.3.3 Sensitivity Analysis

Figure 5.8 shows the results of a sensitivity analysis on the basic and control reproduction numbers, $\mathcal{R}_0$ and $\mathcal{R}_c$, for COVID-19, influenza, measles, and norovirus (top to bottom). Evidently, $\mathcal{R}_0$ and $\mathcal{R}_c$ are significantly affected by the shedding rate (κ). Additionally, changes in the effectiveness of PPE against human-environment transmission (f) significantly affect

$\mathcal{R}_c$. These results highlight the importance of reducing the viral load in the environment (i.e., cleaning).

We also studied the impact of cleaning on the cumulative number of new asymptomatic infections over the course of the park day for all viruses. This is considered under low, medium, and high levels of infected individuals entering the park ($i_{ap} = (0.001 - 0.05)$, $(0.05 - 0.1)$, and $(0.1 - 0.5)$). Figures 5.9 - 5.12 show that when cleaning occurs once a day (left column), reductions in the virus shedding rate (κ), and the increase in the effectiveness of the PPE in human-environment transmission (f) as well as the proportion of visitors wearing PPE properly (vp_{size}) are needed to significantly reduce the number of new A infections in the park. When the park is cleaned multiple times a day (right column), to significantly affect the number of new A infections produced in the park, reductions in κ and i_{ap} are still important, as well as an increase in f. However, variations in vp_{size} do not significantly affect the outcome anymore. Instead, the frequency of cleaning cl_{time} becomes important. Here, we see that reductions in the number of hours between cleanings are needed to greatly reduce the number of A infections produced over the course of one park-day.

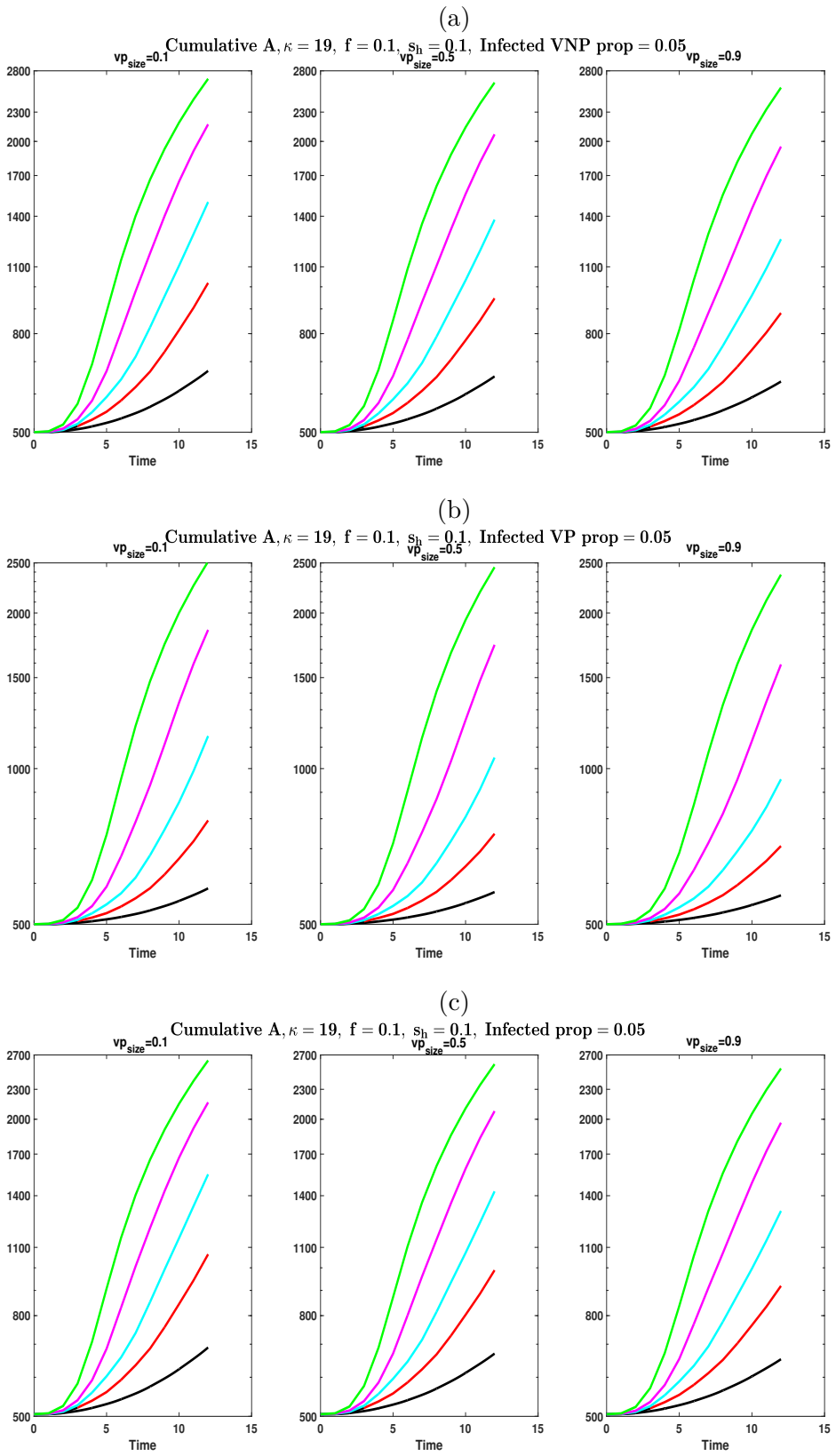

Figure 5.3: Dynamic of A (asymptomatic) classes of **Covid-19** for $f = 0.1$, $s_h = 0.1$, $vp_{size} = 0.1$, 0.5, 0.9 and $i_{ap} = 0.05$ when infected individuals are seeded in the (a) visitors with no PPEs (b) visitors with PPEs and (c) visitors in both PPE classes and a small fraction of workers (10 out of 200 workers). The theme park is cleaned every 2, 3, 4, or 6 hours, or once a day (black, red, cyan, magenta, green, respectively).

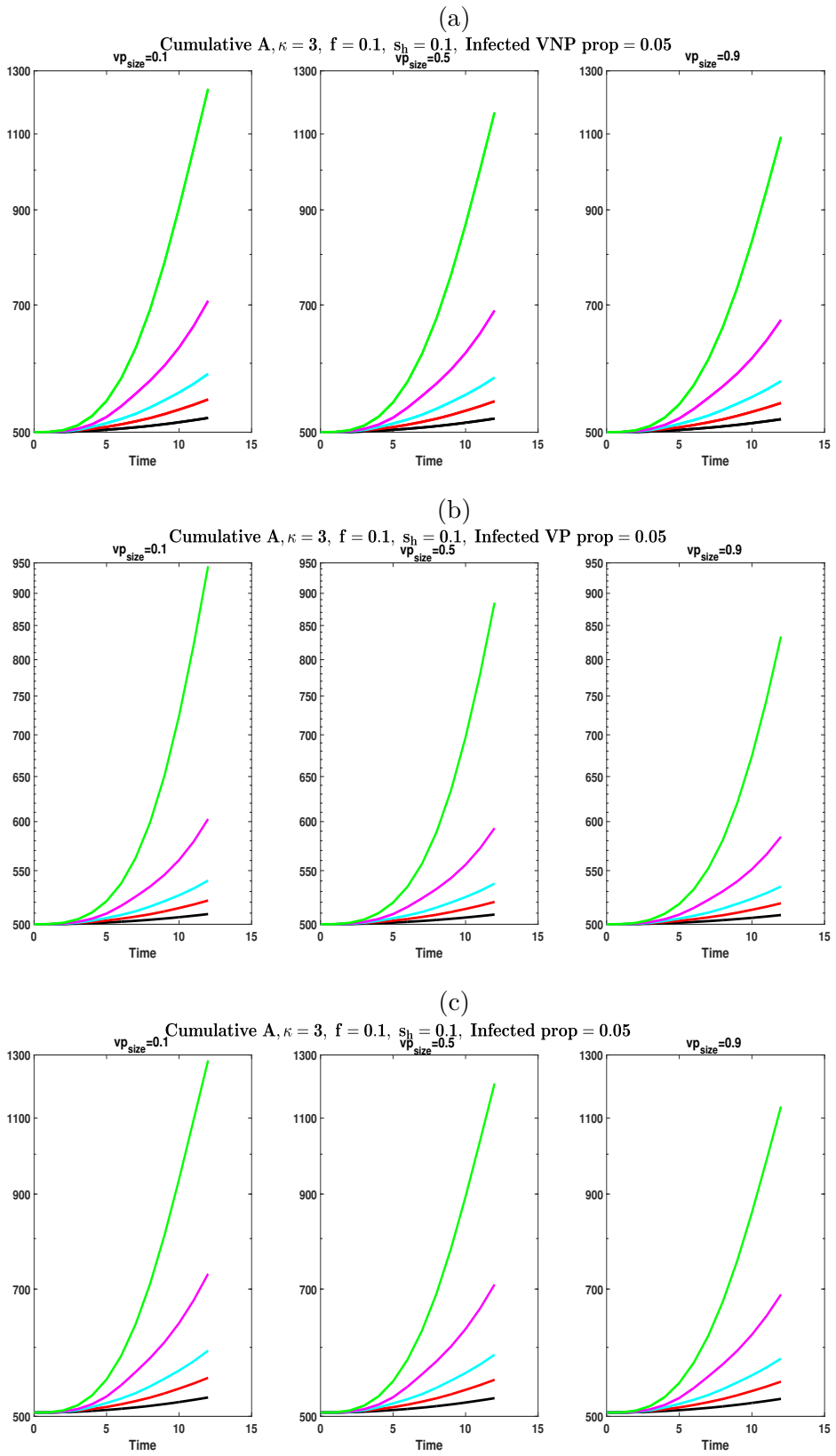

Figure 5.4: Dynamic of A (asymptomatic) classes of **Influenza** for $f = 0.1$, $s_h = 0.1$, $vp_{size} = 0.1$, 0.5, 0.9 and $i_{ap} = 0.05$ when infected individuals are seeded in the (a) visitors with no PPEs (b) visitors with PPEs and (c) visitors in both PPE classes and a small fraction of workers (10 out of 200 workers). The theme park is cleaned every 2, 3, 4, or 6 hours, or once a day (black, red, cyan, magenta, green, respectively).

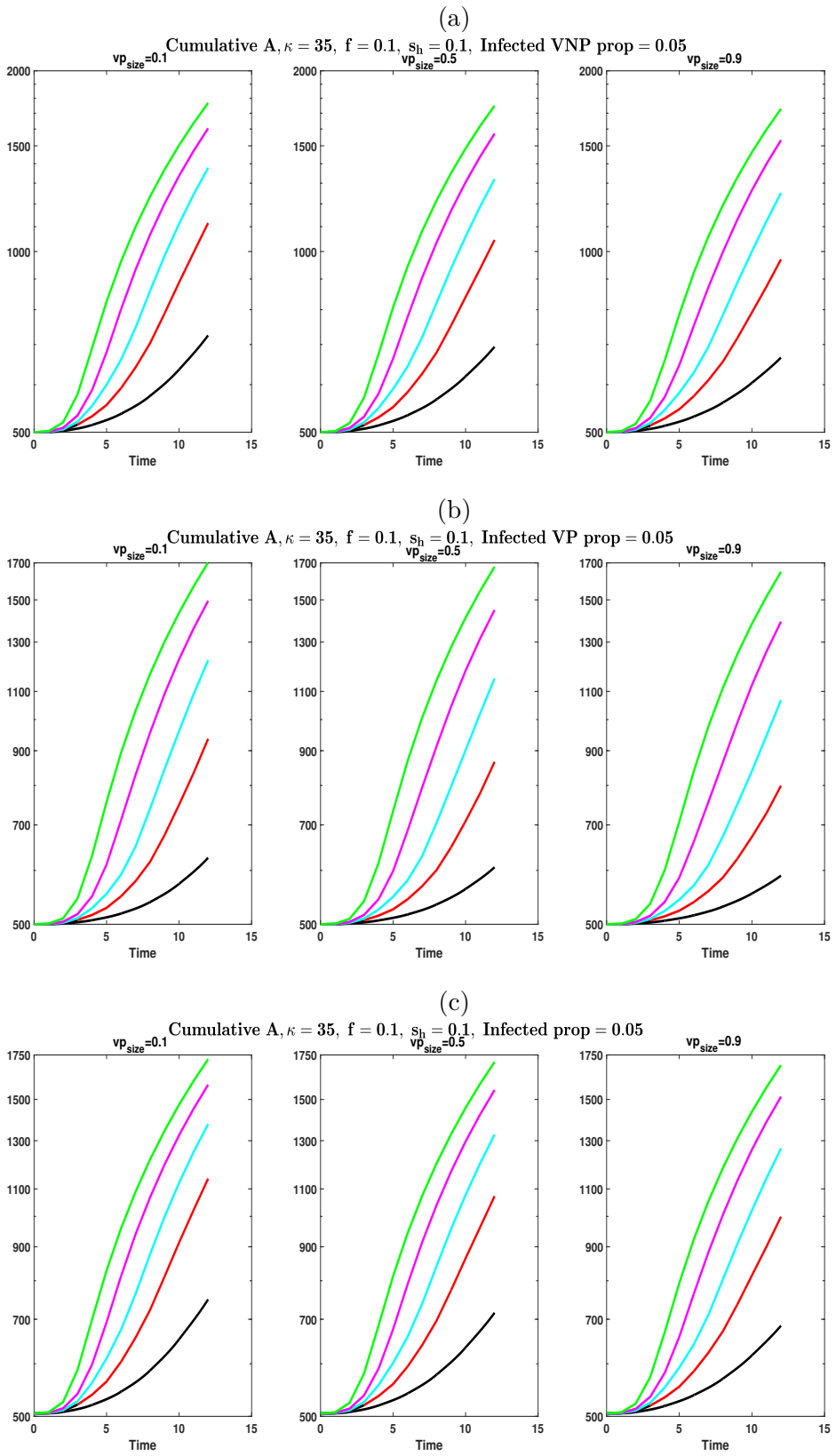

Figure 5.5: Dynamic of A (asymptomatic) classes of **Measles** for $f = 0.1$, $s_h = 0.1$, $vp_{size} = 0.1$, 0.5, 0.9 and $i_{ap} = 0.05$ when infected individuals are seeded in the (a) visitors with no PPEs (b) visitors with PPEs and (c) visitors in both PPE classes and a small fraction of workers (10 out of 200 workers). The theme park is cleaned every 2, 3, 4, or 6 hours, or once a day (black, red, cyan, magenta, green, respectively).

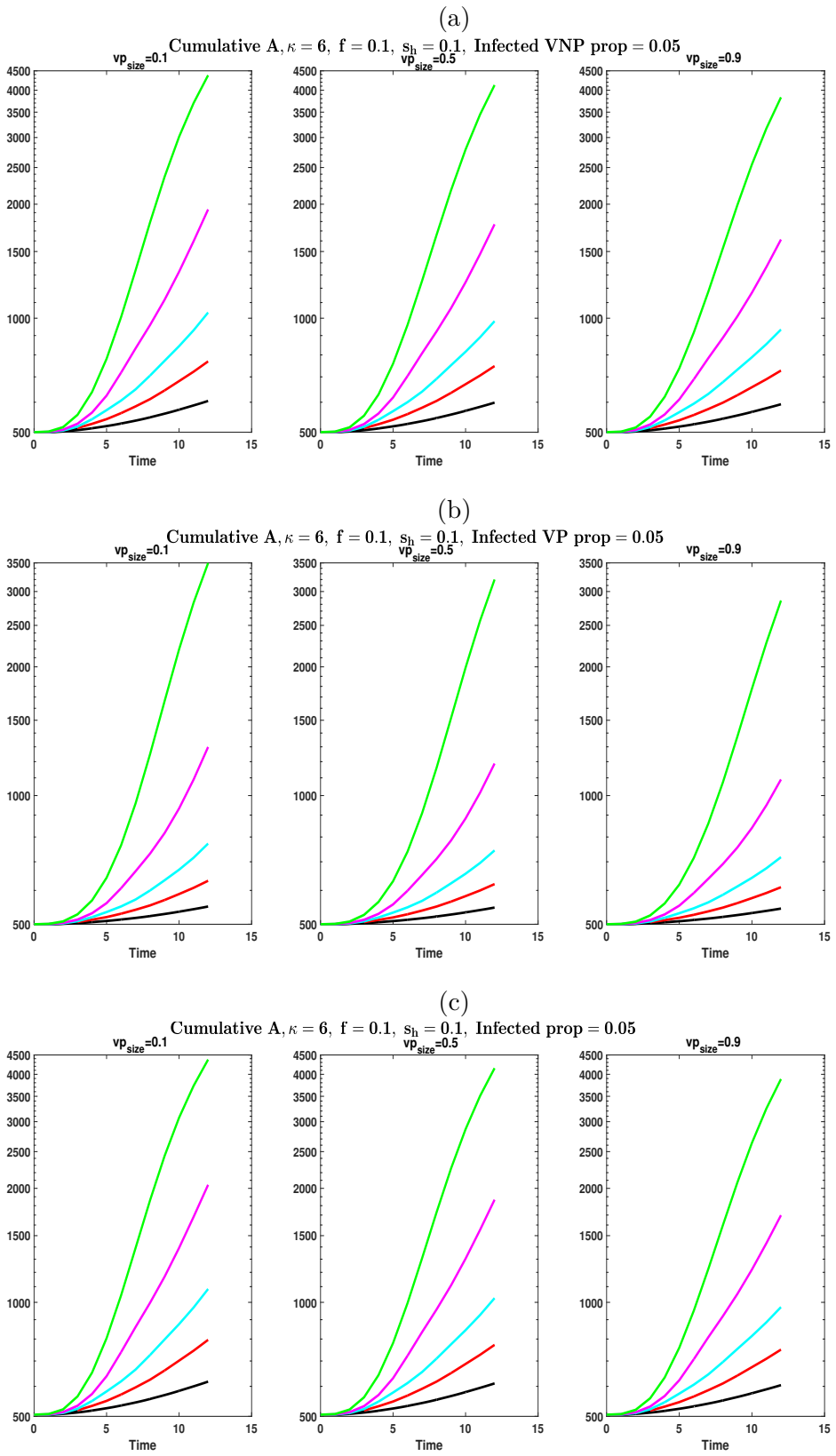

Figure 5.6: Dynamic of A (asymptomatic) classes of **Norovirus** for $f = 0.1$, $s_h = 0.1$, $vp_{size} = 0.1$, 0.5, 0.9 and $i_{ap} = 0.05$ when infected individuals are seeded in the (a) visitors with no PPEs (b) visitors with PPEs and (c) visitors in both PPE classes and a small fraction of workers (10 out of 200 workers). The theme park is cleaned every 2, 3, 4, or 6 hours, or once a day (black, red, cyan, magenta, green, respectively).

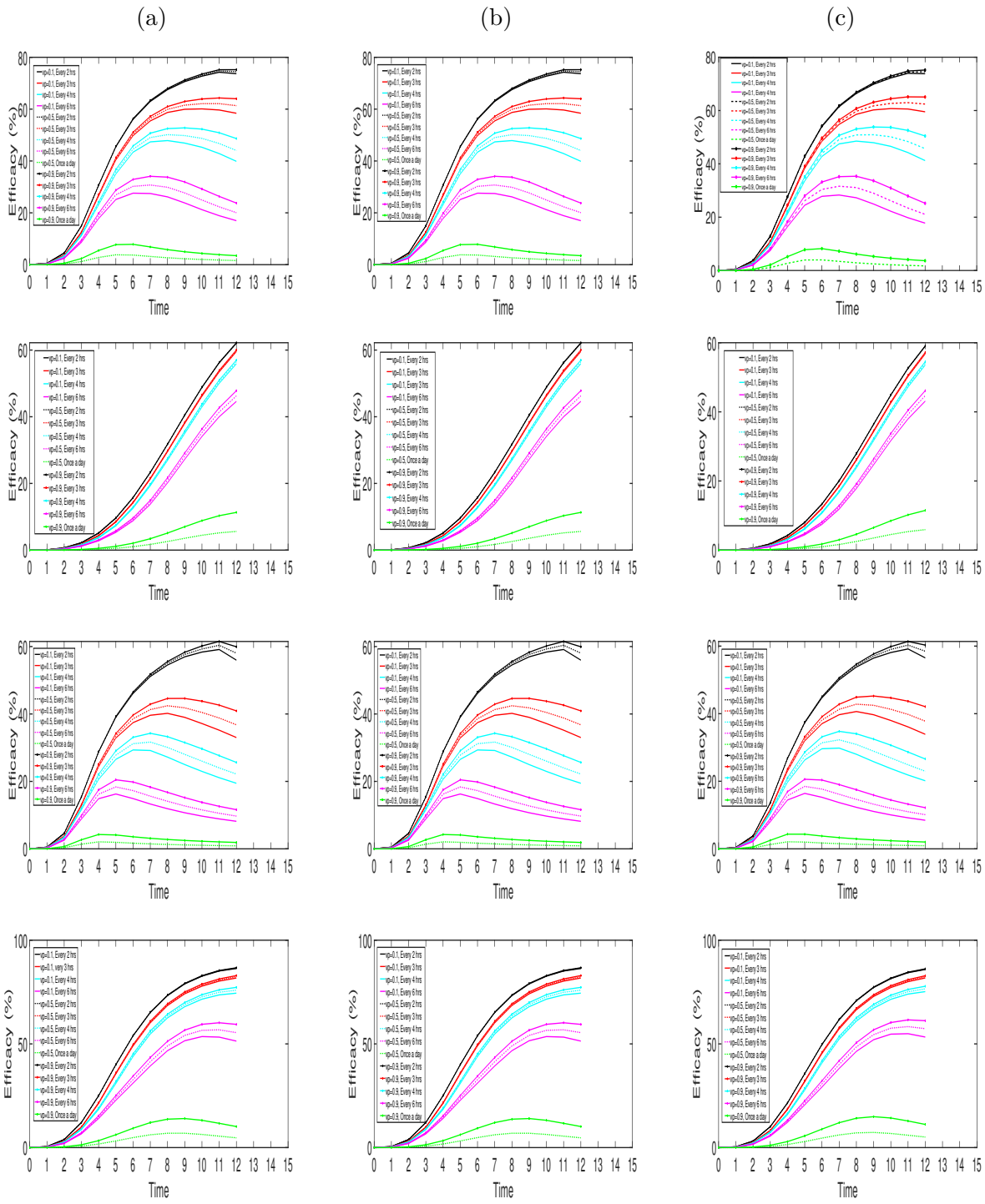

Figure 5.7: Percent change in the number of secondary infections A (asymptomatic) produced for COVID-19, influenza, measles and norovirus compared to no cleaning when $f = 0.1$, $s_h = 0.1$, $i_{ap} = 0.05$, and $vp_{size} = 0.1$, 0.5, 0.9 (solid, dotted, solid with circles). Infected individuals are seeded in the (a) visitors with no PPEs (b) visitors with PPEs and (c) visitors with and without PPEs; also a small fraction of workers (10 out of 200 workers) are included to these three classes. The theme park is cleaned every 2, 3, 4, or 6 hours, or once a day (black, red, cyan, magenta, and green, respectively).

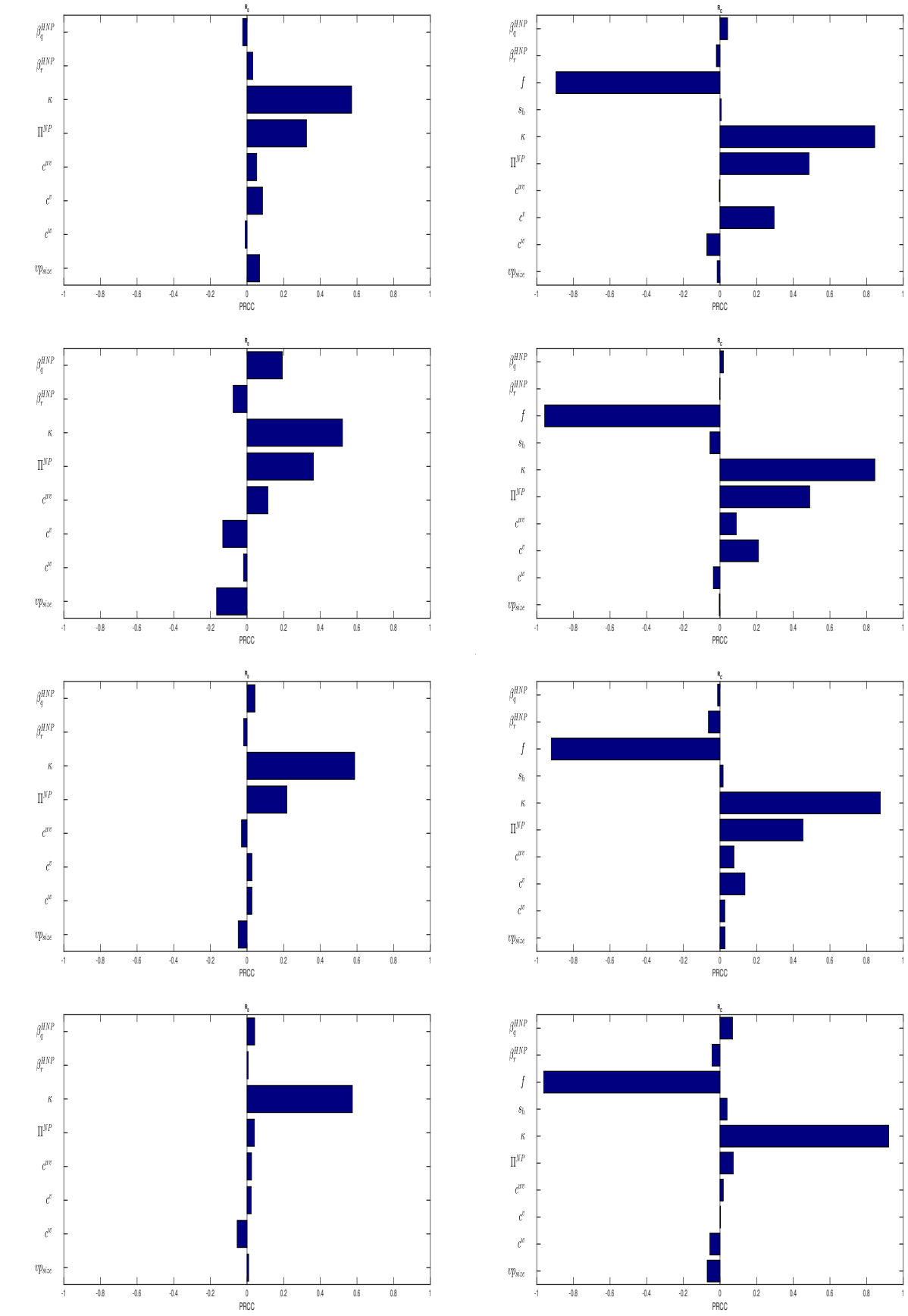

Figure 5.8: PRCC plots of (a) basic reproduction number (left) and (b) control reproduction number (right) for COVID-19, influenza, measles, and norovirus.

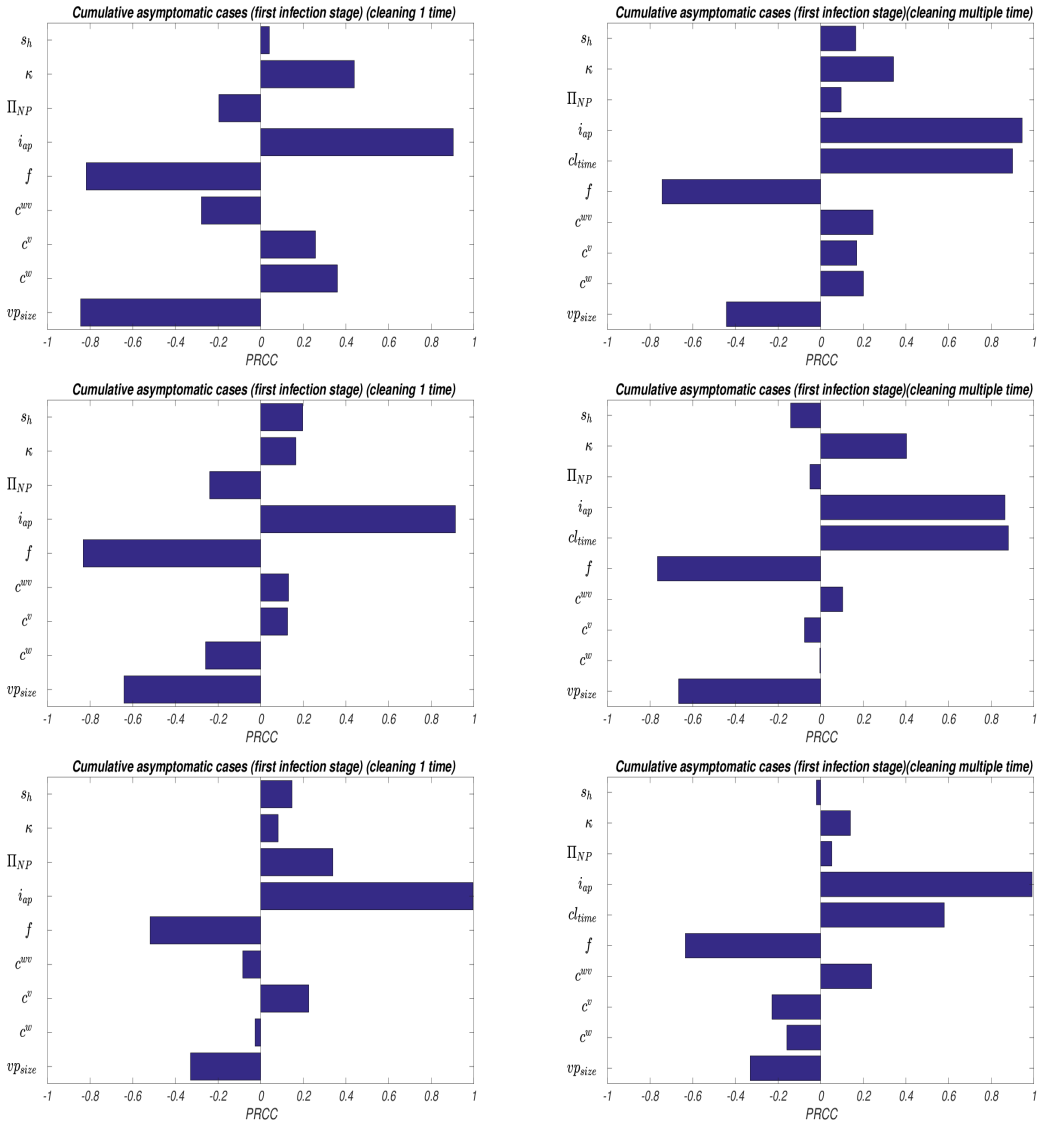

Figure 5.9: PRCC plots on the number of cumulative asymptomatic A of **Covid-19** infections produced over the course of one park day when (left panels) cleaning is once a day, (right panels) cleaning occurs multiple times a day, and when the proportion of infected visitors entering the park is $i_{ap} = (0.001 - 0.05)$ (top), $(0.05 - 0.1)$ (middle), and $(0.1 - 0.5)$ (bottom).

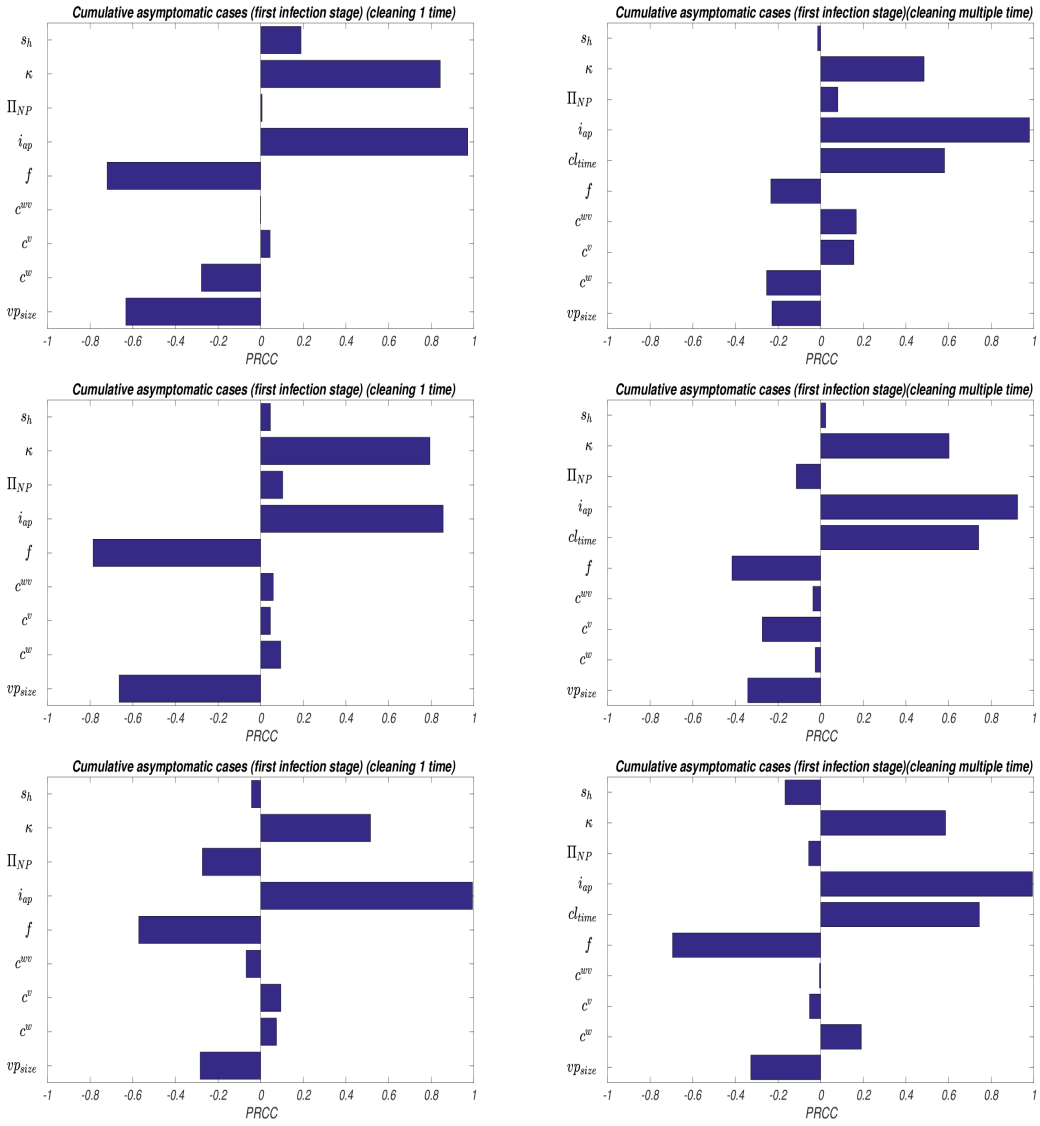

Figure 5.10: PRCC plots on the number of cumulative asymptomatic A of **Influenza** infections produced over the course of one park day when (left panels) cleaning is once a day, (right panels) cleaning occurs multiple times a day, and when the proportion of infected visitors entering the park is $i_{ap} = (0.001 - 0.05)$ (top), $(0.05 - 0.1)$ (middle), and $(0.1 - 0.5)$ (bottom).

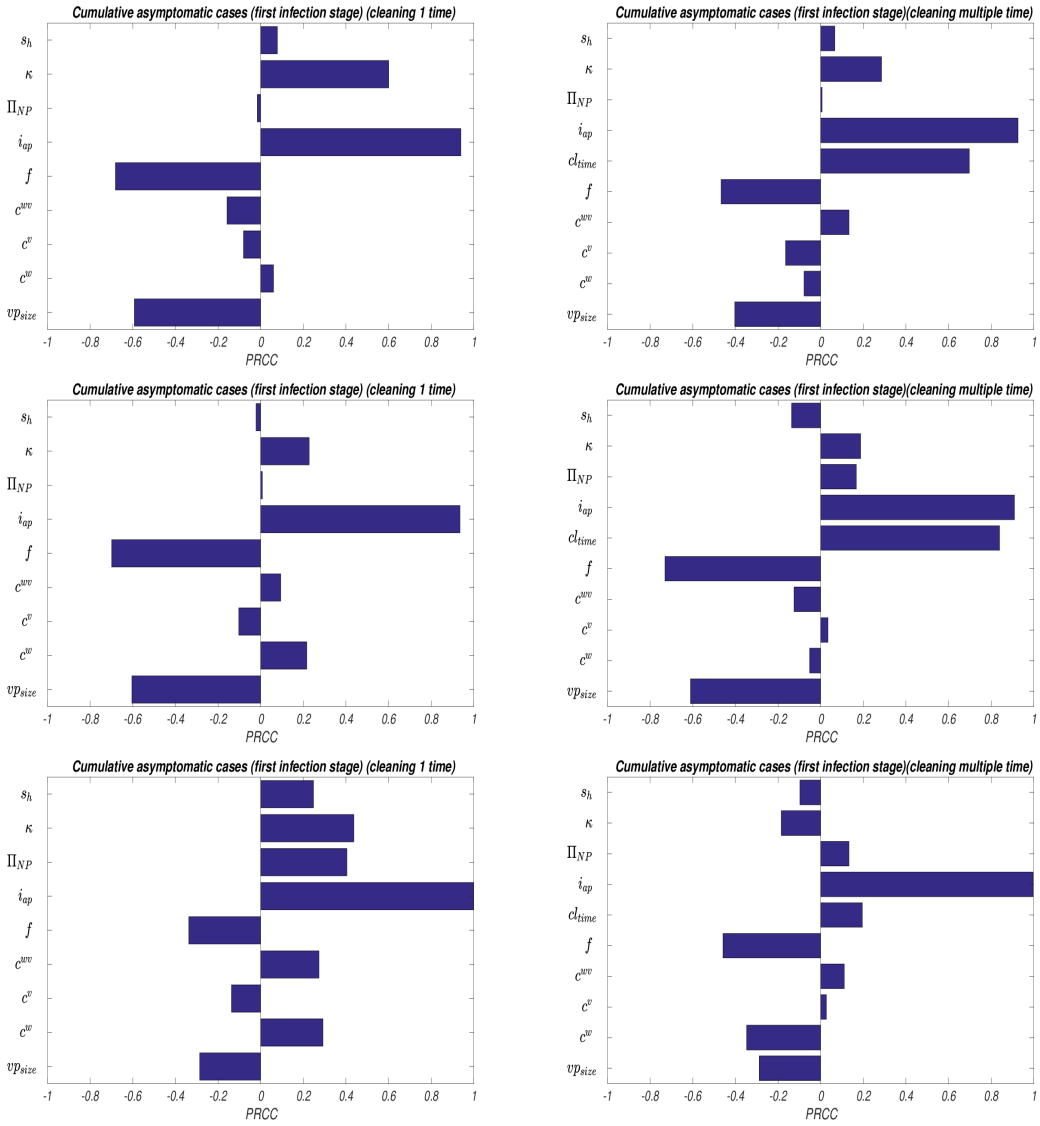

Figure 5.11: PRCC plots on the number of cumulative asymptomatic A of **Measles** infections produced over the course of one park day when (left panels) cleaning is once a day, (right panels) cleaning occurs multiple times a day, and when the proportion of infected visitors entering the park is $i_{ap} = (0.001 - 0.05)$ (top), $0.05 - 0.1$ (middle), and $(0.1 - 0.5)$ (bottom).

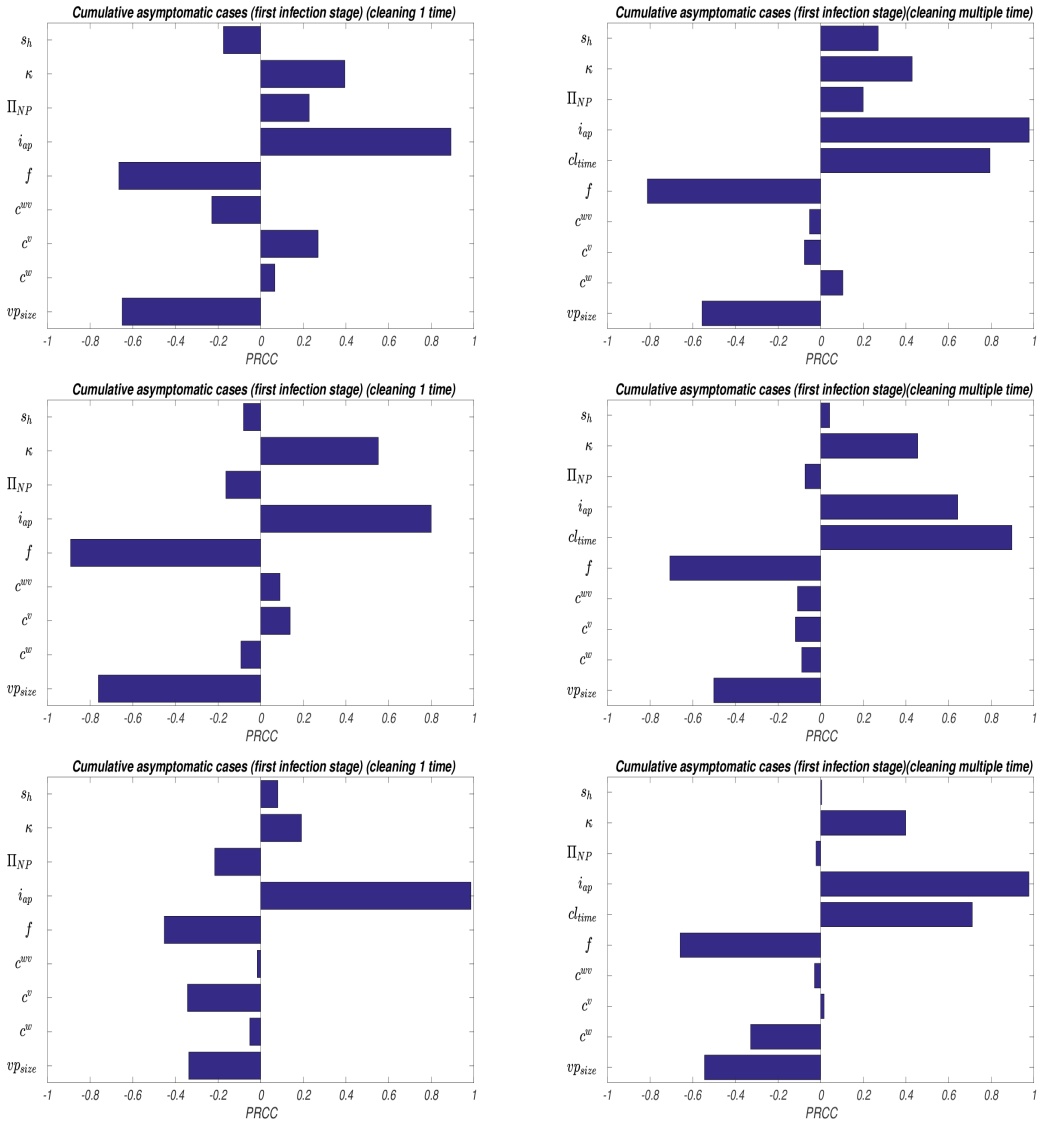

Figure 5.12: PRCC plots on the number of cumulative asymptomatic A of **Norovirus** infections produced over the course of one park day when (left panels) cleaning is once a day, (right panels) cleaning occurs multiple times a day, and when the proportion of infected visitors entering the park is $i_{ap} = (0.001 - 0.05)$ (top), $(0.05 - 0.1)$ (middle), and $(0.1 - 0.5)$ (bottom).

5.4 Conclusion

Theme parks can take action to reduce the spread of infectious diseases within their grounds. We have applied a mathematical model to study the spread of infectious disease (in making secondary infections) given public health measures that theme parks can easily enact i.e., symptom checking at the gate, PPE wearing and hand washing within the park, ride and queue cleaning. We have applied the model to COVID-19, measles, influenza and norovirus, all diseases that have recently affected theme park operations [202, 211, 212].

Our results show that reducing virus shedding to the environment κ, increasing the efficacy of PPE in protecting workers and humans from contracting the virus from the environment f, increasing testing efficacy at the gate to decrease the proportion of infected visitors entering the park i_{ap}, and increasing the proportion of visitors properly wearing PPE (vp_{size}) in the park can greatly reduce transmission of COVID-19, influenza, measles, and norovirus in a theme park. We, however, also find that increases in park cleaning rates greatly affect this outcome, and that, as the proportion of infected visitors entering the park i_{ap} increases, the cleaning rate can grow in importance for disease control. We note, however, that when i_{ap} is low, theme parks can adopt the strategy of cleaning once a day if they ensure adequate use of PPE (face covering and hand sanitization). We remark that as knowledge of vaccine uptake and waning immunity from vaccination and infections is not known by theme parks for all staff and visitors, the wearing of PPE or a sufficient frequence of cleaning rides and queues in the park should be top priorities for a first line of disease transmission defense.

An interesting outcome of our modeling study is that reductions in the number of contacts between workers and visitors were not found to be significant in reducing the number of new infections A in the park. This outcome, however, can be explained when considering specific characteristics of direct human-human and indirect environment-human transmission in the park. During a visit to the park, individuals directly contact individuals over a very short period. Given that the basic reproduction number $\mathcal{R}_0$ of COVID-19 lies in the interval $2-6$

[204, 205], influenza lies in the interval $1-2$ [207], measles lies in the interval $12-18$ [154, 182], norovirus lies in the interval $1.2-7.2$[40], over the lengthy infectious period of respective viruses, the probability of transmitting the virus between humans is small. The shedding rate of the virus to the environment thus lengthens the 'effective infectious period' of an infected individual, increasing the probability of infection of susceptibles. Thus, cleaning rates and mitigation of human-environment contact increase in importance.

The outcomes of this study can guide theme parks in developing public health mitigation strategies in the park. In the current study we have not considered the costs of implementing COVID-19, influenza, measles, and norovirus symptom checking, park cleaning, and any provision of PPE to park workers and visitors, so we cannot comment on optimal policies that minimize transmission while minimizing cost to the park. This is a course for future work.

The current study employs a system of ordinary differential equations. This type of model structure includes broad-sweeping assumptions on the mixing of individuals in the park that ignore spatial aspects of movement, and therefore, may not accurately reflect actual worker and visitor behaviour in the park. Additionally, the existing model ignores different transmission probabilities between indoor and outdoor venues. Next part, we are implementing agent-based models using specific park structures with pathways, queues, and rides that better represent theme-park spatial structure, indoor and outdoor spaces, and movement of the workers and visitors.

Part B: Agent Based Model of Disease Dynamics

5.5 Introduction for ABM

In Part A of this chapter, we examined a model for disease transmission in a theme park that utilized a system of ordinary differential equations (ODEs). Although these systems can be helpful in the analysis of infectious diseases, they have some limitations, including the complexity that arises when introducing more spatial dimensions or multiple areas within the park. Additionally, ODEs do not account for the inherent randomness present in biological systems. We will now investigate the transmission of infectious diseases in a theme park using an agent-based model (ABM). The goals of this section mirror those in Part A, aiming to evaluate the impact of non-pharmaceutical interventions on disease spread within a theme park.

The agent-based model discussed here, developed in Java and executed within Anylogic, is used to represent disease phenomena and simulate the dynamics of infectious disease transmission in a theme park similar to "Canada's Wonderland," located in Ontario, Canada's Greater Toronto Area. We analyze the dynamics of the disease under certain conditions, whether with personal protective equipment (PPE) or without it, along with social distancing, under the baseline assumption of routine surface cleaning. Surface cleaning is treated as

a constant operational assumption and is not varied in the different simulation scenarios; therefore, its independent impact on disease transmission is not evaluated in this research. This study helps to explore potential strategies to safely reopen amusement parks that have been closed due to pandemic outbreaks, similar to the situations experienced during COVID-19. Consequently, we assess how the use of PPE and reduced interactions among visitors can lower viral transmission rates in a theme park environment. Although cleaning and sanitization measures are included to represent realistic park operations, the main emphasis of this research is on behavioural interventions such as the use of PPE and decreased contact among visitors.

Our results support the claims made by references [213, 214] that taking appropriate health precautions, such as wearing PPE, can help reduce the spread of viruses. Furthermore, the use of PPE will decrease the exposure of aerosols to individuals and the surrounding environment.

5.6 Material and Method

5.6.1 Mathematical Model

Similar to our study in Part A, we use the SEIR structure as a conceptual disease-progression framework for the agent-based model (ABM). Transitions between disease states are implemented at the individual level using a state chart (5.15) with probabilistic transmission rules. Control measures including social distancing, personal protective equipment (PPE) usage, and surface cleaning are incorporated into the transmission process.

For reference, the corresponding deterministic SEIR model, which motivates the disease state structure of the ABM, is given by:

$$\frac{dS}{dt} = -\beta IS \tag{5.1}$$

$$\frac{dE}{dt} = \beta IS - \gamma E \tag{5.2}$$

$$\frac{dI}{dt} = \gamma E - \alpha I \tag{5.3}$$

$$\frac{dR}{dt} = \alpha I \tag{5.4}$$

The model represents the dynamic interaction of individuals across four distinct states: S, the number of susceptible individuals; E, the number of exposed individuals; I, the number of actively infected individuals and R, the number of recovered individuals from infection. The population is assumed to be constant with the total size N. Parameters β, γ and α denote, respectively, the baseline disease transmission rate between susceptible and infectious individuals, the incubation rate, and the recovery rate.

In the agent-based model (ABM), the behaviours and interactions of all agents are simulated concurrently. To biologically capture indirect transmission arising from environmental contamination, the baseline infection transmission parameter β is modified to $\beta\,(1 - \text{effi} \cdot \text{PPE})$. Here, β is defined as the product of the contact rate and the probability of effective contact between an infected and a susceptible visitor. The parameter $\text{PPE} \in \{0, 1\}$ represents whether personal protective equipment is used (0 = no PPE, 1 = PPE assumed for all agents in the intervention scenarios), while $\text{effi} \in [0, 1]$ denotes the efficacy of PPE in reducing transmissibility. Personal protective equipment includes face masks and hand sanitization, but could also include face shields, gloves, gowns, and eye protection. The disease incubation period γ is assumed to be $\gamma = \frac{1}{3}\,\text{day}^{-1}$ [207]. In addition, social distancing is implemented through a distance-based contact rule, in which a transmission event can occur only when two agents are within 2 m of each other [215, 216]. This effectively reduces close-contact interactions and is represented by the social distancing factor S_d.

Parameter	Description	Values
γ	latent rate	$1/(3*24*60)$ (min^{-1}) [207]
α	recovery rate	0
S_d	social distancing factor	2m [215, 216]
effi	efficacy of PPE	$0.2, 0.6$ [217, 214]
IT_{pi}	itineraries with entry probabilities ($i = 1, .., 5$)	$(0.1, 0.1, 0.1, 0.3, 0.4)$[Assumed]
κ	environmental contamination input rate (min^{-1})	0.1 (baseline scenario, assumed)
δ	environmental contamination removal rate (min^{-1})	0.1 (baseline cleaning, assumed)
ξ	pathogen shedding input rate by infected visitors (min^{-1})	0.01 (baseline scenario, assumed)
τ_c	surface cleaning period	60 min (baseline operation)

Table 5.1: Parameters for ABM

5.6.2 AnyLogic: An Agent Based Simulation Environment

AnyLogic is a simulation software platform built on object-oriented Java programming. It supports the integration of three major simulation paradigms: system dynamics, discrete-event simulation, and agent-based modeling. The fundamental building block of an AnyLogic model is an active entity, referred to as an agent. Each agent operates independently while being simulated concurrently and is capable of interacting with other agents, as well as with its surrounding environment.

Agents encapsulate attributes, behaviours, and methods, and their dynamic behaviour and state transitions are typically represented using statecharts within the AnyLogic framework. AnyLogic also provides advanced tools, such as the simulation-based OptQuest optimization package, which enables automated parameter optimization.

The AnyLogic simulation environment has been widely applied in diverse domains, including epidemic spread modeling [218], industrial and manufacturing system analysis [219], complex system design and performance evaluation [220], computer and communication system performance analysis [221], military and defense system modeling [222], transportation

and pedestrian dynamics [223], supply chain management [224], and business process and organizational modeling [225].

A key advantage of AnyLogic is the flexibility to incorporate Java code at any point within the model, allowing for extensive customization and adaptation to meet specific modeling requirements. Additionally, AnyLogic supports the creation of Java applets from operational models, enabling deployment and distribution via web platforms. In this study, AnyLogic version 8.0 was used for model development and simulation.

5.6.3 Model Formulation

An agent is the fundamental unit of an agent-based model (ABM). In AnyLogic, a class of active agents is defined by specifying spatial location and visual representation. The position of each agent within the computational domain is described using Cartesian coordinates (x, y), and its appearance is assigned using predefined graphical shapes available in AnyLogic. In this study, agents representing park visitors are visualized as small filled circles.

The computational domain represents Canada's Wonderland and is generated using a map from Google Maps, which is a tool within the AnyLogic framework (Figure 5.13). The park contains a designated entrance through which visitors enter the system and subsequently move along predefined pathways to access various rides according to assigned itineraries. Five different visitor routes are constructed using the pedestrian library in AnyLogic. These visitor routes or itineraries are described below. Visitors spend a prescribed amount of time on each ride, as specified by park regulations. These dwell times are explicitly incorporated into the model to capture the effects of prolonged contact and potential environmental contamination effects on disease transmission. A representative pedestrian flow diagram is shown in Figure 5.14.

Canada's Wonderland features 18 roller coasters and more than 60 thrill rides, which motivated the construction of multiple visitor itineraries (Table 5.2, also shown in Figure 5.14).

Three itineraries ($IT1 - IT3$) focus on different combinations of thrill rides and coasters. KidZville and Planet Snoopy together offer more than 25 family-friendly attractions; therefore, dedicated family-oriented itineraries ($IT1, IT4, IT5$) are included to represent visitors with young children. In addition, Splash Works is a 20-acre water park with 17 attractions, which motivates the itinerary $IT5$, which represents visitors who spend a substantial portion of their visit engaging in water-based activities. Visitors are generated from a pedestrian source and progress through these itineraries while interacting with other agents and the environment during movement and ride usage.

We note that the itineraries used here are assumed by the modeller and are not actual itineraries determined from visitor data sets. We do not have such data, so move forward with reasonable itineraries that we have decided on. If the theme park provides data, the itineraries can be easily modified.

Itinerary	**Description**
IT1	Combination of family rides and selected thrill rides
IT2	Combination of coaster and thrill rides
IT3	Alternative combination of coaster and thrill rides
IT4	Family rides and KidZville attractions
IT5	KidZville and water park (Splash Works)

Table 5.2: Visitor itineraries used in the ABM

The process of disease transmission and the health conditions of agents are regulated by a state chart that outlines the discrete states of the disease and the rules of transition between them (Figure 5.15). This state chart illustrates the progression through various stages of infection and dictates agent behaviour according to their current health status.

Disease transmission is simulated on the basis of proximity from contact. When two agents find themselves within a radius of 2 m (following public health social distancing recommendations [215, 216]), a contact event may take place. Transitions between health states are initiated by conditions defined within the state chart. Susceptible visitors enter the computational area at a specified arrival rate, accompanied by a minor proportion of infectious

Figure 5.13: Theme park map (top) and Anylogic platform map(bottom) for ABM.

visitors. Should a susceptible agent come within 2m of an infectious agent, a signal marked *infect* is produced, indicating successful contact. Infection occurs probabilistically according to the disease transmission rate, leading the agent to shift to the exposed state. After a latent period of 3 days ($3 \times 24 \times 60$ mins) [207], exposed agents advance to the infectious state. Infectious agents are capable of spreading infection to surrounding susceptible agents by sending the *infect* signal during internal state transitions.

Recovery is often modeled as occurring at a rate that is the reciprocal of the infectious period. However, since the simulation's time frame is brief compared to the recovery time required, recovery is not factored into this study, and the recovery rate is assigned a value of $\alpha = 0$.

The main objective of the model is to assess how the use of personal protective equipment (PPE) by visitors and staff affects the transmission of disease within the park. PPE is represented by adjusting the baseline transmission rate β. In particular, transmission occurs when

$$\text{Uniform}(0,1) < \beta\,(1 - \text{effi} \times \text{PPE})\,,$$

where β signifies the baseline disease transmission rate, $\text{PPE} \in \{0,1\}$ denotes the presence or absence of personal protective equipment, and $\text{effi} \in (0,1)$ reflects the effectiveness of PPE in reducing the probability of transmission. The stochastic variable $\text{Uniform}(0,1)$ represents a random selection from a uniform distribution in the range $(0,1)$, implemented in AnyLogic to represent probabilistic transmission events. Surface cleaning was incorporated into the model as a standard baseline process (e.g., a cleaning interval of 60 minutes) and was not altered between simulation scenarios; thus, the separate influence of cleaning on transmission reduction is not assessed in this research.

We examine the dynamics of disease transmission within the theme park in two classes of intervention scenarios: uncontrolled transmission in the absence of personal protective equipment ($\text{PPE} = 0$) and mitigated transmission in full compliance with PPE ($\text{PPE} = 1$).

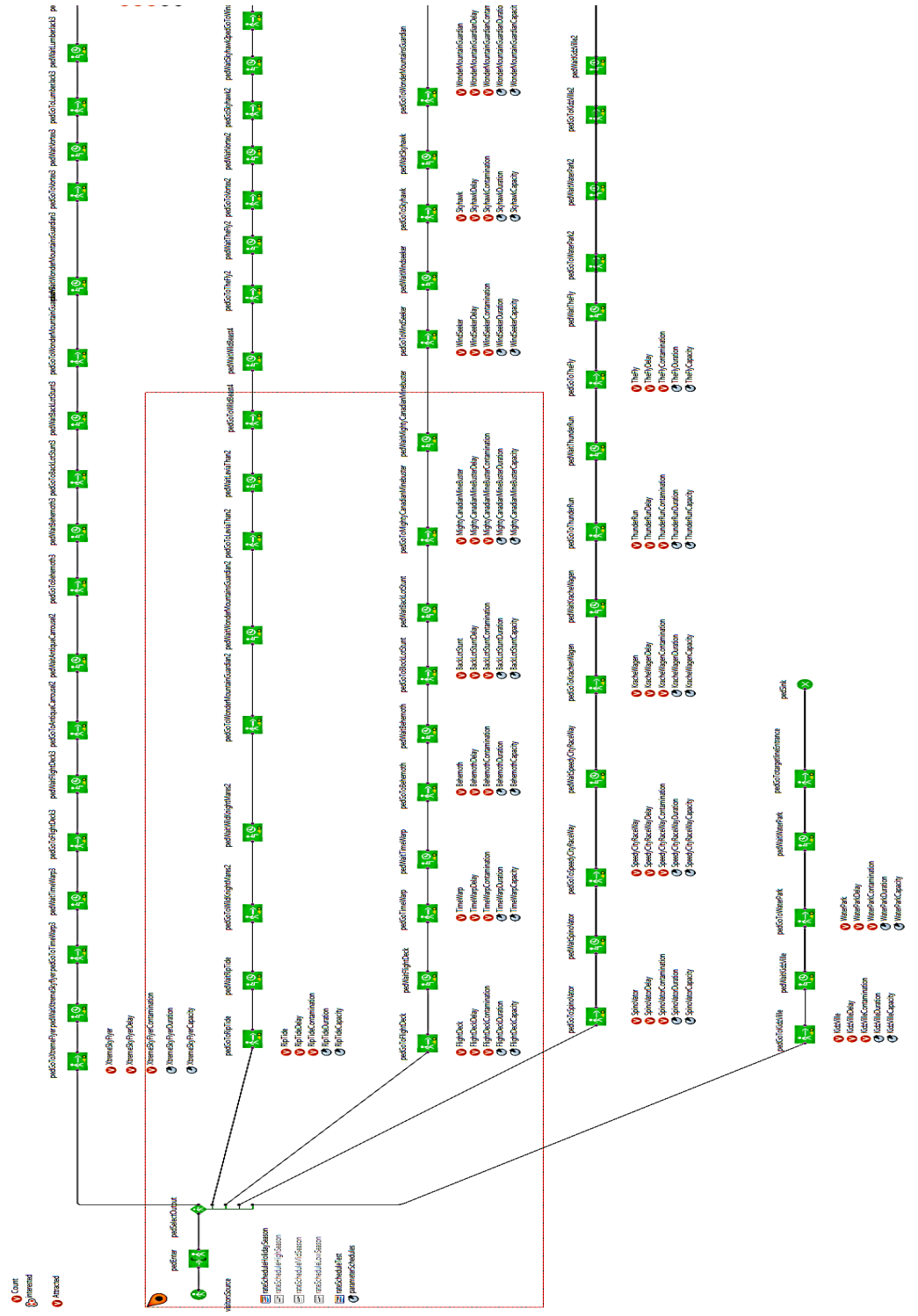

Figure 5.14: The flow diagram is used to represent visitor trajectories within the park, from entry points to ride locations, as implemented in the agent-based model.

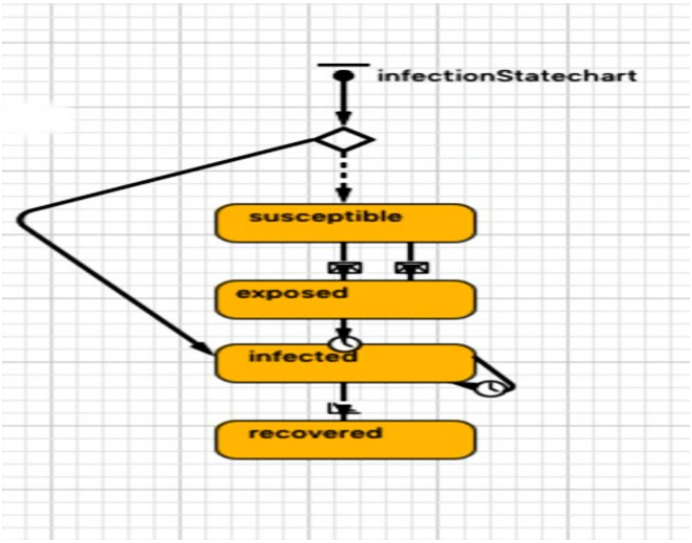

Figure 5.15: Infection State Chart for ABM

When PPE is implemented, its effectiveness is quantified using an efficacy parameter, denoted by effi, with values effi = 0.2 and effi = 0.6 [217, 214] considered to represent moderate and higher levels of protection. All other parameter values are fixed and are listed in Table 5.1. The agent-based visitor model is simulated over a 12-hour operating period (8:00 AM − 9:00 PM), representing a single day of park operations. Simulations are performed using the AnyLogic Cloud platform, with system dynamics components numerically integrated using the Euler–Newton scheme. Visitors continuously enter and exit the park according to a time-varying arrival schedule, reflecting empirical observations that attendance in theme park environments is not uniformly distributed throughout the day, but varies with time of day and visitor demand [226, 227]. This produces a dynamic visitor population with substantial turnover during the operating period.

Upon entry, each visitor is assigned an individual walking speed drawn from a uniform distribution, $\text{Uniform}(0, 1), \text{ms}^{-1}$, representing heterogeneity in pedestrian movement. This range is consistent with empirical measurements of pedestrian walking speeds reported in the transportation and pedestrian dynamics literature and is commonly used in agent-based models of crowd movement in recreational and public environments [228, 229]. Each visitor

then follows one of five predefined itineraries, selected according to the entry probabilities $(0.1, 0.1, 0.1, 0.3, 0.4)$. These itinerary probabilities are scenario-based inputs chosen to represent heterogeneous visitor preferences and to generate unequal demand between attractions. Specific values are not intended to reproduce proprietary attendance data for a particular venue but rather to support an exploratory analysis of how spatial heterogeneity and visitor routing influence exposure patterns. The agent-based modeling framework is fully flexible, and empirically informed itinerary probabilities provided by park operators could be directly incorporated in future applications without altering the underlying model structure.

The dwell time at each attraction is specified using ride duration information published on the official Canada's Wonderland website [230]. These values are used to parameterize the time visitors spend at individual rides and to ensure that attraction level occupancy durations reflect realistic operational characteristics rather than hypothetical assumptions.

A small fraction of visitors are assumed to be infectious upon entry into the park. The infection status is probabilistically assigned such that a visitor is infected if $\text{Uniform}(0, 1) <$ infectedEnterProb, where infectedEnterProb $= 0.01$. This value represents a low-prevalence baseline scenario rather than a calibrated estimate of local infection prevalence and reflects evidence that a non-negligible proportion of infections may be asymptomatic or undetected in the community [231, 232].

5.7 Results

We analyze disease transmission dynamics in the theme park under three intervention scenarios: no personal protective equipment (PPE $= 0$), moderate PPE efficacy (effi $= 0.2$), and higher PPE efficacy (effi $= 0.6$). All results are reported primarily as population-normalized rates, expressed as new events per 100 visitors per minute. This normalization accounts for the continuously changing park population and allows meaningful comparison across time periods and intervention scenarios.

Unless otherwise stated, all time-series plots correspond to a single representative stochastic realization selected to illustrate qualitative differences between scenarios.

Figure 5.16(a) shows the rate of new exposures per 100 visitors per minute under the three PPE scenarios. Throughout the operating period, the exposure rates remain below one new exposure per 100 visitors per minute, indicating that although exposure events occur frequently at the population level, the instantaneous risk to any individual visitor is low. Pronounced temporal fluctuations are observed that arise from stochastic contact processes, heterogeneous visitor movement, and time-varying crowd density driven by scheduled arrivals and departures. Comparing intervention scenarios, the no-PPE case consistently exhibits the highest exposure rates. Introducing PPE reduces exposure rates, with the greatest reduction observed when effi = 0.6. The relative ordering of scenarios (No PPE $>$ 0.2 PPE $>$ 0.6 PPE) remains consistent throughout the operating period. Exposure rates increase during peak attendance periods and decrease toward the end of the day as the density of visitors decreases.

Figure 5.16(b) presents the infection rate per 100 visitors per minute, decomposed into contributions from direct interpersonal contact and environmental contamination. Across the operating period, direct contact represents the primary source of new infections, while environmental contamination contributes a smaller but non-negligible background risk, consistent with transient surface-mediated exposure in settings with continuous visitor turnover. This reflects the transient nature of surface-mediated exposure in a setting with continuous visitor turnover and limited dwell time at shared locations. Importantly, total infection rates remain well below one new infection per 100 visitors per minute throughout the day across all scenarios. Thus, although infections occur at the population level, the instantaneous risk to any single visitor during a given minute remains low. The implementation of PPE reduces infection rates across both transmission pathways, with higher efficacy producing larger reductions.

Figure 5.16(c) shows the itinerary specific infection rates per 100 visitors per minute arising from environmental contamination. Because itinerary-specific population sizes are not tracked explicitly within the agent-based model, rates are normalized using the expected number of visitors following each itinerary, calculated as the product of the itinerary entry probability and the instantaneous total park population. Temporary peaks are observed in itinerary-specific infection rates, particularly early in the operating period, when visitor numbers are small and stochastic effects are amplified. These peaks reflect the combined effects of small early-day populations and stochastic infection events, rather than sustained differences in transmission risk across itineraries. As visitor numbers increase and stabilize, infection rates across itineraries become more comparable. Across all itineraries and intervention scenarios, infection rates remain below one new infection per 100 visitors per minute, indicating that the risk of individual-level infection is low in absolute terms. Differences in cumulative infection counts across itineraries are primarily driven by differences in visitor throughput rather than differences in per-capita infection risk.

Figure 5.17(a) presents the window-averaged per-capita infection rates associated with KidzVille in three PPE scenarios (no PPE, PPE efficacy 0.2, and PPE efficacy 0.6). Each bar represents the average number of new infections per minute computed over progressively increasing time windows from the start of the operating day. Rates are normalized by the instantaneous total population of the park to account for continuous visitor turnover. Across all time windows, the no-PPE scenario exhibits the highest average infection rate, while increasing the efficacy of PPE produces progressively lower infection rates. As the averaging window increases, infection rates decline in all scenarios due to inclusion of lower-risk periods later in the day, while the relative ordering of scenarios remains consistent.

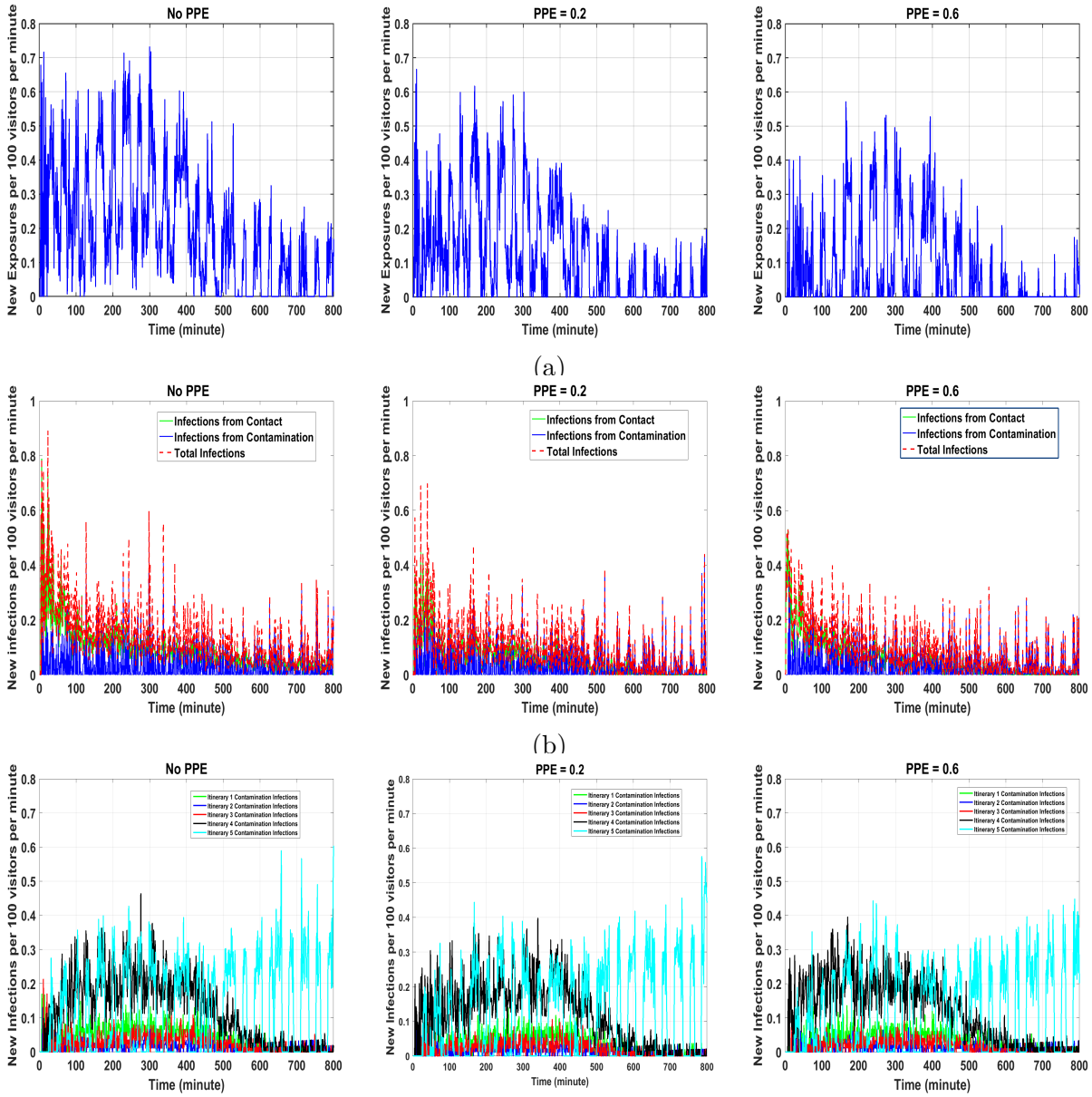

Figure 5.16: Time evolution of Per capita exposure and infection rates (per 100 visitors per minute) over the 12 hour operating period under no-PPE and PPE scenarios (effi $= 0.2, 0.6$) (left to right), obtained from a single representative stochastic simulation. (a) Time evolution of exposure risk. (b) Infection rate due to direct interpersonal contact and contamination. (c) Comparison of infection rate across visitor itineraries.

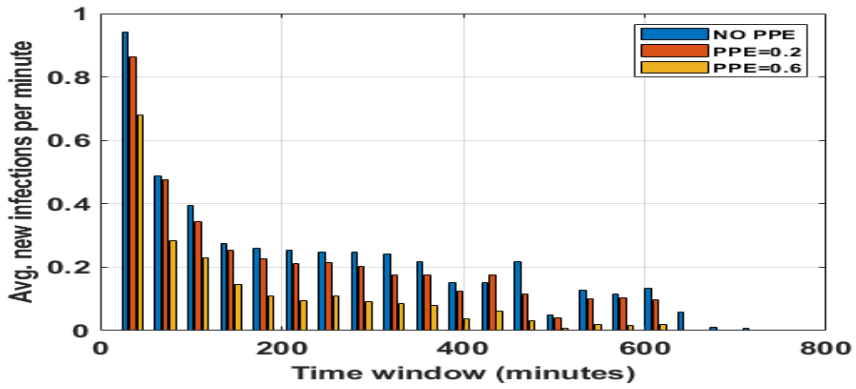

(a)

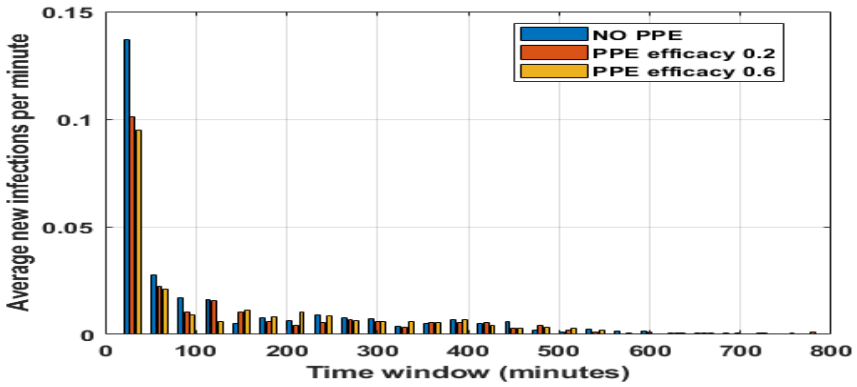

(b)

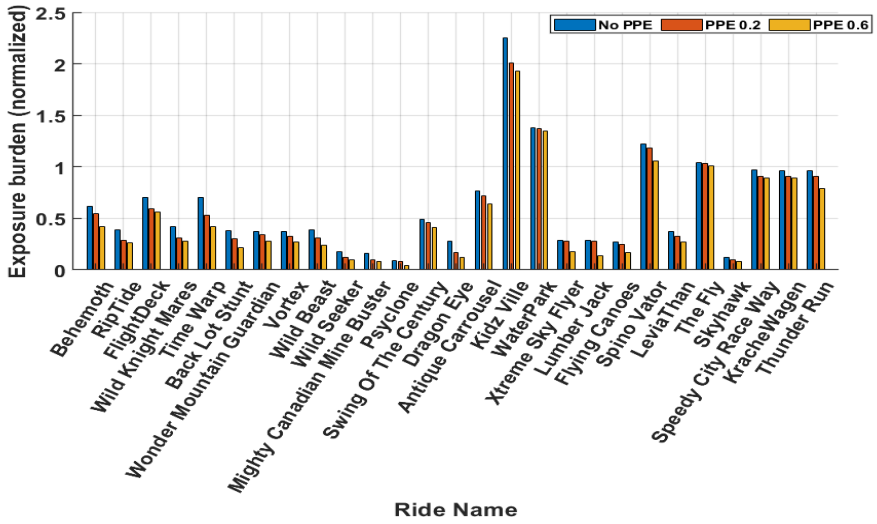

(c)

Figure 5.17: Comparison of infection and exposure metrics under different PPE scenarios. (a) Window-averaged per-capita infection rate associated with KidzVille exposure. (b) Window-averaged park-level per-capita infection rates under no PPE, PPE efficacy 0.2, and PPE efficacy 0.6. (c) Normalized cumulative exposure burden across attractions over the operating period.

Figure 5.17(b) summarizes the window averaged rate of new infections per minute, calculated over twenty progressively increasing time windows spanning the 800- minute operating period, for scenarios without PPE and with PPE implemented at different levels of efficacy. All Results are reported on a per-capita basis, enabling direct comparison across scenarios despite continuous population turnover. The no-PPE scenario consistently exhibits the highest average infection rate in all time windows. Introducing PPE leads to a clear reduction in infection rates, with a higher efficacy (effi = 0.6) producing the greatest reduction. Even moderate efficacy of PPE substantially reduces per-minute infection rates, demonstrating that partial protection is effective in limiting transmission. As the averaging window increases, the average infection rate decreases in all scenarios because longer windows incorporate later periods of lower transmission intensity. Importantly, the relative ordering of the scenarios remains unchanged across all windows, demonstrating consistent protective effects of PPE over time.

Figure 5.17(c) summarizes the distribution of the cumulative exposure burden between attractions during the operating period. Substantial heterogeneity is observed, with a small number of attractions contributing disproportionately to cumulative exposure events, while many attractions contribute relatively little. In particular, KidzVille exhibits the highest cumulative exposure burden in this representative simulation. These differences do not imply that individual visitors experience a higher instantaneous risk at specific attractions. Rather, they arise from the accumulation of exposure events over time, as large numbers of visitors sequentially pass through the same locations. This interpretation is consistent with the population-normalized results presented earlier, which show that individual-level infection rates remain low across attractions when expressed per-capita.

When infection outcomes are reported in population-normalized terms, instantaneous per-capita infection and exposure rates remain low throughout the operating day. Direct interpersonal contact represents the primary transmission pathway in the simulated environ-

ment, while environmental contamination contributes a smaller background component to the overall risk. The implementation of personal protective equipment (PPE) consistently reduces infection rates, with higher efficacy producing greater reductions across all time windows and attractions.

Although cumulative infection counts at the attraction level may appear substantial, these totals are driven primarily by sustained visitor throughput and time accumulation, rather than elevated per-capita risk at any specific location. Overall, the results indicate that infections can accumulate during the operating period due to continuous visitor flow, yet the individual-level risk during a single visit remains low and can be further mitigated through protective interventions such as PPE.

5.8 Conclusion

This chapter presented an agent-based modeling framework to evaluate COVID-19 transmission dynamics within a theme park characterized by continuous visitor turnover, heterogeneous movement patterns, and multiple transmission pathways. By explicitly representing visitor itineraries, contact interactions, and environmental exposure processes, the model captures essential features of disease spread in large-scale recreational mass-gathering environments.

A central methodological contribution of this study is the use of population-normalized, per-capita exposure, and infection rates to quantify instantaneous individual-level transmission risk. In a setting where visitors continually enter and exit the park, cumulative infection counts increase with total attendance and duration of operation. Explicitly expressing the outcomes as per-capita rates therefore provides a biologically meaningful and comparable measure of transmission intensity between time periods, attractions, itineraries, and intervention scenarios.

The results indicate that the instantaneous per-capita infection and exposure rates remain low throughout the operating day. Direct interpersonal contact emerges as the dominant

transmission pathway, while environmental contamination contributes a smaller background component. Although cumulative infections accumulate over time, this accumulation reflects sustained visitor throughput and repeated exposure opportunities in many individuals rather than elevated risk for any single visitor during a given minute of activity.

The implementation of personal protective equipment (PPE) consistently reduces the risk of infection in all analyzes. Higher efficacy produces greater reductions in transmission and even moderate efficacy significantly lowers per-minute infection rates. These findings demonstrate that protective interventions can substantially mitigate disease spread in high-contact recreational environments without imposing structural constraints on visitor movement.

In general, this modeling framework provides a quantitative basis for evaluating intervention strategies in mass-gathering settings with dynamic populations. The study underscores the importance of interpreting cumulative infection counts alongside population-normalized risk metrics and highlights the value of per-capita measures to assess transmission dynamics in complex public venues.

Chapter 6

Conclusion and Future Work

In this thesis we have used infectious disease models to study the dynamics of infectious diseases, namely in measles, influenza, COVID-19, and influenza spread in populations with different population structures, new model terms or functions, and/or waning immunity. We have also studied an in-host model of HIV infection. The models and analyses presented in this thesis offer valuable information on the mechanisms that drive and control infectious disease transmission on multiple scales. Each study also reveals specific areas that could be refined or extended in future work. The purpose of these improvements is to make the models more biologically realistic, increase their predictive strength, and improve their usefulness for public health policy.

The first study focused on the dynamics of HIV infection within the host in a model with the addition of the virus loss term. Here, we examined how target cells, infected cells, and viral particles interact through bifurcation, basin-of-attraction, and sensitivity analyses. The model captured important behaviours such as bistability and backward bifurcation. Previous works have shown that the addition of the virus loss term can induce a Hopf bifurcation or oscillatory behaviour that can be used to induce periodic increases in HIV viral load (or viral blips). We did not find this in our model. Several extensions of our model are possible that we can consider that may induce oscillatory dynamics. For example, adding

time-dependent immune responses, treatment delays, or stochastic effects could capture this. Taking into account immune exhaustion, drug resistance, and viral mutation would also improve understanding of long-term persistence.

The second study investigated measles transmission while accounting for waning immunity and vaccination. Future work might include age-structured contact patterns, uneven vaccine uptake, or spatial heterogeneity to better reflect real-world transmission. Considering different types of vaccine, imperfect protection, and timing of booster campaigns could strengthen outbreak predictions. Including demographic turnover and migration would further increase the value of the model for long-term eradication planning and surveillance.

The third study explored influenza transmission in the presence of waning immunity and periodic vaccination. Although the model captured seasonal patterns and emphasized the need for booster programs, additional extensions are possible. Adaptive vaccination schedules, strain replacement, and cross-protection between influenza subtypes could be investigated. Incorporating environmental drivers such as temperature and humidity, stochastic seasonality, and global travel patterns would help forecast resurgence and guide the design of long-lasting or 'universal' vaccines.

The fourth study, described in Chapter 5A, examined infection spread in theme parks using a deterministic model focusing on environmental and behavioral control measures. It evaluated the influence of testing, PPE use, and cleaning practices on transmission. Future versions of the model could include economic optimization to weigh intervention costs against benefits. Adding behavioral variability, differing compliance levels, and real-time data integration would make the model more practical for managing disease risk in mass-gathering environments.

The fifth study (Chapter 5B) introduced an agent-based model of COVID-19 transmission at Canada's Wonderland Park. This model provided a detailed representation of spatial movement, contact networks, and surface contamination within a large recreational environ-

ment. The framework could be extended to simulate interactions between multiple pathogens, incorporate visitor demographics, or evaluate additional mitigation strategies such as virtual queueing systems and automated crowd monitoring. Linking the simulation with real-world surveillance data could enable future model calibration and near real-time risk assessment. Further extensions may include modeling staff vaccination, behavioral heterogeneity, and varying levels of compliance in order to improve predictive capability.

Together, these directions point toward a more integrated understanding of infectious disease dynamics. Combining biological mechanisms, behavioral patterns, and environmental processes within hybrid modeling frameworks—such as linking within-host and population-level models, or integrating deterministic and agent-based approaches—would allow for deeper insight into infection persistence and control. As data availability improves, the incorporation of parameter inference and data assimilation methods may help transform these models into practical tools to support public health decision-making and outbreak management in complex, high-traffic settings.

Bibliography

[1] Laurence Cole and Peter R Kramer. "Bacteria, virus, fungi, and infectious diseases". In: *Human Physiology, Biochemistry and Basic Medicine* (2015), p. 193.

[2] Abigail Bartlett et al. "A comprehensive list of bacterial pathogens infecting humans". In: *Microbiology* 168.12 (2022), p. 001269.

[3] Jaishree Paul. "Introduction to infectious diseases". In: *Disease Causing Microbes*. Springer, 2024, pp. 1–63.

[4] Lidia Morawska and Junji Cao. "Airborne transmission of SARS-CoV-2: The world should face the reality". In: *Environment international* 139 (2020), p. 105730.

[5] David M Morens, Gregory K Folkers, and Anthony S Fauci. "Emerging infections: a perpetual challenge". In: *The Lancet infectious diseases* 8.11 (2008), pp. 710–719.

[6] World Health Organization. *Managing epidemics: key facts about major deadly diseases*. World Health Organization, 2023.

[7] Alan S. Perelson. "Modeling the within-host dynamics of HIV infection". In: *BMC Biology* (2013).

[8] Nicole Mideo, Samuel Alizon, and Troy Day. "Linking within- and between-host dynamics in the evolutionary epidemiology of infectious diseases". In: *Trends in Ecology & Evolution* (2008).

[9] Nicholas C. Grassly and Christophe Fraser. “Mathematical models of infectious disease transmission”. In: *Nature Reviews Microbiology* (2008).

[10] Hans Heesterbeek et al. “Modeling infectious disease dynamics in the complex landscape of global health”. In: *Science* (2015). DOI: 10.1126/science.aaa4339.

[11] Neil M. Ferguson et al. “Strategies for mitigating an influenza pandemic”. In: *Nature* (2006).

[12] Alun L. Lloyd. “Realistic distributions of infectious periods in epidemic models: changing patterns of persistence and dynamics”. In: *Theoretical Population Biology* (2001).

[13] Matt J. Keeling and Ken T. D. Eames. “Networks and epidemic models”. In: *Journal of the Royal Society Interface* (2005).

[14] Ken T. D. Eames and Matt J. Keeling. “Modeling dynamic and network heterogeneities in the spread of sexually transmitted diseases”. In: *Proceedings of the National Academy of Sciences* (2002).

[15] Roy M Anderson. “Discussion: the Kermack-McKendrick epidemic threshold theorem”. In: *Bulletin of mathematical biology* 53.1 (1991), pp. 1–32.

[16] Jane M Heffernan, Robert J Smith, and Lindi M Wahl. “Perspectives on the basic reproductive ratio”. In: *Journal of the Royal Society Interface* 2.4 (2005), pp. 281–293.

[17] David D Ho et al. “Rapid turnover of plasma virions and CD4 lymphocytes in HIV-1 infection”. In: *Nature* 373.6510 (1995), pp. 123–126.

[18] Alan S Perelson et al. “HIV-1 dynamics in vivo: virion clearance rate, infected cell life-span, and viral generation time”. In: *Science* 271.5255 (1996), pp. 1582–1586.

[19] Martin Nowak and Robert M May. *Virus dynamics: mathematical principles of immunology and virology: mathematical principles of immunology and virology*. Oxford University Press, UK, 2000.

[20] Katarzyna A Rejniak. "An immersed boundary framework for modelling the growth of individual cells: an application to the early tumour development". In: *Journal of theoretical biology* 247.1 (2007), pp. 186–204.

[21] Alan S Perelson and Patrick W Nelson. "Mathematical analysis of HIV-1 dynamics in vivo". In: *SIAM review* 41.1 (1999), pp. 3–44.

[22] Stanca M. Ciupe and Jane M. Heffernan. "In-host modeling". In: *Infectious Disease Modelling* 2.2 (2017), pp. 188–202. ISSN: 2468-0427. DOI: https://doi.org/10.1016/j.idm.2017.04.002. URL: https://www.sciencedirect.com/science/article/pii/S2468042717300039.

[23] Dominik Wodarz. *Killer cell dynamics: mathematical and computational approaches to immunology*. Springer, 2007.

[24] Jane M Heffernan, Robert J Smith, and Lindi M Wahl. "Perspectives on the basic reproductive ratio". In: *Journal of the Royal Society Interface* 2.4 (2005), pp. 281–293.

[25] Matt J. Keeling and Pejman Rohani. *Modeling Infectious Diseases in Humans and Animals*. Princeton University Press, 2008.

[26] Fabrice Carrat and Antoine Flahault. "Influenza vaccine: the challenge of antigenic drift". In: *Vaccine* 25.39-40 (2007), pp. 6852–6862.

[27] Cynthia Nypaver, Cynthia Dehlinger, and Chelsea Carter. "Influenza and influenza vaccine: a review". In: *Journal of midwifery & women's health* 66.1 (2021), pp. 45–53.

[28] Alan J Hay et al. "The evolution of human influenza viruses". In: *Philosophical Transactions of the Royal Society of London. Series B* 356.1416 (2001), p. 1861.

[29] Arthur WD Edridge et al. "Seasonal coronavirus protective immunity is short-lasting". In: *Nature medicine* 26.11 (2020), pp. 1691–1693.

[30] Aaron M Wendelboe et al. “Duration of immunity against pertussis after natural infection or vaccination”. In: *The Pediatric infectious disease journal* 24.5 (2005), S58–S61.

[31] Jane M. Heffernan and Matt J. Keeling. “Implications of vaccination and waning immunity”. In: *Proceedings of the Royal Society B: Biological Sciences* 276.1664 (2009), pp. 2071–2080.

[32] Tiffany Leung et al. “Infection-acquired versus vaccine-acquired immunity in an SIRWS model”. In: *Infectious Disease Modelling* 3 (2018), pp. 118–135.

[33] Jennie S Lavine et al. “Immune boosting explains regime-shifts in prevaccine-era pertussis dynamics”. In: *PloS one* 8.8 (2013), e72086.

[34] Narumichi Iwamura and Kanako Tsutsumi. “Predicting the Airborne Transmission of Measles: Impact of Indoor Carbon Dioxide (CO2) Levels and Mitigation Strategies”. In: *Cureus* 16.7 (2024).

[35] World Health Organization (WHO). *Measles: Key facts*. `https://www.who.int/news-room/fact-sheets/detail/measles`. Accessed: 2025-11-08. 2024.

[36] Sotiris Vardoulakis et al. “COVID-19 environmental transmission and preventive public health measures”. In: *Australian and New Zealand Journal of Public Health* 44.5 (2020), pp. 333–335.

[37] Zhaoyuan Gong et al. “Natural and socio-environmental factors in the transmission of COVID-19: a comprehensive analysis of epidemiology and mechanisms”. In: *BMC Public Health* 24.1 (2024), p. 2196.

[38] Ben Lopman et al. “Environmental transmission of norovirus gastroenteritis”. In: *Current opinion in virology* 2.1 (2012), pp. 96–102.

[39] John A Marshall and Leesa D Bruggink. “The dynamics of norovirus outbreak epidemics: recent insights”. In: *International Journal of Environmental Research and Public Health* 8.4 (2011), pp. 1141–1149.

[40] Sherry Towers et al. “Quantifying the relative effects of environmental and direct transmission of norovirus”. In: *Royal Society open science* 5.3 (2018), p. 170602.

[41] Joseph H Tien and David JD Earn. “Multiple transmission pathways and disease dynamics in a waterborne pathogen model”. In: *Bulletin of mathematical biology* 72.6 (2010), pp. 1506–1533.

[42] Romulus Breban, John M Drake, and Pejman Rohani. “A general multi-strain model with environmental transmission: invasion conditions for the disease-free and endemic states”. In: *Journal of theoretical biology* 264.3 (2010), pp. 729–736.

[43] Cláudia Torres Codeço. “Endemic and epidemic dynamics of cholera: the role of the aquatic reservoir”. In: *BMC Infectious diseases* 1.1 (2001), p. 1.

[44] Romulus Breban et al. “The role of environmental transmission in recurrent avian influenza epidemics”. In: *PLoS computational biology* 5.4 (2009), e1000346.

[45] David M Hartley, J Glenn Morris Jr, and David L Smith. “Hyperinfectivity: a critical element in the ability of V. cholerae to cause epidemics?” In: *PLoS medicine* 3.1 (2006), e7.

[46] Stefania Ottaviano, Mattia Sensi, and Sara Sottile. “Global stability of multi-group SAIRS epidemic models”. In: *Mathematical Methods in the Applied Sciences* 46.13 (2023), pp. 14045–14071.

[47] Sebastien Regis et al. “A data-based approach using a multi-group SIR model with fuzzy subsets: application to the COVID-19 simulation in the islands of Guadeloupe”. In: *Biology* 10.10 (2021), p. 991.

[48] Pauline Van den Driessche. "Reproduction numbers of infectious disease models". In: *Infectious disease modelling* 2.3 (2017), pp. 288–303.

[49] Tom Britton, Frank Ball, and Pieter Trapman. "A mathematical model reveals the influence of population heterogeneity on herd immunity to SARS-CoV-2". In: *science* 369.6505 (2020), pp. 846–849.

[50] Toshikazu Kuniya, Jinliang Wang, and Hisashi Inaba. "A MULTI-GROUP SIR EPIDEMIC MODEL WITH AGE STRUCTURE." In: *Discrete & Continuous Dynamical Systems-Series B* 21.10 (2016).

[51] World Health Organization. *HIV/AIDS Fact Sheet*. `https://www.who.int/news-room/fact-sheets/detail/hiv-aids`. Accessed October 2025. 2024.

[52] UNAIDS. *Global HIV AIDS statistics — 2024 fact sheet*. `https://www.unaids.org/en/resources/fact-sheet`. Accessed October 2025. 2024.

[53] F. Barré-Sinoussi et al. "Isolation of a T-lymphotropic retrovirus from a patient at risk for acquired immune deficiency syndrome (AIDS)". In: *Science* 220.4599 (1983), pp. 868–871. DOI: `10.1126/science.6189183`.

[54] Centers for Disease Control and Prevention. *How HIV Spreads*. `https://www.cdc.gov/hiv/basics/transmission.html`. Accessed October 2025. 2024.

[55] Centers for Disease Control and Prevention. *HIV Testing Overview: Viral Load and CD4 Count*. `https://www.cdc.gov/hiv/basics/hiv-testing/diagnostic-tests.html`. Accessed October 2025. 2024.

[56] M. S. Cohen et al. "Antiretroviral therapy for the prevention of HIV-1 transmission". In: *New England Journal of Medicine* 375.9 (2016), pp. 830–839. DOI: `10.1056/NEJMoa1600693`.

[57] World Health Organization. *Antiretroviral therapy (ART)*. https://www.who.int/news-room/questions-and-answers/item/hiv-antiretroviral-therapy-(art). Accessed October 2025. 2024.

[58] World Health Organization. *Measles fact sheet*. https://www.who.int/news-room/fact-sheets/detail/measles. Accessed October 2025. 2024.

[59] Centers for Disease Control and Prevention. *Transmission of Measles*. https://www.cdc.gov/measles/about/transmission.html. Accessed October 2025. 2024.

[60] Centers for Disease Control and Prevention. *Measles Vaccination: What Everyone Should Know*. https://www.cdc.gov/vaccines/vpd/measles/public/index.html. Accessed October 2025. 2024.

[61] William J. Moss. "Measles". In: *The Lancet* 390.10111 (2017), pp. 2490–2502. DOI: 10.1016/S0140-6736(17)31463-0.

[62] World Health Organization. *Influenza (Seasonal) Fact Sheet*. https://www.who.int/news-room/fact-sheets/detail/influenza-(seasonal). Accessed October 2025. 2024.

[63] Centers for Disease Control and Prevention. *Influenza (Flu): Overview*. https://www.cdc.gov/flu/about/keyfacts.html. Accessed October 2025. 2024.

[64] R. Tellier et al. "Recognition of aerosol transmission of infectious agents: a commentary". In: *BMC Infectious Diseases* 19.1 (2019), p. 101. DOI: 10.1186/s12879-019-3707-y.

[65] C. Paules and K. Subbarao. "Influenza". In: *The Lancet* 390.10095 (2017), pp. 697–708. DOI: 10.1016/S0140-6736(17)30129-0.

[66] J. K. Taubenberger and D. M. Morens. "The pathology of influenza virus infections". In: *Annual Review of Pathology: Mechanisms of Disease* 3 (2008), pp. 499–522. DOI: 10.1146/annurev.pathmechdis.3.121806.154316.

[67] F. Krammer et al. “Influenza”. In: *Nature Reviews Disease Primers* 4.1 (2018), p. 3. DOI: 10.1038/s41572-018-0002-y.

[68] Centers for Disease Control and Prevention. *Key Facts About Seasonal Flu Vaccine*. https://www.cdc.gov/flu/prevent/keyfacts.htm. Accessed October 2025. 2024.

[69] M. Biggerstaff et al. “Estimates of the reproduction number for seasonal, pandemic, and zoonotic influenza: a systematic review of the literature”. In: *BMC Infectious Diseases* 14.480 (2014). DOI: 10.1186/1471-2334-14-480.

[70] Centers for Disease Control and Prevention. *Norovirus: Technical Fact Sheet*. https://www.cdc.gov/norovirus/about/index.html. Accessed October 2025. 2024.

[71] M. M. Patel et al. “Noroviruses: a comprehensive review”. In: *Journal of Clinical Virology* 44.1 (2009), pp. 1–8. DOI: 10.1016/j.jcv.2008.10.009.

[72] R. I. Glass, U. D. Parashar, and M. K. Estes. “Norovirus gastroenteritis”. In: *New England Journal of Medicine* 361.18 (2009), pp. 1776–1785. DOI: 10.1056/NEJMra0804575.

[73] Centers for Disease Control and Prevention. *How Norovirus Spreads*. https://www.cdc.gov/norovirus/transmission/index.html. Accessed October 2025. 2024.

[74] Jennifer L. Cannon et al. “Survival of human norovirus surrogates in water and on environmental surfaces”. In: *Journal of Food Protection* 69.4 (2006), pp. 1105–1110. DOI: 10.4315/0362-028X-69.4.1105.

[75] Jennifer L Cannon et al. “Surrogates for the study of norovirus stability and inactivation in the environment: a comparison of murine norovirus and feline calicivirus”. In: *Journal of food protection* 69.11 (2006), pp. 2761–2765.

[76] BI Escudero et al. “Persistence and transferability of noroviruses on and between common surfaces and foods”. In: *Journal of food protection* 75.5 (2012), pp. 927–935.

[77] P. F. M. Teunis et al. “Norwalk virus: how infectious is it?” In: *Journal of Medical Virology* 80.8 (2008), pp. 1468–1476. DOI: 10.1002/jmv.21237.

[78] G. I. Parra et al. “Static and evolving norovirus genotypes: implications for epidemiology and immunity”. In: *Viruses* 11.2 (2019), E199. DOI: 10.3390/v11020199.

[79] S. J. Olsen, D. Acheson, and R. I. Glass. “Transmission and control of norovirus outbreaks”. In: *Emerging Infectious Diseases* 26.10 (2020), pp. 2319–2326. DOI: 10.3201/eid2610.201091.

[80] World Health Organization. *Coronavirus disease (COVID-19) Fact sheet*. https://www.who.int/news-room/fact-sheets/detail/coronavirus-disease-(covid-19). Accessed October 2025. 2024.

[81] B. Hu et al. “Characteristics of SARS-CoV-2 and COVID-19”. In: *Nature Reviews Microbiology* 19.3 (2021), pp. 141–154. DOI: 10.1038/s41579-020-00459-7.

[82] World Health Organization. *Naming the coronavirus disease (COVID-19) and the virus that causes it*. https://www.who.int/emergencies/diseases/novel-coronavirus-2019/technical-guidance/naming-the-coronavirus-disease. Accessed October 2025. 2020.

[83] World Health Organization. *Modes of transmission of virus causing COVID-19*. https://www.who.int/news-room/commentaries/detail/modes-of-transmission-of-virus-causing-covid-19-implications-for-ipc-precaution-recommendations. Accessed October 2025. 2020.

[84] Centers for Disease Control and Prevention. *CDC COVID-19 Timeline*. https://www.cdc.gov/museum/timeline/covid19.html. Accessed October 2025. 2024.

[85] C. Huang et al. “Clinical features of patients infected with 2019 novel coronavirus in Wuhan, China”. In: *The Lancet* 395.10223 (2020), pp. 497–506. DOI: 10.1016/S0140-6736(20)30183-5.

[86] D. A. Berlin, R. M. Gulick, and F. J. Martinez. “Severe COVID-19”. In: *New England Journal of Medicine* 383 (2020), pp. 2451–2460. DOI: 10.1056/NEJMcp2009575.

[87] F. Zhou et al. “Clinical course and risk factors for mortality of adult inpatients with COVID-19 in Wuhan, China: a retrospective cohort study”. In: *The Lancet* 395.10229 (2020), pp. 1054–1062. DOI: 10.1016/S0140-6736(20)30566-3.

[88] F. P. Polack et al. “Safety and efficacy of the BNT162b2 mRNA COVID-19 vaccine”. In: *New England Journal of Medicine* 383.27 (2020), pp. 2603–2615. DOI: 10.1056/NEJMoa2034577.

[89] S. Flaxman et al. “Estimating the effects of non-pharmaceutical interventions on COVID-19 in Europe”. In: *Nature* 584.7820 (2020), pp. 257–261. DOI: 10.1038/s41586-020-2405-7.

[90] A. Fontanet and S. Cauchemez. “COVID-19 herd immunity: where are we?” In: *Nature Reviews Immunology* 21.9 (2021), pp. 583–584. DOI: 10.1038/s41577-021-00651-3.

[91] Evgeny B. Postnikov. “Estimation of COVID-19 dynamics “on a back of envelope”: bifurcation analysis and parameter estimation for the SIR model”. In: *Chaos, Solitons & Fractals* 135 (2020), p. 109841. DOI: 10.1016/j.chaos.2020.109841.

[92] Pauline van den Driessche. “Reproduction numbers of infectious disease models”. In: *Infectious Disease Modelling* 2.3 (2017), pp. 288–303. DOI: 10.1016/j.idm.2017.06.002.

[93] Maia Martcheva. *An Introduction to Mathematical Epidemiology*. New York, NY: Springer, 2015. ISBN: 978-1-4899-7611-0.

[94] Arjun Kumar et al. “Stability and bifurcation analysis of an infectious disease model with different optimal control strategies”. In: *Mathematics & Computers in Simulation* 213 (2023), pp. 78–114. DOI: 10.1016/j.matcom.2023.05.024. URL: https://www.sciencedirect.com/science/article/pii/S0378475423002434.

[95] E. A. Iboi, C. N. Ngonghala, and A. B. Gumel. "Will an imperfect vaccine curtail the COVID-19 pandemic in the U.S.?" In: *Infectious Disease Modelling* 5 (2020), pp. 510–524. DOI: 10.1016/j.idm.2020.07.006.

[96] Fatima Ndaïrou et al. "Mathematical modeling of COVID-19 transmission dynamics with a case study of Wuhan". In: *Chaos, Solitons & Fractals* 135 (2020), p. 109846. DOI: 10.1016/j.chaos.2020.109846.

[97] B. Xie, M. Liu, and L. Zhang. "Bifurcation analysis and optimal control of SEIR epidemic model with saturated treatment function on the network". In: *Mathematical Biosciences and Engineering* 19.2 (2022), pp. 1677–1696. DOI: 10.3934/mbe.2022079. URL: https://doi.org/10.3934/mbe.2022079.

[98] Roy M. Anderson and Robert M. May. *Infectious Diseases of Humans: Dynamics and Control*. Oxford University Press, 1991.

[99] Herbert W Hethcote. "The mathematics of infectious diseases". In: *SIAM review* 42.4 (2000), pp. 599–653.

[100] William Ogilvy Kermack and Anderson G McKendrick. "A contribution to the mathematical theory of epidemics". In: *Proceedings of the royal society of london. Series A, Containing papers of a mathematical and physical character* 115.772 (1927), pp. 700–721.

[101] Linda JS Allen. "An introduction to stochastic epidemic models". In: *Mathematical epidemiology*. Springer, 2008, pp. 81–130.

[102] Daniel T Gillespie. "Exact stochastic simulation of coupled chemical reactions". In: *The journal of physical chemistry* 81.25 (1977), pp. 2340–2361.

[103] Christian P Robert, George Casella, and George Casella. *Monte Carlo statistical methods*. Vol. 2. Springer, 2004.

[104] Odo Diekmann, Hans Heesterbeek, and Tom Britton. *Mathematical tools for understanding infectious disease dynamics*. Vol. 7. Princeton University Press, 2013.

[105] Linda JS Allen. "A primer on stochastic epidemic models: Formulation, numerical simulation, and analysis". In: *Infectious Disease Modelling* 2.2 (2017), pp. 128–142.

[106] Linda J. S. Allen. *An Introduction to Stochastic Processes with Applications to Biology*. 2nd. Boca Raton, FL: Chapman and Hall/CRC, 2010. ISBN: 9781439818824. DOI: 10.1201/b12537. URL: https://doi.org/10.1201/b12537.

[107] V. Ng et al. *Modelling Group Report – January 14, 2021: COVID-19 agent-based model analyses for Canada*. Tech. rep. Public Health Agency of Canada (PHAC), 2021. URL: https://nccid.ca/wp-content/uploads/sites/2/2021/01/Modelling-Group-report-2020_01_14_Final.pdf.

[108] V. Gabriele-Rivet et al. "Modelling the impact of age-stratified public health measures on SARS-CoV-2 transmission in Canada". In: *Royal Society Open Science* 8.11 (2021), p. 210834. DOI: 10.1098/rsos.210834. URL: https://royalsocietypublishing.org/doi/10.1098/rsos.210834.

[109] Seyed M Moghadas et al. "The impact of vaccination on coronavirus disease 2019 (COVID-19) outbreaks in the United States". In: *Clinical Infectious Diseases* 73.12 (2021), pp. 2257–2264.

[110] The AnyLogic Company. *The AnyLogic Simulation Software (Version 8.8.5)*. AnyLogic is a multimethod simulation platform supporting system dynamics, discrete-event, and agent-based modelling, with Java-based implementation and spatial visualization. AnyLogic North America. Chicago, IL, USA, 2022. URL: https://www.anylogic.com.

[111] Maplesoft. *Maple: Technical Computing Software (Version 2023)*. Waterloo Maple Inc. Waterloo, Ontario, Canada, 2020. URL: https://www.maplesoft.com.

[112] Wolfram Research, Inc. *Mathematica, Version 13.2*. Wolfram Research, Inc. Champaign, IL, USA, 2023. URL: https://www.wolfram.com/mathematica.

[113] The MathWorks, Inc. *MATLAB: The Language of Technical Computing (Version R2023b)*. The MathWorks, Inc. Natick, Massachusetts, USA, 2023. URL: https://www.mathworks.com.

[114] A. Dhooge, W. Govaerts, and Y. A. Kuznetsov. "MATCONT: A MATLAB package for numerical bifurcation analysis of ODEs". In: *ACM Transactions on Mathematical Software* 29.2 (2003), pp. 141–164. DOI: 10.1145/779359.779362. URL: https://doi.org/10.1145/779359.779362.

[115] Hassan K. Khalil. *Nonlinear Systems*. Prentice Hall, 2002.

[116] Joseph P. LaSalle. *The Stability of Dynamical Systems*. SIAM, 1976.

[117] Ronald L Iman and Jon C Helton. "An investigation of uncertainty and sensitivity analysis techniques for computer models". In: *Risk analysis* 8.1 (1988), pp. 71–90.

[118] Sally M Blower and Hadi Dowlatabadi. "Sensitivity and uncertainty analysis of complex models of disease transmission: an HIV model, as an example". In: *International Statistical Review/Revue Internationale de Statistique* (1994), pp. 229–243.

[119] Simeone Marino et al. "A methodology for performing global uncertainty and sensitivity analysis in systems biology". In: *Journal of theoretical biology* 254.1 (2008), pp. 178–196.

[120] Michael D McKay, Richard J Beckman, and William J Conover. "A comparison of three methods for selecting values of input variables in the analysis of output from a computer code". In: *Technometrics* 42.1 (2000), pp. 55–61.

[121] Duncan S Callaway and Alan S Perelson. "HIV-1 infection and low steady state viral loads". In: *Bulletin of mathematical biology* 64.1 (2002), pp. 29–64.

[122] Jane M Heffernan and Lindi M Wahl. "Monte Carlo estimates of natural variation in HIV infection". In: *Journal of theoretical biology* 236.2 (2005), pp. 137–153.

[123] Jane M Heffernan and Lindi M Wahl. "Natural variation in HIV infection: Monte Carlo estimates that include CD8 effector cells". In: *Journal of theoretical biology* 243.2 (2006), pp. 191–204.

[124] Marios M Hadjiandreou, Raul Conejeros, and Vassilis S Vassiliadis. "Towards a long-term model construction for the dynamic simulation of HIV infection". In: *Mathematical biosciences and engineering* 4.3 (2007), p. 489.

[125] Ian B Hogue et al. "The dual role of dendritic cells in the immune response to HIV-1 infection". In: *The Journal of general virology* 89.Pt 9 (2008), p. 2228.

[126] Yan Wang et al. "Oscillatory viral dynamics in a delayed HIV pathogenesis model". In: *Mathematical Biosciences* 219.2 (2009), pp. 104–112.

[127] Alan S Perelson and Ruy M Ribeiro. "Modeling the within-host dynamics of HIV infection". In: *BMC biology* 11 (2013), pp. 1–10.

[128] Yanni Xiao et al. "Modeling antiretroviral drug responses for HIV-1 infected patients using differential equation models". In: *Advanced drug delivery reviews* 65.7 (2013), pp. 940–953.

[129] Elissa J Schwartz et al. "HIV dynamics with immune responses: Perspectives from mathematical modeling". In: *Current Clinical Microbiology Reports* 3 (2016), pp. 216–224.

[130] Xinqi Xie, Junling Ma, and P van den Driessche. "Backward bifurcation in within-host HIV models". In: *Mathematical Biosciences* 335 (2021), p. 108569.

[131] FEDERICO Frascoli et al. "A new model describing the development of memory/latency during HIV infection". In: *Canadian Applied Mathematics Quarterly* 21.2 (2013), pp. 183–212.

[132] Alexandra Teslya et al. “A threshold delay model of HIV infection of newborn infants through breastfeeding”. In: *Infectious Disease Modelling* 4 (2019), pp. 188–214.

[133] Redouane Qesmi and Aayah Hammoumi. “A stochastic delay model of HIV pathogenesis with reactivation of latent reservoirs”. In: *Chaos, Solitons & Fractals* 132 (2020), p. 109594.

[134] John Denholm Lambert et al. *Numerical methods for ordinary differential systems*. Vol. 146. Wiley New York, 1991.

[135] Carlos Castillo-Chavez and Baojun Song. “Dynamical models of tuberculosis and their applications”. In: *Mathematical Biosciences & Engineering* 1.2 (2004), pp. 361–404.

[136] Pauline Van den Driessche and James Watmough. “Reproduction numbers and subthreshold endemic equilibria for compartmental models of disease transmission”. In: *Mathematical biosciences* 180.1-2 (2002), pp. 29–48.

[137] Samuel Alizon, Jacobus C. de Roode, and Yannis Michalakis. “Multiple infections and the evolution of virulence”. In: *Ecology Letters* 16.4 (2013). Reviews how within-host viral kinetics and immune clearance shape infection persistence and control., pp. 556–567. DOI: 10.1111/ele.12076. URL: https://doi.org/10.1111/ele.12076.

[138] Jinhu Xu and Yicang Zhou. “Bifurcation analysis of HIV-1 infection model with cell-to-cell transmission and immune response delay”. In: *Mathematical Biosciences & Engineering* 13.2 (2015), pp. 343–367.

[139] Alan S. Perelson and Patrick W. Nelson. “Mathematical analysis of HIV-1 dynamics in vivo”. In: *SIAM Review* 41.1 (1999). Shows that infected-cell lifespan and viral clearance rate are dominant factors in infection persistence., pp. 3–44. DOI: 10.1137/S0036144598335107. URL: https://doi.org/10.1137/S0036144598335107.

[140] Martin A. Nowak and Robert M. May. *Virus Dynamics: Mathematical Principles of Immunology and Virology*. Foundational work linking target-cell dynamics, viral replication, and clearance to infection control. Oxford, UK: Oxford University Press, 2000. ISBN: 978-0198504185.

[141] Sebastian Bonhoeffer et al. "Virus dynamics and drug therapy". In: *Proceedings of the National Academy of Sciences* 94.13 (1997). Demonstrates how infected-cell lifespan and viral clearance rate control persistence and treatment outcomes., pp. 6971–6976. DOI: 10.1073/pnas.94.13.6971. URL: https://doi.org/10.1073/pnas.94.13.6971.

[142] William J Moss and Diane E Griffin. "Measles". In: *The Lancet* 379.9811 (2012), pp. 153–164. ISSN: 0140-6736. DOI: https://doi.org/10.1016/S0140-6736(10)62352-5. URL: https://www.sciencedirect.com/science/article/pii/S0140673610623525.

[143] World Health Organization. *Measles vaccines: WHO position paper*. https://www.who.int/health-topics/measles. 2017.

[144] Public Health Agency of Canada. *Measles and Rubella Weekly Monitoring Report*. https://www.canada.ca/. 2018.

[145] Amra Uzicanin and Corinne M. Zimmerman. "Field effectiveness of live attenuated measles-containing vaccines: a review of published literature". In: *J Infect Dis* 204 (2011). Supplement 1, S133–S148.

[146] Centers for Disease Control and Prevention. *Measles Vaccine Effectiveness*. https://www.cdc.gov/measles/vaccination.html. Accessed: 2025. 2024.

[147] Public Health Agency of Canada. *Measles and Rubella Weekly Monitoring Report*. https://www.canada.ca/en/public-health/services/immunization-vaccine-preventable-diseases/measles.html. Accessed: 2025. 2025.

[148] Public Health Agency of Canada. *National Immunization Coverage Survey (NICS): Results*. https://www.canada.ca/en/public-health/services/publications/vaccines-immunization/. Accessed: 2025. 2021.

[149] Adedayo O Faneye et al. "Measles virus infection among vaccinated and unvaccinated children in Nigeria". In: *Viral immunology* 28.6 (2015), pp. 304–308.

[150] Eva Avramovich. "Measles outbreak in a highly vaccinated population—Israel, July–August 2017". In: *MMWR. Morbidity and Mortality Weekly Report* 67 (2018).

[151] Martha Iwamoto et al. "Measles infection in persons with secondary vaccine failure, New York City, 2018–19". In: *Vaccine* 39.38 (2021), pp. 5346–5350.

[152] Archchun Ariyarajah et al. "Measles seroprevalence among individuals serologically tested in Ontario, Canada". In: *Vaccine* 62 (2025), p. 127446.

[153] Odo Diekmann, Hans Heesterbeek, and Tom Britton. *Mathematical Tools for Understanding Infectious Disease Dynamics*. Princeton University Press, 2013.

[154] Fiona M Guerra et al. "The basic reproduction number (R0) of measles: a systematic review". In: *The Lancet Infectious Diseases* 17.12 (2017), e420–e428.

[155] World Health Organization (WHO). *Data overview for Canada*. http://www.who.int/countries/can/en/. Accessed: 2025-09-18. 2025.

[156] Julien Arino et al. "Final size relations for epidemic models". In: *Mathematical Biosciences & Engineering* 4.2 (2007), pp. 159–175.

[157] Linda JS Allen. *An introduction to stochastic processes with applications to biology*. CRC press, 2010.

[158] Katelyn M Gostic et al. "Potent protection against H5N1 and H7N9 influenza via childhood hemagglutinin imprinting". In: *Science* 354.6313 (2016), pp. 722–726.

[159] Velislava N Petrova and Colin A Russell. "The evolution of seasonal influenza viruses". In: *Nature Reviews Microbiology* 16.1 (2018), pp. 47–60.

[160] J. M. et al. Fonville. “Antibody landscapes after influenza virus infection or vaccination”. In: *Science* 346.6212 (2014), 996–1000.

[161] Robert G Webster et al. “Evolution and ecology of influenza A viruses”. In: *Microbiological reviews* 56.1 (1992), pp. 152–179.

[162] Trevor Bedford et al. “Global circulation patterns of seasonal influenza viruses vary with antigenic drift”. In: *Nature* 523.7559 (2015), pp. 217–220.

[163] Alicia M Fry et al. “Influenza Vaccine Effectiveness Against Drifted Versus Vaccine-Like A/H3N2 Viruses During the 2014-15 Influenza Season—US Flu VE Network”. In: *Open Forum Infectious Diseases*. Vol. 2. suppl_1. Infectious Diseases Society of America. 2015, p. 1350.

[164] Giorgia Vattiato et al. “Modelling the dynamics of infection, waning of immunity and re-infection with the Omicron variant of SARS-CoV-2 in Aotearoa New Zealand”. In: *Epidemics* 41 (2022), p. 100657.

[165] Jeffery K Taubenberger and David M Morens. “1918 Influenza: the mother of all pandemics”. In: *Revista Biomedica* 17.1 (2006), pp. 69–79.

[166] Niall PAS Johnson and Juergen Mueller. “Updating the accounts: global mortality of the 1918-1920" Spanish" influenza pandemic”. In: *Bulletin of the History of Medicine* 76.1 (2002), pp. 105–115.

[167] Vanessa Cozza et al. “Global seasonal influenza mortality estimates: a comparison of 3 different approaches”. In: *American journal of epidemiology* 190.5 (2021), pp. 718–727.

[168] A Danielle Iuliano et al. “Estimates of global seasonal influenza-associated respiratory mortality: a modelling study”. In: *The Lancet* 391.10127 (2018), pp. 1285–1300.

[169] Fabrice Carrat et al. “Time lines of infection and disease in human influenza: a review of volunteer challenge studies”. In: *American journal of epidemiology* 167.7 (2008), pp. 775–785.

[170] Mohsen Moghadami. “A narrative review of influenza: a seasonal and pandemic disease”. In: *Iranian journal of medical sciences* 42.1 (2017), p. 2.

[171] Laetitia Canini and Fabrice Carrat. “Population modeling of influenza A/H1N1 virus kinetics and symptom dynamics”. In: *Journal of virology* 85.6 (2011), pp. 2764–2770.

[172] Chun-Miin Jimmy Chen and Alia C Stanciu. “Simulating influenza epidemics with waning vaccine immunity”. In: *Medicine* 100.36 (2021), e27169.

[173] Manish M Patel et al. “Immune-mediated attenuation of influenza illness after infection: opportunities and challenges”. In: *The Lancet Microbe* 2.12 (2021), e715–e725.

[174] Neil M Ferguson et al. “Strategies for mitigating an influenza pandemic”. In: *Nature* 442.7101 (2006), pp. 448–452.

[175] Vittoria Colizza et al. “Modeling the worldwide spread of pandemic influenza: baseline case and containment interventions”. In: *PLoS medicine* 4.1 (2007), e13.

[176] Rutger G Woolthuis, Jacco Wallinga, and Michiel van Boven. “Variation in loss of immunity shapes influenza epidemics and the impact of vaccination”. In: *BMC infectious diseases* 17.1 (2017), p. 632.

[177] Edward M Hill et al. “Seasonal influenza: Modelling approaches to capture immunity propagation”. In: *PLoS computational biology* 15.10 (2019), e1007096.

[178] Musa Rabiu and Sarafa A Iyaniwura. “Assessing the potential impact of immunity waning on the dynamics of COVID-19 in South Africa: an endemic model of COVID-19”. In: *Nonlinear dynamics* 109.1 (2022), pp. 203–223.

[179] Kenneth L Cooke and P Van Den Driessche. “Analysis of an SEIRS epidemic model with two delays”. In: *Journal of mathematical biology* 35.2 (1996), pp. 240–260.

[180] Bimal Kumar Mishra and Dinesh Kumar Saini. “SEIRS epidemic model with delay for transmission of malicious objects in computer network”. In: *Applied mathematics and computation* 188.2 (2007), pp. 1476–1482.

[181] Wendi Wang. “Global behavior of an SEIRS epidemic model with time delays”. In: *Applied Mathematics Letters* 15.4 (2002), pp. 423–428.

[182] Jane M Heffernan and Matthew James Keeling. “An in-host model of acute infection: measles as a case study”. In: *Theoretical population biology* 73.1 (2008), pp. 134–147.

[183] Jose-Luis Sagripanti and C David Lytle. “Inactivation of influenza virus by solar radiation”. In: *Photochemistry and photobiology* 83.5 (2007), pp. 1278–1282.

[184] Rutu Karia et al. “COVID-19 and its modes of transmission”. In: *SN comprehensive clinical medicine* 2.10 (2020), pp. 1798–1801.

[185] Government of Ontario. *Reopening Ontario*. `https://www.ontario.ca/page/reopening-ontario/`. Accessed: 2020-06-30. 2020.

[186] Elena Aruffo et al. “COVID-19 transmission in a theme-park”. In: *medRxiv* (2021), pp. 2021–04.

[187] Statista. *Attendance at the Walt Disney World Magic Kingdom theme park worldwide from 2008 to 2023*. `https://www.statista.com/statistics/232966/attendance-at-the-walt-disney-world-magic-kingdom-theme-park/`. Accessed: 2025-07-05. 2025.

[188] Marco D’Orazio, Gabriele Bernardini, and Enrico Quagliarini. “How to restart? An agent-based simulation model towards the definition of strategies for COVID-19 “second phase" in public buildings”. In: *arXiv preprint arXiv:2004.12927* (2020).

[189] Laura Fierce, Alison J Robey, and Cathrine Hamilton. “High efficacy of layered controls for reducing exposure to airborne pathogens”. In: *Indoor air* 32.2 (2022), e12989.

[190] Julie Mazziotta. “Teen with Measles Went to Disneyland and Universal Studios, Health Officials Warn”. In: *People* (Aug. 2019). Published online: August 26, 2019. Accessed:

2025-07-05. URL: https://people.com/health/teen-with-measles-went-to-disneyland-and-universal-studios-health-officials-warn/.

[191] U.S. Centers for Disease Control and Prevention. *Standard Precautions for All Patient Care*. https://www.cdc.gov/infection-control/hcp/basics/standard-precautions.html/. Accessed: 2025-07-05. 2024.

[192] Jos H Verbeek et al. "Personal protective equipment for preventing highly infectious diseases due to exposure to contaminated body fluids in healthcare staff". In: *Cochrane database of systematic reviews* 4 (2020).

[193] World Health Organization. *Coronavirus Disease (COVID-19): Masks*. https://www.who.int/news-room/questions-and-answers/item/coronavirus-disease-covid-19-masks/. Accessed: 2025-07-05. 2023.

[194] Peter Caley, David J Philp, and Kevin McCracken. "Quantifying social distancing arising from pandemic influenza". In: *Journal of the Royal Society Interface* 5.23 (2008), pp. 631–639.

[195] Rodrigo DeAntonio et al. "Norovirus in children under 2 years of age: An epidemiological study in Panama during the COVID-19 pandemic". In: *Frontiers in Pediatrics* 12 (2024), p. 1292967.

[196] Paul A Gastanaduy et al. "Public health responses during measles outbreaks in elimination settings: Strategies and challenges". In: *Human vaccines & immunotherapeutics* 14.9 (2018), pp. 2222–2238.

[197] Shelly L Miller et al. "Transmission of SARS-CoV-2 by inhalation of respiratory aerosol in the Skagit Valley Chorale superspreading event". In: *Indoor air* 31.2 (2021), pp. 314–323.

[198] Leonardo Setti et al. *Airborne transmission route of COVID-19: why 2 meters/6 feet of inter-personal distance could not be enough*. 2020.

[199] Farah Yasmin, Syed Hasan Ali, and Irfan Ullah. “Norovirus outbreak amid COVID-19 in the United Kingdom; priorities for achieving control”. In: *Journal of Medical Virology* 94.3 (2022), pp. 1232–1235.

[200] Chaojun Xie et al. “The evidence of indirect transmission of SARS-CoV-2 reported in Guangzhou, China”. In: *BMC public health* 20 (2020), pp. 1–9.

[201] Anass Bouchnita and Aissam Jebrane. “A hybrid multi-scale model of COVID-19 transmission dynamics to assess the potential of non-pharmaceutical interventions”. In: *Chaos, Solitons & Fractals* 138 (2020), p. 109941.

[202] Shih-Fen Cheng et al. “An agent-based simulation approach to experience management in theme parks”. In: *2013 Winter Simulations Conference (WSC)*. IEEE. 2013, pp. 1527–1538.

[203] Kiesha Prem, Alex R Cook, and Mark Jit. “Projecting social contact matrices in 152 countries using contact surveys and demographic data”. In: *PLoS computational biology* 13.9 (2017), e1005697.

[204] Jesse Knight and Sharmistha Mishra. “Estimating effective reproduction number using generation time versus serial interval, with application to COVID-19 in the Greater Toronto Area, Canada”. In: *Infectious Disease Modelling* 5 (2020), pp. 889–896.

[205] A Meiksin. “Dynamics of COVID-19 transmission including indirect transmission mechanisms: a mathematical analysis”. In: *Epidemiology & Infection* 148 (2020), e257.

[206] Ying Liu and Joacim Rocklöv. “The effective reproductive number of the Omicron variant of SARS-CoV-2 is several times relative to Delta”. In: *Journal of travel medicine* 29.3 (2022), taac037.

[207] Sawitree Boonpatcharanon, Jane M Heffernan, and Hanna Jankowski. “Estimating the basic reproduction number at the beginning of an outbreak”. In: *Plos one* 17.6 (2022), e0269306.

[208] Odo Diekmann, Johan Andre Peter Heesterbeek, and Johan Anton Jacob Metz. "On the definition and the computation of the basic reproduction ratio R0 in models for infectious diseases in heterogeneous populations". In: *Journal of mathematical biology* 28 (1990), pp. 365–382.

[209] MG Roberts. "The pluses and minuses of R0". In: *Journal of the Royal Society Interface* 4.16 (2007), p. 949.

[210] Md Afsar Ali et al. "Global sensitivity analysis of a single-cell HBV model for viral dynamics in the liver". In: *Infectious Disease Modelling* 6 (2021), pp. 1220–1235.

[211] Pierrot Derjany et al. "Multiscale model for the optimal design of pedestrian queues to mitigate infectious disease spread". In: *PloS one* 15.7 (2020), e0235891.

[212] Lee Worden et al. "Measles transmission during a large outbreak in California". In: *Epidemics* 30 (2020), p. 100375.

[213] Sudarat Chadsuthi and Surapa Wichapeng. "The modelling of hand, foot, and mouth disease in contaminated environments in Bangkok, Thailand". In: *Computational and mathematical methods in medicine* 2018.1 (2018), p. 5168931.

[214] Jeremy Howard et al. "An evidence review of face masks against COVID-19". In: *Proceedings of the National Academy of Sciences* 118.4 (2021), e2014564118.

[215] Derek K Chu et al. "Physical distancing, face masks, and eye protection to prevent person-to-person transmission of SARS-CoV-2 and COVID-19: a systematic review and meta-analysis". In: *The lancet* 395.10242 (2020), pp. 1973–1987.

[216] Centers for Disease Control and Prevention. *Social Distancing: Keep a Safe Distance to Slow the Spread*. Tech. rep. Accessed: 2025-03-16. U.S. Department of Health and Human Services, 2020.

[217] Steffen E Eikenberry et al. “To mask or not to mask: Modeling the potential for face mask use by the general public to curtail the COVID-19 pandemic”. In: *Infectious disease modelling* 5 (2020), pp. 293–308.

[218] Stefan Emrich, Sergej Suslov, and Florian Judex. “Fully agent based modellings of epidemic spread using AnyLogic”. In: *Proc. eurosim*. 2007, pp. 9–13.

[219] Alexei Filippov and Andrei Borshchev. “OMER-2 workshop Daimler-Chrysler modeling contest–Modeling S-class car seat control with AnyLogic”. In: *OMER-Object-oriented Modeling of Embedded Real-Time Systems, GI-Workshops OMER-1 & OMER-2*. Gesellschaft für Informatik e. V. 2001, pp. 46–50.

[220] Andrei Borshchev. “Multi-method modelling: AnyLogic”. In: Apr. 2014, pp. 248–279. ISBN: 9781118349021. DOI: 10.1002/9781118762745.ch12.

[221] Averill M. Law. *Simulation Modeling and Analysis*. 5th ed. McGraw-Hill, 2015.

[222] Andrei Borshchev and Yuri Karpov. “Multimethod modeling with AnyLogic”. In: *Proceedings of the Winter Simulation Conference*. IEEE. 2014, pp. 248–259.

[223] Pallavi Zambare and Ying Liu. “Modeling and Simulation of Pedestrian Behavior in Traffic Environment: A Systematic Review of Approaches and Software”. In: *IEEE Transactions on Intelligent Transportation Systems* 21.9 (2020), pp. 3929–3944.

[224] Jing Li and Felix T.S. Chan. “An agent-based model of supply chains with dynamic structures”. In: *Applied Mathematical Modelling* 37.7 (2013), pp. 5403–5413. ISSN: 0307-904X. DOI: https://doi.org/10.1016/j.apm.2012.10.054. URL: https://www.sciencedirect.com/science/article/pii/S0307904X12006592.

[225] Michael Pidd. *Computer simulation in management science*. John Wiley & Sons, Inc., 1998.

[226] Gang Li, Haiyan Song, and Stephen F Witt. “Recent developments in econometric modeling and forecasting”. In: *Journal of travel Research* 44.1 (2005), pp. 82–99.

[227] Themed Entertainment Association and AECOM. *Theme Index and Museum Index*. Annual report on global theme park and museum attendance. Themed Entertainment Association, 2023.

[228] Dirk Helbing and Peter Molnar. "Social force model for pedestrian dynamics". In: *Physical review E* 51.5 (1995), p. 4282.

[229] Dirk Helbing et al. "Self-organized pedestrian crowd dynamics: Experiments, simulations, and design solutions". In: *Transportation science* 39.1 (2005), pp. 1–24.

[230] Canada's Wonderland. *Ride Information and Attraction Details*. `https://www.canadaswonderland.com/rides-experiences`. Accessed January 31, 2026. 2026.

[231] Kenji Mizumoto et al. "Estimating the asymptomatic proportion of coronavirus disease 2019 (COVID-19) cases on board the Diamond Princess cruise ship, Yokohama, Japan, 2020". In: *Eurosurveillance* 25.10 (2020), p. 2000180.

[232] Oyungerel Byambasuren et al. "Estimating the extent of asymptomatic COVID-19 and its potential for community transmission: systematic review and meta-analysis". In: *Official Journal of the Association of Medical Microbiology and Infectious Disease Canada* 5.4 (2020), pp. 223–234.

[233] Enagnon Kazali Alidjinou et al. "Resistance of enteric viruses on fomites". In: *Intervirology* 61.5 (2019), pp. 205–213.

[234] Ottar N Bjørnstad, Bärbel F Finkenstädt, and Bryan T Grenfell. "Dynamics of measles epidemics: estimating scaling of transmission rates using a time series SIR model". In: *Ecological monographs* 72.2 (2002), pp. 169–184.

[235] Ben Lopman et al. "Epidemiologic implications of asymptomatic reinfection: A mathematical modeling study of norovirus". In: *American journal of epidemiology* 179.4 (2014), pp. 507–512.

[236] Chong W Ong. “Norovirus: A challenging pathogen”. In: *Healthcare infection* 18.4 (2013), pp. 133–142.

[237] World Health Organization. *Coronavirus disease (COVID-19): Similarities and differences with influenza*. `https://www.who.int/news-room/q-a-detail/coronavirus-disease-covid-19-similarities-and-differences-with-influenza`. 2020.

[238] OJ Peter et al. “Mathematical model for the control of measles”. In: *Journal of Applied Sciences and Environmental Management* 22.4 (2018), pp. 571–576.

[239] Mathew P Dafilis et al. “Dynamical crises, multistability and the influence of the duration of immunity in a seasonally-forced model of disease transmission”. In: *Theoretical Biology and Medical Modelling* 11 (2014), pp. 1–10.

Appendix

A. Model Description

A comprehensive flowchart illustrating the model is depicted in Figure 6.1. Model parameters are listed in Tables 6.1 and 6.2.

The theme park population is divided into visitor (V) and worker (W) sub-populations. These are further subdivided into disease classes: susceptible (S), exposed (E), pre-symptomic infectious (A), asymptomatic infectious (I_a), symptomatic infectious (I_S) and immune (R).

Upon arrival at the park gate, visitors and workers undergo symptom monitoring. Those found symptom-free are permitted entry into the park. Consequently, only individuals categorized as susceptible, pre-symptomatic, asymptomatic infectious, or immune are granted access.

Upon entering the park, visitors are assigned to PPE compliant (VP) and non-compliant (VNP) subgroups with probabilities v_p and $1 - v_p$, respectively. It is assumed that workers adhere to PPE guidelines mandated by their employers.

The theme park is divided into n patches. Each patch is further divided into ride (r) and queue (q) environments.

Upon entering the park, each worker or visitor is allocated to a specific home patch i. The allocation of the home patch determines the proportion of time that an individual spends in each of the n patches while in the park. This is denoted by y_{ij}^k, where $y = w, v, v^{Is}$, $i, j = 1, \cdots, n, k = W, VP, VNP$, and $\sum_j y_{ij}^k = 1$ for any given combination of $i = 1, ..., n$ and $k = W, VP, VNP$. The distribution of home patch assignments can be provided by

the theme park. Currently, we assume a distribution, denoted as $\lambda^k_{S,i}, \lambda^k_{E,i}, \lambda^k_{A,i}, \lambda^k_{Ia,i}, \lambda^k_{R,I}$, $i = 1, \cdots, n$, $k = W, V$, where V represents the total visitor population ($VP + VNP$).

Susceptible individuals, S, are susceptible to infection by pre-symptomatic, asymptomatic, and symptomatic infectious individuals - both workers and visitors - from any patch ($A^k_i, I^k_{ai}, I^k_{si}$, where $i = 1, \cdots, n$ and $k = W, VP, VNP$) within the park. Alternatively, transmission can occur indirectly through contact with contaminated environments such as queues or rides (H^q, H^r). Upon infection, an individual transitions to the exposed class E and remains there for $1/\alpha$ days, on average. Subsequently, they move to the pre-symptomatic infectious class (A^k_i) and remain there for $1/\delta$ days, on average. As the disease progresses, an infected individual may either develop symptomatic infection (I^k_{si}) with probability q or remain asymptomatic (I^k_{ai}) with probability of $1 - q$. Upon the onset of symptoms, it is assumed that symptomatic visitors and workers will leave the park within 30 minutes ($1/\gamma_2$) (on average).

The model represents pathogen transmission among humans through contact rates between workers c^W, visitors c^V, and between workers and visitors c^{WV}, along with transmission probabilities among PPE-compliant individuals π^P, PPE non-compliant individuals π^{NP}, and between individuals from both groups π^{PNP}. It is assumed that π^P and π^{PNP} are correlated with π^{NP} and the efficacy of PPE in preventing human-to-human transmission s_h. Transmission from the environment to humans is simulated using transmission rates in queues $\beta^{HP}_q, \beta^{HNP}_q$ and on rides $\beta^{HP}_r, \beta^{HNP}_r$, considering individuals as PPE-compliant (HP) or non-compliant (HNP). Furthermore, infectious individuals are assumed to release pathogens into queue and ride environments at a rate κ, with PPE having effectiveness f in reducing this shedding.

B. Model Equations

For a given population $k = W, VP, VNP$ and a given patch $i = 1, ..., n$, we have:

$$S'^k_i = \lambda^k_{S,i} - B^k_i S^k_i$$

$$E_i^{'k} = \lambda_{E,i}^k + \mathrm{B}_i^k S_i^k - \alpha E_i^k$$

$$\mathrm{A}_i^{'k} = \lambda_{\mathrm{A},i}^k + \alpha E_i^k - \delta \mathrm{A}_i^k$$

$$I_{a,i}^{'k} = \lambda_{Ia,i}^k + (1-q)\delta \mathrm{A}_i^k - \gamma I_{a,i}^k$$

$$I_{s,i}^{'k} = q\delta \mathrm{A}_i^k - \gamma_2 I_{s,i}^k$$

$$R_i^{'k} = \lambda_{R,i}^k + \gamma I_{a,i}^k$$

$$H_i^{'q} = B_i^q H_i^q - \epsilon H_i^q$$

$$H_i^{'r} = B_i^r H_i^r - \epsilon H_i^r$$

where,

$$\begin{aligned}
B_i^W = \omega_{ii}^q &\left(\frac{\pi^P c^W W_{(inf,i)}^q + \pi^P c^{WV} VP_{(inf,i)}^q + \pi^{NP} c^{WV} VNP_{(inf,i)}^q}{N_i} \right) \\
+\omega_{ij}^q &\left(\frac{\pi^P c^W W_{(inf,j)}^q + \pi^P c^{WV} VP_{(inf,j)}^q + \pi^{NP} c^{WV} VNP_{(inf,j)}^q}{N_j} \right) \\
+\omega_{ii}^r &\left(\frac{\pi^P c^W W_{(inf,i)}^r + \pi^P c^{WV} VP_{(inf,i)}^r + \pi^{NP} c^{WV} VNP_{(inf,i)}^r}{N_i} \right) \\
+\omega_{ij}^r &\left(\frac{\pi^P c^W W_{(inf,j)}^r + \pi^P c^{WV} VP_{(inf,j)}^r + \pi^{NP} c^{WV} VNP_{(inf,j)}^r}{N_j} \right) \\
&+\omega_{ii}^q \left(\frac{\beta_r^{HP} H_i^r}{N_i} + \frac{\beta_q^{HP} H_i^q}{N_i} \right) + \omega_{ij}^q \left(\frac{\beta_r^{HP} H_j^r}{N_j} + \frac{\beta_q^{HP} H_j^q}{N_j} \right)
\end{aligned}$$

$$
\begin{aligned}
B_i^{VP} = v_{ii}^q & \left(\frac{\pi^P c^{WV} W_{(inf,i)}^q + \pi^P c^V V P_{(inf,i)}^q + \pi^{NP} c^V V N P_{(inf,i)}^q}{N_i} \right) \\
+ v_{ij}^q & \left(\frac{\pi^P c^{WV} W_{(inf,j)}^q + \pi^P c^V V P_{(inf,j)}^q + \pi^{NP} c^V V N P_{(inf,j)}^q}{N_j} \right) \\
+ v_{ii}^r & \left(\frac{\pi^P c^{WV} W_{(inf,i)}^r + \pi^P c^V V P_{(inf,i)}^r + \pi^{NP} c^V V N P_{(inf,i)}^r}{N_i} \right) \\
+ v_{ij}^r & \left(\frac{\pi^P c^{WV} W_{(inf,j)}^r + \pi^P c^V V P_{(inf,j)}^r + \pi^{NP} c^V V N P_{(inf,j)}^r}{N_j} \right) \\
+ v_{ii}^q & \left(\frac{\beta_r^{HP} H_i^r}{N_i} + \frac{\beta_q^{HP} H_i^q}{N_i} \right) + v_{ij}^q \left(\frac{\beta_r^{HP} H_j^r}{N_j} + \frac{\beta_q^{HP} H_j^q}{N_j} \right)
\end{aligned}
$$

$$
\begin{aligned}
B_i^{VNP} = v_{ii}^q & \left(\frac{\pi^P c^{WV} W_{(inf,i)}^q + \pi^{NP} c^V V P_{(inf,i)}^q + \pi^{PNP} c^V V N P_{(inf,i)}^q}{N_i} \right) \\
+ v_{ij}^q & \left(\frac{\pi^P c^{WV} W_{(inf,j)}^q + \pi^{NP} c^V V P_{(inf,j)}^q + \pi^{PNP} c^V V N P_{(inf,j)}^q}{N_j} \right) \\
+ v_{ii}^r & \left(\frac{\pi^{NP} c^{WV} W_{(inf,i)}^r + \pi^{NP} c^V V P_{(inf,i)}^r + \pi^{PNP} c^V V N P_{(inf,i)}^r}{N_i} \right) \\
+ v_{ij}^r & \left(\frac{\pi^{NP} c^{WV} W_{(inf,j)}^r + \pi^{NP} c^V V P_{(inf,j)}^r + \pi^{PNP} c^V V N P_{(inf,j)}^r}{N_j} \right) \\
+ v_{ii}^q & \left(\frac{\beta_r^{HNP} H_i^r}{N_i} + \frac{\beta_q^{HNP} H_i^q}{N_i} \right) + v_{ij}^q \left(\frac{\beta_r^{HNP} H_j^r}{N_j} + \frac{\beta_q^{HNP} H_j^q}{N_j} \right)
\end{aligned}
$$

$$
\begin{aligned}
B_i^q &= \frac{\kappa \left((1-f)(W_{(inf,i)}^q + V P_{(inf,i)}^q) + V N P_{(inf,i)}^q \right)}{N_i} \\
B_i^r &= \frac{\kappa \left((1-f)(W_{(inf,i)}^r + V P_{(inf,i)}^r) + V N P_{(inf,i)}^r \right)}{N_i}
\end{aligned}
$$

and

$$W^q_{(inf,i)} = \omega^q_{ii}\left(E^W_i + \mathrm{A}^W_i + I^W_{a,i}\right) + \omega^q_{ji}\left(E^W_j + \mathrm{A}^W_j + I^W_{a,j}\right) + \omega^{qI_s}_{ii} I^W_{s,i} + \omega^{qI_s}_{ij} I^W_{s,j}$$

$$W^q_{(inf,j)} = \omega^q_{ij}\left(E^W_i + \mathrm{A}^W_i + I^W_{a,i}\right) + \omega^q_{jj}\left(E^W_j + \mathrm{A}^W_j + I^W_{a,j}\right) + \omega^{qI_s}_{ij} I^W_{s,i} + \omega^{qI_s}_{jj} I^W_{s,j}$$

$$VP^q_{(inf,i)} = v^q_{ii}\left(E^{VP}_i + \mathrm{A}^{VP}_i + I^{VP}_{a,i}\right) + v^q_{ji}\left(E^{VP}_j + \mathrm{A}^{VP}_j + I^{VP}_{a,j}\right) + v^{qI_s}_{ii} I^{VP}_{s,i} + v^{qI_s}_{ij} I^{VP}_{s,j}$$

$$VP^q_{(inf,j)} = v^q_{ij}\left(E^{VP}_i + \mathrm{A}^{VP}_i + I^{VP}_{a,i}\right) + v^q_{jj}\left(E^{VP}_j + \mathrm{A}^{VP}_j + I^{VP}_{a,j}\right) + v^{qI_s}_{ij} I^{VP}_{s,i} + v^{qI_s}_{jj} I^{VP}_{s,j}$$

$$VNP^q_{(inf,i)} = v^q_{ii}\left(E^{VNP}_i + \mathrm{A}^{VNP}_i + I^{VNP}_{a,i}\right) + v^q_{ji}\left(E^{VNP}_j + \mathrm{A}^{VNP}_j + I^{VNP}_{a,j}\right) + v^{qI_s}_{ii} I^{VNP}_{s,i} + v^{qI_s}_{ji} I^{VNP}_{s,j}$$

$$VNP^q_{(inf,j)} = v^q_{ij}\left(E^{VNP}_i + \mathrm{A}^{VNP}_i + I^{VNP}_{a,i}\right) + v^q_{jj}\left(E^{VNP}_j + \mathrm{A}^{VNP}_j + I^{VNP}_{a,j}\right) + v^{qI_s}_{ij} I^{VNP}_{s,i} + v^{qI_s}_{jj} I^{VNP}_{s,j}$$

$$W^r_{(inf,i)} = \omega^r_{ii}\left(E^W_i + \mathrm{A}^W_i + I^W_{a,i}\right) + \omega^r_{ji}\left(E^W_j + \mathrm{A}^W_j + I^W_{a,j}\right) + \omega^{rI_s}_{ii} I^W_{s,i} + \omega^{rI_s}_{ij} I^W_{s,j}$$

$$W^r_{(inf,j)} = \omega^r_{ij}\left(E^W_i + \mathrm{A}^W_i + I^W_{a,i}\right) + \omega^r_{jj}\left(E^W_j + \mathrm{A}^W_j + I^W_{a,j}\right) + \omega^{rI_s}_{ij} I^W_{s,i} + \omega^{rI_s}_{jj} I^W_{s,j}$$

$$VP^r_{(inf,i)} = v^r_{ii}\left(E^{VP}_i + \mathrm{A}^{VP}_i + I^{VP}_{a,i}\right) + v^r_{ji}\left(E^{VP}_j + \mathrm{A}^{VP}_j + I^{VP}_{a,j}\right) + v^{rI_s}_{ii} I^{VP}_{s,i} + v^{rI_s}_{ij} I^{VP}_{s,j}$$

$$VP^r_{(inf,j)} = v^r_{ij}\left(E^{VP}_i + \mathrm{A}^{VP}_i + I^{VP}_{a,i}\right) + v^r_{jj}\left(E^{VP}_j + \mathrm{A}^{VP}_j + I^{VP}_{a,j}\right) + v^{rI_s}_{ji} I^{VP}_{s,i} + v^{rI_s}_{jj} I^{VP}_{s,j}$$

$$VNP^r_{(inf,i)} = v^r_{ii}\left(E^{VNP}_i + \mathrm{A}^{VNP}_i + I^{VNP}_{a,i}\right) + v^r_{ji}\left(E^{VNP}_j + \mathrm{A}^{VNP}_j + I^{VNP}_{a,j}\right) + v^{rI_s}_{ii} I^{VNP}_{s,i} + v^{rI_s}_{ij} I^{VNP}_{s,j}$$

$$VNP^r_{(inf,j)} = v^r_{ij}\left(E^{VNP}_i + \mathrm{A}^{VNP}_i + I^{VNP}_{a,i}\right) + v^r_{jj}\left(E^{VNP}_j + \mathrm{A}^{VNP}_j + I^{VNP}_{a,j}\right) + v^{rI_s}_{ij} I^{VNP}_{s,i} + v^{rI_s}_{jj} I^{VNP}_{s,j}$$

List of parameters			
Parameter	**Value**	**Ref**	**Description**
γ_2	2 $hours^{-1}$	Assumed	Exit rate for symptomatic cases
s_h	$0-1$	Assumed	PPE effectiveness (human-human). We assume $s_h = 0$, 0.1, 0.9.
π^{NP}	see Table 6.2	see Table 6.2	probability of generating an infected between unprotected individuals.
π^{P}	$(1-s_h)\pi^{NP}$	Assumed	probability of generating an infected between protected individuals
π^{PNP}	$(1-s_h/2)\pi^{NP}$	Assumed	probability of generating an infected between protected and not protected individuals.
c^W, c^V, c^{WV}	$2-10$	[203]	contacts between workers, visitors, and workers with visitors, respectively. We assume $c^V = 5$, 10, $c^W = 2$, and $c^{WV} = 4$.
β_r^{HNP}, β_q^{HNP}	1/20000	Assumed	Infection transmission rate from rides (r) and queues (q) to humans without protection.
β_r^{HP}, β_q^{HP}	$(1-f)\beta_{(r,q)}^{HNP}$	Assumed	Infection transmission rate from rides (r) and queues (q) to humans with protection.
f	$0-1$	Assumed	PPE effectiveness (environment-human). We assume $f = 0$, 0.1, 0.9.
vp_{size}	$0-1$	Assumed	Proportion of visitors wearing PPE correctly.
i_{ap}	$0-1$	Assumed	Proportion of infectious visitors entering the park.
$y_{i,j}^x$	$0-1$	[202]	Proportion of time spent by S, E, A, I_a, R workers ($y = w$) and visitors ($y = v$) from patch i in patch $j; i, j = 1, ...n$, in queues ($x = q$) or on the rides ($x = r$).
$y_{i,j}^{xI_s}$	0	Assumed	Proportion of time spent by I_s workers ($y = w$) and visitors ($y = v$) from patch i in patch $j; i, j = 1, ...n$, in queues ($x = q$) or on the rides ($x = r$).
$\lambda_{S,i}^k$	0.95 (of total population)	Assumed	Susceptible Individual
$\lambda_{E,i}^k$	0	Assumed	Exposed Individual
$\lambda_{A,i}^k$	0.05 (of total population)	Assumed	presymptomic infectious
$\lambda_{Ia,i}^k$	$0.001-0.5$ (of total A population)	Assumed	asymptomatic infectious
$\lambda_{R,i}^k$	0	Assumed	Recovered Individual within the park

Table 6.1: Model parameter values associated with visitors, workers, and the environment

Parameter	**Definition**	**COVID-19**	**Influenza**	**Measles**	**Norovirus**
$\mathcal{R}_0$	Basic Reproduction Number	$2-6$ [204, 205]	$1-2$ [207]	$12-18$ [154, 182]	$1.2-7.2$ [40]
$\epsilon(t)$	pathogen clearance rate (hrs^{-1})	$\frac{26}{(57)(24)}$ [207]	$\frac{1}{72}$ [183]	$\frac{1}{(3)(24)}$ [182]	$\frac{1}{(7)(24)}$ [233]
α	latent rate (hrs^{-1})	$\frac{1}{(3)(24)}$ [207]	$\frac{1}{(3)(24)}$ [207]	$\frac{1}{(6)(24)}$ [234]	$\frac{1}{24}$ [235]
δ	Average period to enter the second stage of infection (hrs^{-1})	$\frac{2}{(7)(24)}$ [207]	$\frac{1}{(2)(24)}$ [207]	$\frac{1}{(7)(24)}$ [234]	$\frac{1}{24}$ [236]
q	Probability of showing symptoms in the second stage of infection	0.2 [237]	0.2 [Assumed]	0.045 [238]	0.036 [235]
γ	Recovery rate (hrs^{-1})	$\frac{5}{(11)(24)}$ [207]	$\frac{1}{(5)(24)}$ [207]	$\frac{1}{(21)(24)}$ [239]	$\frac{1}{24}$ [236]
π^{NP}	probability of generating an infected between unprotected individuals.	$(2\times10^{-5}-8\times10^{-5})$ [Fig:5.2]	2×10^{-5} [Fig: 5.2]	0.7×10^{-4} [Fig:5.2]	3×10^{-4} [Fig:5.2]
κ	Shedding rate (hrs^{-1})	$3-19$ [Fig:5.2]	3 [Fig:5.2]	35 [Fig:5.2]	6 [Fig:5.2]

Table 6.2: Disease specific parameters for COVID-19, influenza, measles and norovirus.

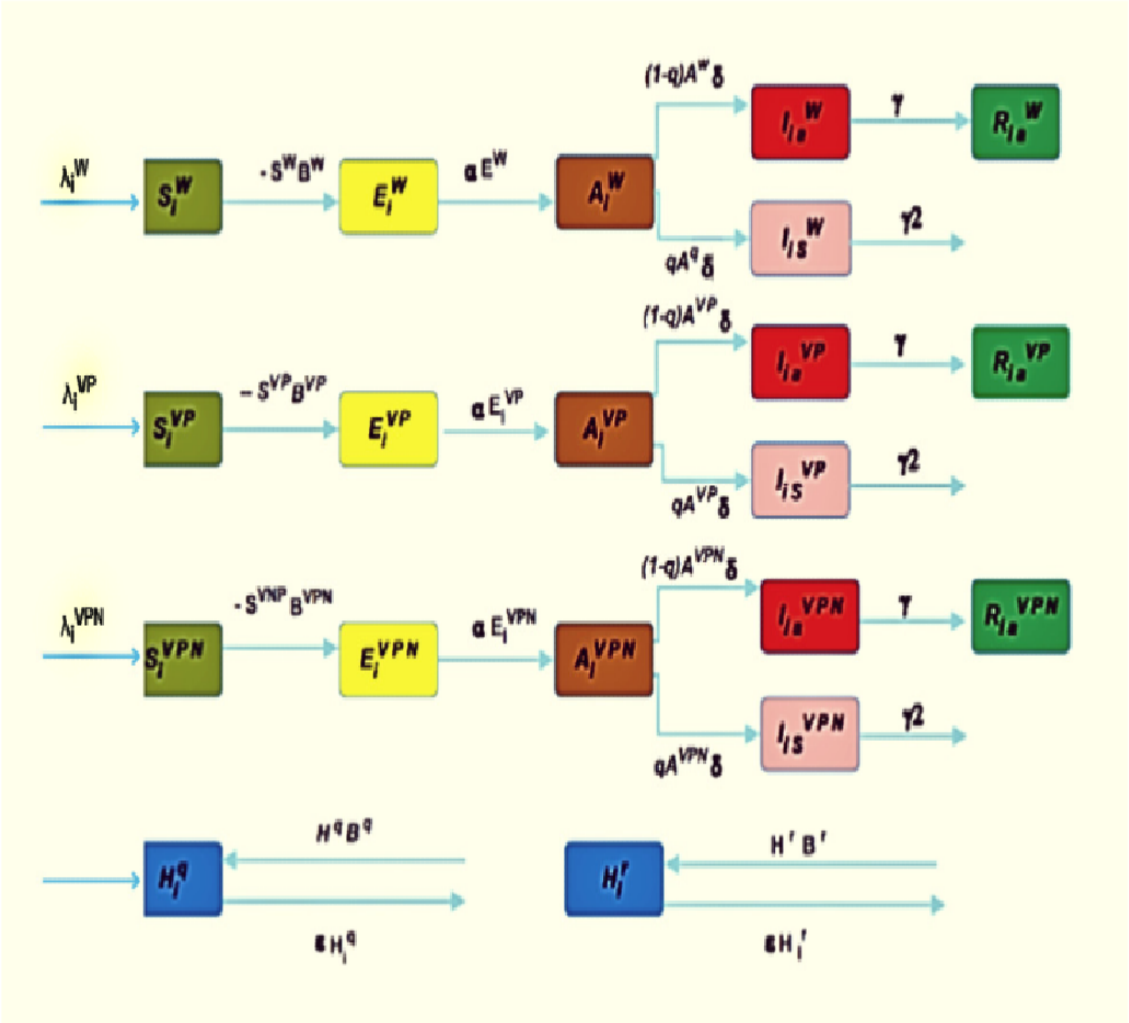

Figure 6.1: Flow diagram of Systems $S1$, in patch i.

Figure 6.2: Scatter plots of (a) basic reproduction number (left) and (b) control reproduction number (right) for COVID-19, influenza, measles and norovirus.